Accurate Colour Reproduction of Human Face using 3D Printing Technology

Ruili He

Submitted in accordance with the requirements for the degree of
Doctor of Philosophy

The University of Leeds
School of Design

April, 2023

The candidate confirms that the work submitted is his/her own, except where work which has formed part of jointly-authored publications has been included. The contribution of the candidate and the other authors to this work has been explicitly indicated below. The candidate confirms that appropriate credit has been given where reference has been made to the work of others.

The following publications were produced in the course of this research:

1. He, R., Xiao, K., Pointer, M. and Westland, S. 2020, September. Assessing skin tone heterogeneity under various light sources. In London Imaging Meeting (Vol. 2020, No. 1, pp. 5-9). Society for Imaging Science and Technology. Referred to Section 4.5.
2. He, R., Xiao, K., Pointer, M., Bressler, Y., Liu, Z. and Lu, Y. 2021. A novel camera colour characterisation model for the colour measurement of human skin. Electronic Imaging, 2021(16), pp.222-1. Referred to Sections 4.1-4.4.
3. Liu, Z., Xiao, K., Pointer, M.R., Liu, Q., Li, C., He, R. and Xie, X., 2021. Spectral reconstruction using an iteratively reweighted regulated model from two illumination camera responses. Sensors, 21(23), p.7911. Referred to Sections 4.1-4.2.
4. He, R., Xiao, K., Pointer, M., Bressler, Y., Liu, Z. and Lu, Y. 2022. Development of an image-based measurement system for human facial skin colour. Colour Research & Application, 47(2), pp.288-300. Referred to Sections 4.1-4.4.
5. He, R., Xiao, K., Pointer, M., Melgosa, M. and Bressler, Y. 2022. An investigation on visual colour difference of 3d printed objects. AIC 2022 Sensing Colour. Referred to Sections 6.1.1 and 6.2-6.3.
6. He, R., Xiao, K., Pointer, M., Melgosa, M. and Bressler, Y. 2022. Optimizing parametric factors in CIELAB and CIEDE2000 colour-difference formulas for 3d-printed spherical objects. Materials, 15(12), p.4055. Referred to Chapter 6.
7. He, R., Xiao, K., Pointer, M., Bressler, Y. and Liu Q. Investigation on color characterization methods for 3D printer. Accepted by London Imaging Meeting 2023. Referred to Section 5.1.

Acknowledgements

First of all, I would like to express my deepest gratitude to my first supervisor, Dr. Kaida Xiao, for his constant support and expert guidance on my PhD study. He helped me achieve a deeper understanding of my research project and always encouraged me to present my research work at conferences and expand my professional network. I also would like to thank my second supervisor, Prof. Stephen Westland, for his valuable insights and constructive advice on shaping my research and future career.

Great thanks to Prof. Michael Pointer for offering a series of lectures on colour science and his insightful comments on my research work. I am grateful to Yoav Bressler, the colour scientist from Stratasys Ltd., for his valuable advice and technical support in 3D printing, and for inviting me to conduct experiments at Stratasys. I also want to thank Prof. Manuel Melgosa from University of Granada for his advice and feedback on colour-difference evaluation, and Prof. Zhen Liu from Qufu Normal University for his continuous support and encouragement, particularly during the COVID-19 period. Many thanks to my friends and colleagues in our school and the Colour Technology Group who have always supported me and made my time at Leeds an unforgettable experience that I will treasure.

I acknowledge the financial support and excellent training events of the ApPEARS (Appearance Printing - European Advanced Research School), which is funded by the European Union’s Horizon 2020 research and innovation programme under the Marie Skłodowska-Curie grant agreement No. 814158. I also would like to bring my special thanks to my examiners: Prof. Phil Green and Dr. Muriel Rigout, for their excellent questions and comments.

Last but not least, I want to thank my parents for their unconditional support and invisible love, my siblings and relatives for taking good care of my family so that I can devote myself into my PhD study in a foreign country. It would have been impossible to complete this work without the help of any of the above, I cannot thank you all enough. Wish everyone is becoming better and better.

Abstract

The colour of the face is one of the most significant factors in appearance and perception of an individual. With the rapid development of colour 3D printing technology and 3D imaging acquisition techniques, it is possible to achieve skin colour reproduction with the application of colour management. However, due to the complicated skin structure with uneven and non-uniform surface, it is challenging to obtain accurate skin colour appearance and reproduce it faithfully using 3D colour printers.

The aim of this study was to improve the colour reproduction accuracy of the human face using 3D printing technology. A workflow of 3D colour image reproduction was developed, including 3D colour image acquisition, 3D model manipulation, colour management, colour 3D printing, postprocessing and colour reproduction evaluation. Most importantly, the colour characterisation methods for the 3D imaging system and the colour 3D printer were comprehensively investigated for achieving higher accuracy. Specifically, a designated digital imaging system was developed to capture human faces to explore the effects of different factors, such as image format, training dataset and mapping method, on the accuracy of skin tone estimation. The findings supported the successful colour characterisation for the 3dMDface system to capture a 3D model of the human face with realistic skin colours.

For the colour 3D printer, the methods of conventional polynomial regression and deep neural networks were investigated for printer colour characterisation which transforms from the printer controlled colour space to an output device-independent colour space, and five types of variables were compared as the output for producing higher precision in printing skin colours. Moreover, a specific skin colour chart was printed using the 3D printer to determine the colour profile for achieving faithful skin colour reproduction.

In addition, psychophysical experiments with the grey-scale method were conducted to collect visual colour-differences data of 3D printed samples, and the results showed that the performance of CIELAB and CIEDE2000 colour-difference formulae needs to be improved for 3D objects. Consequently, the parametric factors in the colour-difference formulae were optimised ($k_L = 1.4, k_C = 1.9$ for CIELAB, and $k_L = 1.5$ for CIEDE2000), and the accuracy of 3D colour reproduction was evaluated using the optimised formulae.

Based on the developed colour characterisation methods, a 3D model of a human face was printed using the proposed 3D colour image reproduction workflow, and the accuracy achieved was 5.73 CIELAB units (3.88 CIEDE2000 units). The values were 3.75 and 3.42 units for the optimised colour-difference formulae. Overall, the methods and results presented in this thesis provide a new and improved understanding of colour characterisation and colour evaluation in 3D colour reproduction of human faces.

Table of Contents

List of Tables

List of Figures

Chapter 1
Introduction

1.1 Background

The colour of skin is one of the colours that we see most often in our daily lives, and there are many applications of skin colour appearance for various proposes, such as computer graphics, computer vision, medicine and cosmetology (Igarashi et al. 2005). Particularly, the colour appearance of the human face is the most significant factor indicating an individual’s health, age, attractiveness, emotional state, ethnic and cultural identity, etc. Achieving accurate skin colour reproduction of the human face is important for applications such as photography, digital art, graphic printing, and the fabrication of facial prostheses using 3D printing technology.

With the development of diverse 3D image capturing techniques, the colour and geometric information of a target object can be captured and transformed into 3D digital models. Moreover, colour 3D printing technology makes it possible to produce full colour solid objects and enables colour controlling during the process of colour reproduction. By combining 3D image acquisition and 3D colour printing technology, it is desirable to fabricate soft tissue facial prostheses for patients suffering facial deficiencies, injuries or disfigurations, especially with an increase in the elderly population and the improving cancer survival rates that may involve facial tissues (Zardawi et al. 2015). Compared to the conventional method which is high skilled and both time and cost consuming, this advanced method is preferred because of its advantages in non-contact, flexible design, low cost, and customisation.

Although the 3D imaging technique and colour 3D printing technology have been successfully applied to reproduce a face model, the colour accuracy still needs to be improved, especially considering that the human colour vision system appears to be sensitive to subtle changes in skin colour, reported by Changizi et al. (2006) and Jimenez et al. (2010). Therefore, it is crucial to achieve realistic and consistent skin colour reproduction using 3D printing technology.

The limitations on achieving accurate colour reproduction of the human face usually come from the colour measurement technique used to quantify the colour of actual human skin, involving the colour characterisation for the cameras used to capture the images of the human face. It is challenging due to the wide range of skin tones and colour heterogeneity on an individual's face. Moreover, appropriate colour management approach is necessary in the 3D printing process to ensure that the 3D printer reproduces the desired skin tones accurately. As colour printing technologies continue to advance, new 3D colour printers with superior capabilities have emerged, making it achievable for reproducing skin colours accurately.

Additionally, the evaluation of the accuracy of colour reproduction is of vital importance in the 3D printing process. The colour quality of the 3D printed objects was typically evaluated using colour-difference formulae such as CIELAB and CIEDE2000, however, these formulae were developed based on 2D colour samples, it is unknown how these formulae perform on predicting colour differences of 3D objects. In light of the circumstances, CIE Technical Committee 8-17 has been established to encourage researchers to collect visual colour-difference data of 3D objects and develop methods for evaluating colour differences between 3D objects.

1.2 Aim and Objectives

The aim of this research is to improve the accuracy of the colour reproduction of human face in the 3D printing process, including the tasks on skin colour measurement, 3D colour image acquisition, colour management from 3D imaging system to 3D printer, colour 3D printing and colour reproduction evaluation. During the conduction of this research, it is expected to achieve the following objectives:

- To collect a skin colour database including spectral reflectance data and 2D & 3D colour images of human faces,
- To establish a 3D colour image reproduction workflow of human faces for achieving higher accuracy,
- To investigate the colour characterisation method for accurately capturing colour information in the 3D imaging system,
- To develop a colour profile of the 3D printer for faithfully reproducing skin tones of the 3D printed models,
- To improve the quantitative method for evaluating colour quality of 3D printed objects.

1.3 Thesis Structure

In this thesis, eight chapters are included and organised as below:

Chapter 1: Introduction

The present chapter gives an introduction to this study by providing an overview of the research background, outlining the research aim and objectives, and describing the structure of the thesis.

Chapter 2: Literature Survey

In this chapter, literatures relevant to this research were reviewed, covering the fields of colour science, image science, 3D printing and psychophysics. Specifically, it includes the basic knowledge of CIE colorimetry, an overview of skin and skin colour, colour measurement using digital cameras, colour production in 3D printing. In addition, the techniques for conducting psychophysical experiments and the statistical measures for data analysis were presented in this chapter.

Chapter 3: Methodology

This chapter describes the methodology applied to achieve the aim and objectives of this research, including the 3D colour image reproduction workflow developed for human faces, the apparatus used in this study, the process of colour management in the workflow, and the evaluation of skin colour reproduction.

Chapter 4: Image Measurement for Human Face

This chapter begins by developing a specific 2D imaging system for capturing human faces and investigating the factors affecting the camera colour characterisation model for achieving accurate skin colour reproduction, followed by a case study on the investigation of skin colour heterogeneity under six illuminations different with CCTs. Moreover, the colour characterisation was performed on the 3D imaging system for accurate colour image acquisition.

Chapter 5: Colour Characterisation for the 3D Printer

This chapter focuses on the colour characterisation methods for the 3D printer to achieve higher accuracy of colour reproduction by comparing different methods and output variables. In practice, a printer colour profile with good performance was developed using a specific skin colour chart, and the colour reproduction accuracy of the 3D printer was significantly improved.

Chapter 6: Colour-Difference Evaluation of 3D printed objects

Psychophysical experiments were conducted using the method of Grey Scale to investigate the visual colour perception of 3D printed samples in lightness, chroma and hue dimensions. Based on the collected visual colour-difference data, the performance of CIELAB and CIEDE2000 colour-difference formulae was tested for 3D objects. Furthermore, the parametric factors in the colour-difference formulae were optimised to better fit the visual results of 3D samples.

Chapter 7: Implementation of 3D Colour Reproduction of a human face

Based on the 3D colour image reproduction workflow, the practice of reproducing a human face from 3D imaging to colour 3D printing was carried out using the developed colour management procedure and specific colour quality assessment method.

Chapter 8: Conclusions

The last chapter summarises the findings of this study and provides suggestions for future work.

Chapter 2
Literature Survey

2.1 CIE Colorimetry

In 1931, the *Commission Internationale de l'Éclairage* (CIE) established the first major recommendations on colorimetric standards, which were developed as the fundamental in the research field of colour science. The CIE colour specifications, colour difference formulae and colour appearance model have been introduced to provide recommendations and guidance on colour communication in various industrial applications. Therefore, it is crucial to understand CIE colorimetry for performing colour measurement and colour evaluation.

2.1.1 CIE Standard Colorimetric Observers

The mechanism of how colours are perceived by human eyes has been studied, and it was found that there are two types of photoreceptors in the retina of the eye: rods, which are highly sensitive to light and active at very low levels of light, and cones, which are capable of colour vision and active in a relatively bright environment (CIE 2018). Furthermore, there are three types of cones responding to long-, medium-, short-wavelength light, respectively, and the spectral sensitivities were be quantified by using a set of three functions, known as cone fundamentals (CIE 2006a).

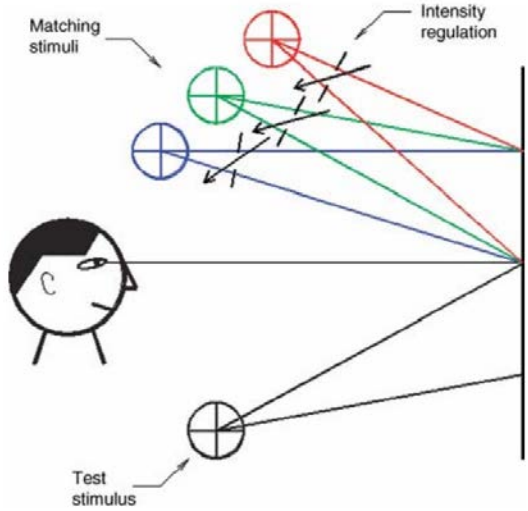

Figure 2.1 Basic experiment setup for colour matching (CIE 2006).

Considering that it is complicated to measure the cone fundamentals of the eye, a set of colour matching functions (CMFs) were derived to represent the average properties of human observers with normal colour vision, based on matching colours by the addition of different amounts of red, green, and blue (RGB) lights. Figure 2.1 illustrates the basic experiment setup for colour matching. The CIE 1931 and 1964 standard colorimetric observers were established for two different fields of view with respect to the observer's eye.

2.1.1.1 CIE 1931 CMFs

The CIE 1931 standard colorimetric observer, also known as the CIE 2° standard colorimetric observer $\bar{x}_2(\lambda)$, $\bar{y}_2(\lambda)$, $\bar{z}_2(\lambda)$ in technical applications, was established based on the results of two colour matching experiments with an approximately 2° bipartite field conducted separately by W.D. Wright (Wright 1929, 1930), and J. Guild (Guild 1931). In order to define a standard observer, the CIE system used three primaries of red at the wavelength of 700 nm, green at 546.1 nm and blue at 435.8 nm to normalise the Wright and Guild experimental data, and a matrix transformation was applied to the RGB colour matching functions to avoid the negative values and reduce the complexity. Figure 2.2 shows the colour matching functions of the CIE 1931 standard colorimetric observer which is recommended for small viewing fields between 1° to 4° (CIE 2018). A 2° visual field represents a diameter of about 17 mm at a viewing distance of 50 cm (CIE 2018).

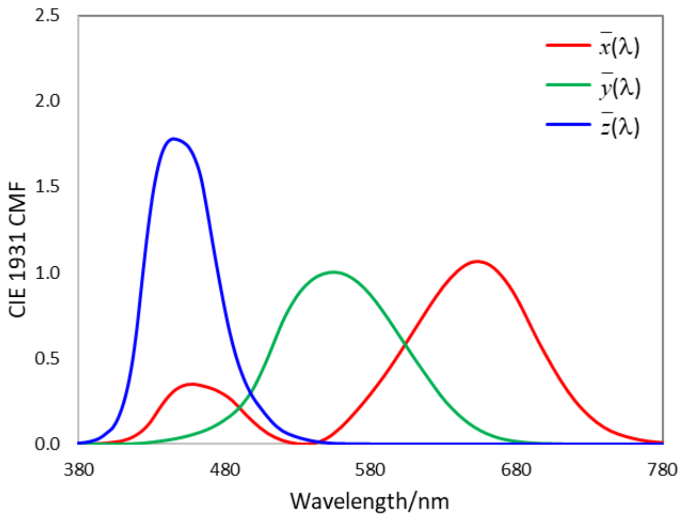

Figure 2.2 CIE 1931 colour matching functions.

2.1.1.2 CIE 1964 CMFs

For the application of larger viewing fields, the CIE 1964 supplementary standard colorimetric observer, also named as the CIE 10° standard colorimetric observer $\bar{x}_{10}(\lambda)$, $\bar{y}_{10}(\lambda)$, $\bar{z}_{10}(\lambda)$, was derived from the results of two colour matching studies with a 10° bipartite field conducted by Speranskaya (1959) and Stiles and Burch (1959). A 10° visual field represents a diameter of about 90 mm at a viewing distance of 50 cm (CIE 2018). Judd (1993) performed the final transformation and derived the CIE 1964 standard colorimetric observer. Figure 2.3 plots the CIE 1964 colour matching functions recommended for a viewing field larger than 4°.

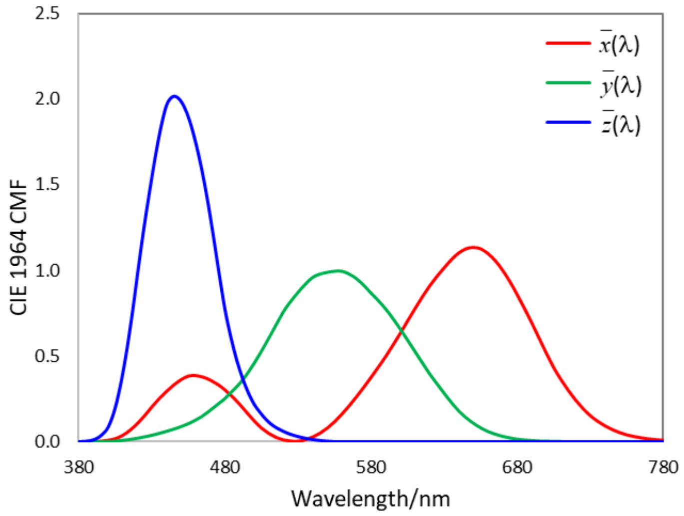

Figure 2.3 CIE 1964 colour matching functions.

2.1.2 CIE Illuminants and Sources

Light sources play an important role in colorimetry. Normally, there is no colour without light. For self-luminous colours, such as a candle or a firework, the light source itself is the colour stimulus. The radiation of a light source can be described by the spectral power distribution (SPD), which represents the radiant power per unit area per unit wavelength of an illumination (Ohta and Robertson 2006). It is a function of wavelength, typically ranging from 380 nm to 780 nm in the visible electromagnetic spectrum. When the radiation at the wavelength of 560 nm of the function is normalised as 100, it is called the relative spectral power distribution.

Colour temperature is the colour of light emitted by a theoretical black body, also called a Planckian radiator, that absorbs all incident radiation. It is usually expressed in Kelvins (K). For light sources whose chromaticities are near, but not exactly on the Planckian locus, it is often to quote the temperature of the Planckian radiator that mostly resembles the colour of the light, and this is called correlated colour temperature (CCT). In order to reproduce colorimetric measurements, the CIE has standardised a series of SPDs: A, B, C, D, E and F, representing incandescent lights, phases of daylight, fluorescent lamps and high pressure discharge lamps, respectively. They were derived from theoretical data and referred as CIE illuminants (CIE 2018). The practical realisations of a CIE illuminant are called CIE sources, and it is referred to as a simulator in most cases that an illuminant cannot be reproduced accurately. Figure 2.4 illustrates the loci of the Planckian radiator, CIE illuminants and some colour temperatures in the $u'v'$ uniform chromaticity diagram.

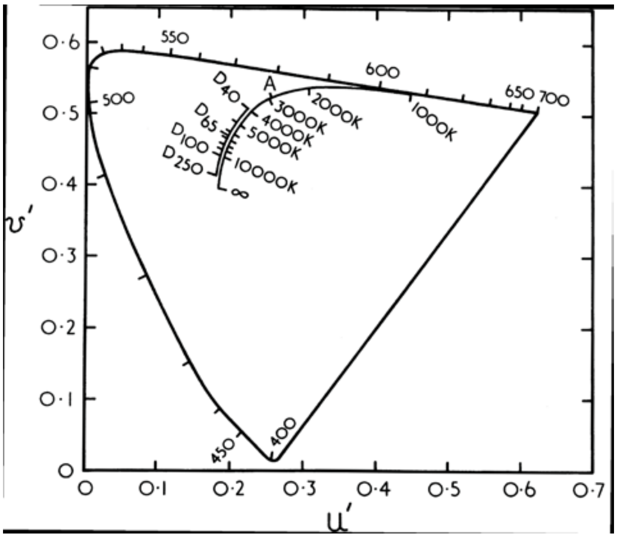

Figure 2.4 The loci of the Planckian, CIE illuminants and some colour temperatures plotted in the $u'v'$ chromaticity diagram (Hunt 2004).

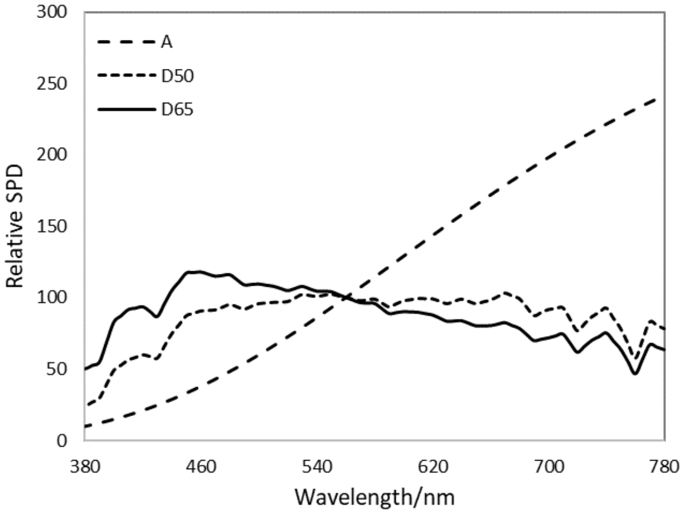

Figure 2.5 The relative spectral power distributions of CIE standard illuminants A, D50 and D65.

Previously CIE defined two standard illuminants: A and D65, and a new standard illuminant D50 with a CCT of approximately 5000 K has been included in 2022 due to its extensive use in the fields of graphic, arts and photography (ISO/CIE 2022). CIE standard illuminant A has a CCT of approximately 2856 K, which is intended to represent typical tungsten-filament lighting and recommended in all applications that involve the use of incandescent lighting. CIE standard illuminant D65 has a CCT of approximately 6500 K, and it is intended to represent average daylight and can be used in all colorimetric calculations requiring representative outdoor daylight. Figure 2.5 plots the relative SPDs of CIE standard illuminants A, D50 and D65.

2.1.3 CIE Standard Measurement Geometry

In order to quantify the colorimetric characteristics of an object, it is not enough to define a standard observer and a standard illuminant, the measuring geometry has to be defined as well. The CIE specifies four measuring geometries for reflectance measurements: 0°:45°, 45°:0°, 8°:d and d:8° (CIE 2018), as shown in Figure 2.6. With the 0°:45° arrangement, the test sample is illuminated at an angle of 0° and the reflected light is detected at 45°. For 45°:0° measurement, the device illuminates the samples at 45° and detects the reflected light at 0°. In practice, these two types of measurement geometries, 0°:45° and 45°:0°, are widely used in the graphic arts industry, while the 45°:0° geometry may give rise to problems due to polarisation (Samanta and Das 1992).

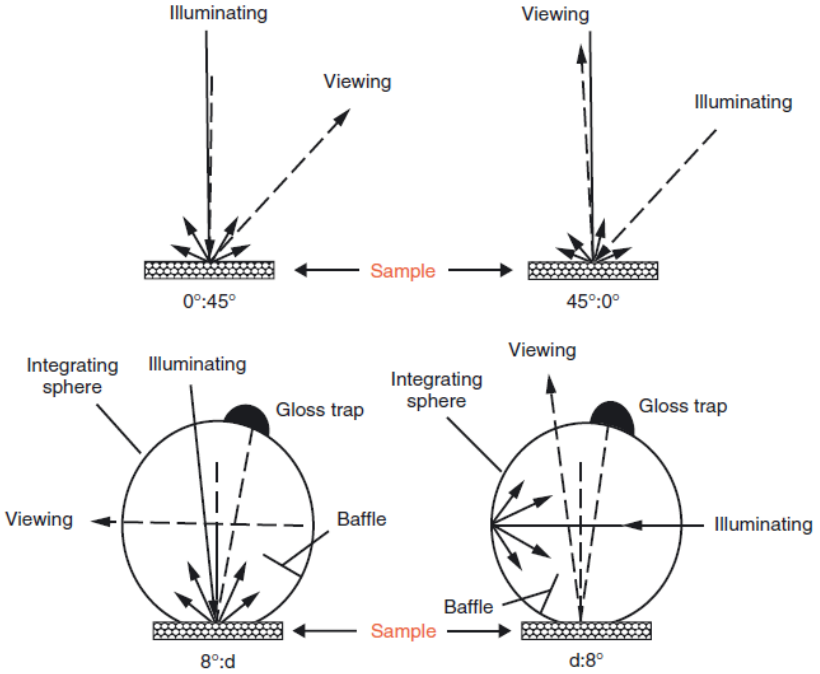

Figure 2.6 Schematic diagrams of the four CIE recommended geometries of illumination and measurement (Hunt and Pointer 2011).

In the case of diffuse instrument geometries (8°:d and d:8°), a baffle is provided in the integrating sphere to prevent direct light from the sample falling on the detector, and a gloss trap is used to include or exclude the specular component (SCI/SCE). In the SCI measurement mode, the specular reflectance is included with the diffuse reflectance. It is used to measure the colour of an object without the influence of surface conditions.

When using the SCE measurement mode, the specular reflectance is excluded from the measurement and only the diffuse reflectance is measured. This type of measurement is used to evaluate colour of an object which correlates to visual perception. Some instruments can measure both SCE and SCI reflectance data simultaneously. It is necessary to consider these criteria and decide the suitable measurement mode, SCI or SCE, according to the object surface conditions.

Generally, the illumination and viewing conditions play a significant role in colour measurement, it is important to select an appropriate measurement geometry that represents the viewing conditions of the target sample in the particular application. For partly glossy or textured samples, the preferred geometry is the one that minimises the surface effects (ASTM 2008).

2.1.4 CIE Colour Spaces

2.1.4.1 CIE XYZ and CIE $xy\mathrm{Y}$ Colour Space

As shown in Figure 2.7, the perception of colour is generated by three components: the spectral power distribution of the light source, the optical properties of the surface of an object, and the response of the human colour vision system which is characterised by colour matching functions. According to the CIE recommendations (CIE 2018), a colour stimulus can be quantified by the integration of these three components, as expressed in the following equation:

$$
\begin{aligned}
X &= k\sum_{\lambda} S(\lambda)\rho(\lambda)\,\bar{x}(\lambda)d\lambda \\
Y &= k\sum_{\lambda} S(\lambda)\rho(\lambda)\,\bar{y}(\lambda)d\lambda \\
Z &= k\sum_{\lambda} S(\lambda)\rho(\lambda)\,\bar{z}(\lambda)d\lambda
\end{aligned}
\tag{2.1}
$$

where X, Y, Z are the CIE XYZ tristimulus values, λ is the wavelength usually ranging from 380 nm to 780 nm or 400 nm to 700 nm, k is a constant to normalize the Y values as 100 for the reference white and $k = 100/\sum_{\lambda} S(\lambda)\rho(\lambda)\,\bar{y}(\lambda)d\lambda$, $S(\lambda)$ indicates the spectral power distribution of the light source, $\rho(\lambda)$ denotes an object's spectral reflectance, $\overline{x}(\lambda)$, $\overline{y}(\lambda)$, $\overline{z}(\lambda)$ represent the average spectral responses of the human colour vision system, either the CIE 1931 standard observer for 1° to 4° small visual field, or the CIE 1964 standard observer for a visual field larger than 4°, $d\lambda$ is an interval of the spectral wavelength, usually assigned as 1 nm, 5 nm or 10 nm (CIE 2018). For self-luminous objects, the $S(\lambda)\rho(\lambda)$ in Equation (2.1) can be expressed as $\Phi(\lambda)$, which denotes the colour stimulus function of the light seen by the observer.

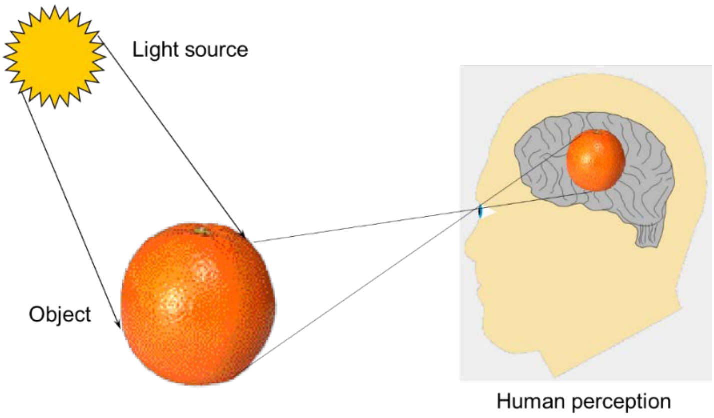

Figure 2.7 An example of how human see colours.

Although a colour stimulus can be described by using CIE XYZ tristimulus values, it is difficult to associate these numbers with the visual perception of the actual colour stimulus. The CIE XYZ colour space was designed to divide the conception of colour into two sections: the luminance factor indicated by the Y value with the maximum of 100, and the chromaticity diagram specified by xy coordinates. The CIE x, y, z chromaticity coordinates are defined as:

$$x = \frac{X}{X+Y+Z}$$
$$y = \frac{Y}{X+Y+Z} \tag{2.2}$$
$$z = \frac{Z}{X+Y+Z}$$

where $x + y + z = 1$, so it is simple to calculate the third one given any two of these three values. The two-dimensional xy chromaticity diagram, as shown in Figure 2.8 (left), is often used to plot colour coordinates. The luminance factor Y of the tristimulus values is usually used to specify a colour with xy chromaticity coordinates, known as the CIE $xy\mathrm{Y}$ colour space.

However, it was found that equal colour differences computed by Euclidean distance in different regions of the colour space are not perceptually equal (Wright 1941). MacAdam reported that the chromaticity difference corresponding to a just noticeable colour difference will be different in different areas of the xy chromaticity diagram, and the equal chromaticity differences in different directions represent different colour-difference magnitudes (MacAdam 1942). Figure 2.8 (right) shows the MacAdam's ellipses as 10 times just noticeable chromaticity differences in the CIE xy

chromaticity diagram, and it can be clearly seen that this space is non-uniform with the largest colour differences in green colours. These ellipses are expected to be circles of the same radius in the chromaticity diagram if the colour space is completely uniform.

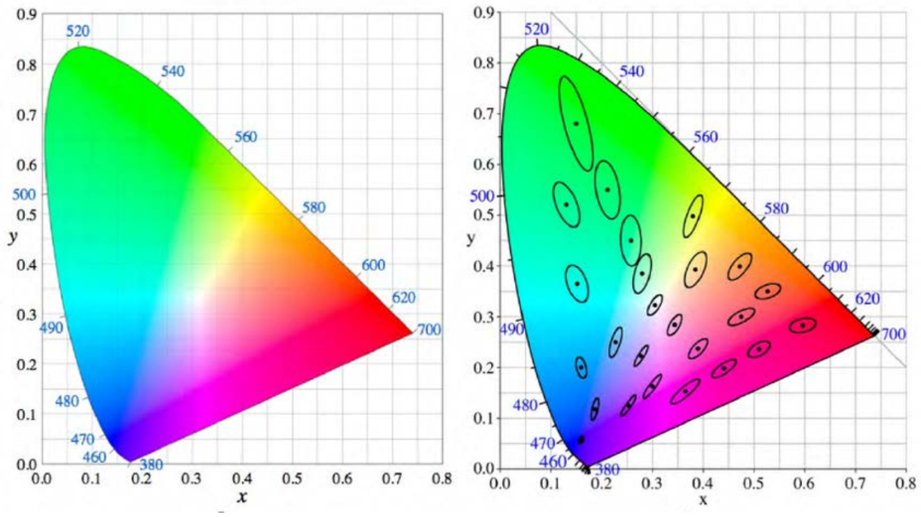

Figure 2.8 CIE 1931 xy chromaticity diagram with the spectral locus and wavelengths shown in nanometres (left) and MacAdam's ellipses ten times their actual sizes (right) (Małgorzata 2010).

2.1.4.2 CIE 1976 Uniform Colour Space

To improve the visual uniformity, a new chromaticity diagram, the CIE 1976 uniform chromaticity scale diagram, was introduced by CIE, as shown in Figure 2.9 (left). The $u'v'$ coordinates can be calculated as follows:

$$u' = \frac{4x}{-2x + y + 3} = \frac{4X}{X + 15Y + 3Z}$$
$$v' = \frac{9x}{-2 + 12y + 3} = \frac{9Y}{X + 15Y + 3Z} \qquad (2.3)$$

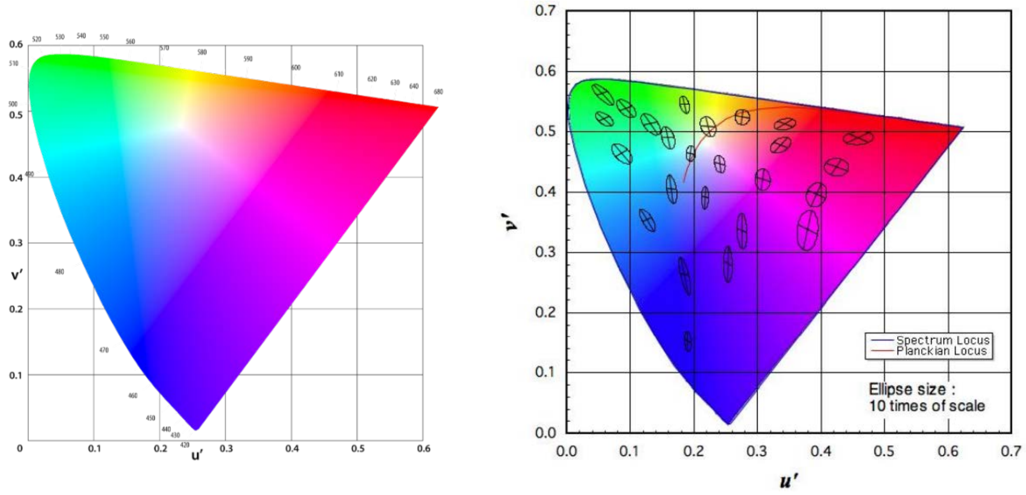

Figure 2.9 CIE 1976 $u'v'$ chromaticity diagram (left) and MacAdam ellipses 10-times of scale plotted (right).

Figure 2.9 (right) shows the MacAdam ellipses converted into the CIE $u'v'$ chromaticity diagram, and it is clear that the uniformity of the ellipses is improved compared to the CIE xy chromaticity diagram (Figure 2.8), but it is still imperfect. The CIE $u'v'$ chromaticity diagram is often used to describe the chromaticities of light sources. Examples are the definition of colour temperature as described in Section 2.1.2 (Figure 2.4).

Based on the $u'v'$ chromaticity diagram, the CIELUV or CIE $L^*u^*v^*$ uniform colour space was developed, which is sometimes used in industrial applications that depend on the additive mixing of light, such as colour television, illumination and video monitor, to specify self-luminous colour stimuli (Ohta and Robertson 2005). The equations to calculate the three coordinates in the CIELUV colour space are expressed:

$$\begin{aligned} L^* &= 116f\left(\frac{Y}{Y_n}\right) - 16 \\ u^* &= 13L^*(u' - u'_n) \\ v^* &= 13L^*(v' - v'_n) \end{aligned} \tag{2.4}$$

where $u', v'$are the CIE 1976 uniform chromaticity scale diagram coordinate of the test stimulus, u'_n, v'_n are those of a specified reference white, f is a function expressed as:

$$f(\omega) = \begin{cases} \omega^{1/3} & \omega > (24/116)^3 \\ (841/108)(\omega) + 16/116 & \omega \leq (24/116)^3 \end{cases} \tag{2.5}$$

The most widely used uniform colour space is the CIELAB or CIE $L^*a^*b^*$ colour space (CIE 1975). The lightness L^* coordinate is the same as that in the CIELUV colour space, the other two coordinates can be calculated from CIE XYZ tristimulus values using the following equation:

$$\begin{aligned} a^* &= 500\left[f\left(\frac{X}{X_n}\right) - f\left(\frac{Y}{Y_n}\right)\right] \\ b^* &= 200\left[f\left(\frac{Y}{Y_n}\right) - f\left(\frac{Z}{Z_n}\right)\right] \end{aligned} \tag{2.6}$$

where X_n, Y_n, Z_n are the tristimulus values of the reference white, and the function f is as given by Equation (2.5).

In CIELAB colour space, as shown in Figure 2.10, the attribute of L^* represents the perceived lightness, the larger the L^* value, the higher the lightness of the stimulus. The a^* axis points approximately in the direction of red-green colour stimulus, where the positive values of a^* attribute indicate reddish colours while negative a^* values denote greenish colours. The axis of b^* indicates the direction of yellow-blue colour stimulus, where positive b^*

is more yellowish and negative b^* is more bluish. Consequently, the a^*b^* diagram is divided into four quadrants by a^*, b^* axis, and each represents different colour regions. The CIELAB uniform colour space is recommended for describing the colour of an object surface (Malacara 2003), widely used in colour applications such as the colourant and graphic art industries.

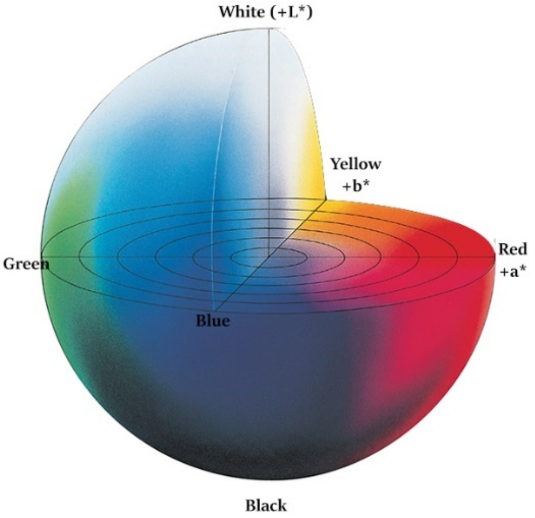

Figure 2.10 The schematic diagram of CIELAB colour space.

Additionally, there are two more perceived attributes, the chroma C^*_{ab}, representing the colourfulness of an object, and the hue angle h_{ab}, representing its proportions of red, green, yellow, blue colour. They can be derived from the a^*b^* coordinates by using the following equation:

$$C^*_{ab} = \sqrt{a^{*2} + b^{*2}}$$
$$h_{ab} = \arctan\left(b^*/a^*\right) \tag{2.7}$$

The CIELAB hue angle h_{ab} shall lie between 0° and 90° if a^* and b^* values are both positive, between 90° and 180° if a^* value is negative and b^* value is positive, between 180° and 270° if $a^*$and b^* values are both negative, between 270° and 360° if a^* value is positive and b^* value is negative. The term of the hue angle h_{ab} does not have a "*" symbol because pairs of colours with constant hue angle difference change their perceived colour difference with variation of chroma (Schanda 2007).

2.1.5 Colour-Difference Formulae

The evaluation of colour difference ($\Delta\mathrm{E}$) between two colour stimuli is an important topic in colorimetry and the formulae developed based on CIE XYZ tristimulus values are widely used in industrial applications. Note that the prerequisite of applying colour-difference formulae is to ensure both colour stimuli are viewed under the same viewing conditions and identical reference white. The reference conditions for applications are recommended by CIE (2006) and listed in Table 2.1.

Table 2.1 CIE recommended reference conditions.

Conditions	CIE Recommendation
Illumination	Source simulating D65
Illuminance	1000lx
Observer	With normal colour vision
Background field	Uniform, neutral grey with $L^* = 50$
Viewing mode	Object
Samples size	Greater than 4° subtended visual angle
Sample separation	Minimum, sample pairs with direct edge contact
Magnitude of $\Delta\mathrm{E}$	0 to 5 CIELAB units
Sample structure	Homogeneous without apparent pattern or non-uniformity

2.1.5.1 CIE 1976 Colour-Difference Formula

It is known that CIELUV colour space is mainly used for the television and illumination industries, and CIELAB colour space for the surface colourant industries (Hunt and Pointer 2011). Based on these two colour spaces, the associated colour-difference formulae have been widely utilised to quantify the perceived colour difference between a pair of colour samples.

The simplest colour-difference formula is quantified as the Euclidean distance between two colour stimuli's coordinates in CIELUV or CIELAB colour space, denoted as CIELUV (ΔE^*_{uv}) or CIELAB (ΔE^*_{ab}) colour difference, the calculation formulae are expressed as:

$$\Delta E^*_{uv} = \sqrt{(\Delta L^*)^2 + (\Delta u^*)^2 + (\Delta v^*)^2} \tag{2.8}$$

$$\Delta E^*_{ab} = \sqrt{(\Delta L^*)^2 + (\Delta a^*)^2 + (\Delta b^*)^2} = \sqrt{(\Delta L^*)^2 + (\Delta C^*_{ab})^2 + (\Delta H^*_{ab})^2} \tag{2.9}$$

where ΔL^*, Δu^*, Δv^*, Δa^*, Δb^*, ΔC^*_{ab} correspondingly indicate the difference of L^*, u^*, v^*, a^*, b^*, C^*_{ab} coordinates of two colour stimuli with subscripts 0 and 1, ΔH^*_{ab} means hue difference which is defined as:

$$\Delta H^*_{ab} = 2\sin\,(\Delta h_{ab}/2)\sqrt{C^*_{ab,0}C^*_{ab,1}} \tag{2.10}$$

As noted in Section 2.1.4.2, Δh_{ab} is not correlated to the perceptual magnitude of a difference in hue, and it may happen that the line joining the two colours crosses the $+a^*$ axis, in which case the value of Δh_{ab} should be corrected by adding or subtracting 360°. Instead, ΔH^*_{ab} is used for the calculation of CIELAB colour-difference formula.

Considering that the CIELAB colour space is not perfectly uniform, several colour-difference formulae were developed to further improve the uniformity of the colour difference metric, such as the CMC $(l{:}c)$ colour-difference formula for the textile colouration industries (Clarke et al. 1984), the BFD$(l{:}c)$ developed by Luo and Rigg (1987), the CIE94 colour-difference formula for small colour difference (CIE 1995), and the CIEDE2000 colour-difference formula (Luo et al. 2001). Due to the simplicity of the calculation in CIELAB colour-difference formula, it is still widely used for colour quality evaluation.

2.1.5.2 CIEDE2000 Colour-Difference Formula

The CIEDE2000 colour-difference formula was developed by Luo et al. (2001) to improve the perceptual uniformity, based on four reliable colour discrimination datasets collected from object colours: *BFD-P* (Luo 1987a, 1987b), *RIT–DuPont* (Alman et al. 1989, Berns et al. 1991), *Leeds* (Kim and Nobbs 1997), and *Witt* (1999). This formula is jointly recommended as a standard by the CIE and the *International Organization for Standardization* (ISO) (ISO/CIE 2014). The CIEDE2000 colour-difference formula is expressed as:

$$\Delta \mathrm{E}_{00} = \sqrt{(\frac{\Delta L'}{k_L S_L})^2 + (\frac{\Delta C'}{k_C S_C})^2 + (\frac{\Delta H'}{k_H S_H})^2 + R_T(\frac{\Delta C'}{k_C S_C})^2(\frac{\Delta H'}{k_H S_H})^2} \tag{2.11}$$

where $\Delta L'$, $\Delta C'$, $\Delta H'$ are the lightness, chroma and hue differences between two colour stimuli subscripted as 0 and 1 (see Equation 2.12), k_L, k_C, k_H are the parametric factors accounting for the influence of the illuminating and viewing conditions ($k_L = k_C = k_H = 1$ under so-called ‘reference conditions’ (Table 2.1) for most applications, and $k_L = 2, k_C = k_H = 1$ for textiles), S_L, S_C, S_H are the lightness, chroma and hue weighting functions (see Equation 2.13), R_T is a new interactive function (see Equation 2.14) between chroma and hue differences to improve the performance of the colour-difference formula for fitting chromatic difference data in the blue region.

The lightness weighting function S_L in CIEDE2000 colour-difference formula was corrected as new data on lightness differences were collected in the database. The chroma weighting function S_C is equivalent to that in CIE94, which aimed to reduce the effect of chroma differences linearly with increasing chroma. For the new hue weighting function S_H, a T function is included in the calculation to cope with the complex hue-dependence.

Since it was found that CIELAB-based formulae gave a poor fit to the chromatic differences close to neutral, a scaling factor G was introduced to CIELAB a^* scale in CIEDE2000 to improve the performance for neutral colours. Compared to the CIELAB colour-difference formula, the calculation of CIEDE2000 colour-difference formula is more complex, and the details are as follows (CIE 2001):

Step 1. Calculate the CIELAB values (see Equation 2.4-2.6).

Step 2. Calculate $\Delta L'$, $\Delta C'$ and $\Delta H'$:

$$\begin{gathered} \Delta L' = L'_1 - L'_0 \\ \Delta C' = C'_1 - C'_0 \\ \Delta H' = 2\sqrt{C'_1 C'_0}\sin(\tfrac{h'_1 - h'_0}{2}) \end{gathered} \tag{2.12}$$

where

$$L' = L^*$$

$$C' = \sqrt{a'^2 + b'^2}$$

$$h' = tan^{-1}(b'/a')$$

where

$$a' = (1 + G)a^*$$

$$b' = b^*$$

where

$$G = 0.5[1 - \sqrt{\tfrac{(C^*_{ab} + C^*_{ab,1})}{2}^7 / (\overline{C^*_{ab}}^7 + 25^7)}].$$

Step 3. Calculate lightness, chroma, hue weighting functions S_L, S_C, S_H:

$$\begin{gathered} S_L = 1 + \frac{0.015\left(\frac{L'_1 + L'_0}{2} - 50\right)^2}{\left[20 + \left(\frac{L'_1 + L'_0}{2} - 50\right)^2\right]^{\frac{1}{2}}} \\ S_C = 1 + \frac{0.045(C'_1 + C'_0)}{2} \\ S_H = 1 + \frac{0.015(C'_1 + C'_0)}{2}T \end{gathered} \tag{2.13}$$

where T is

$$T = 1 - 0.17\,cos\left[\frac{(h_1' + h_2')}{2} - 30^{\circ}\right] + 0.24cos(h_1' + h_2') + 0.32\cos\,[\frac{3(h_1' + h_2')}{2} + 6^{\circ}] - 0.20\cos\,[2(h_1' + h_2') - 63^{\circ}]$$

Step 4. Calculate R_T:

$$R_T = -\sin(2\Delta\theta) * R_C \tag{2.14}$$

where

$$\Delta\theta = 30\exp\,\{-[\frac{\frac{(h_1' + h_2')}{2} - 275^{\circ}}{25}]^2\}$$

$$R_C = 2\sqrt{\frac{(C_1' + C_0')}{2}{}^7 / \,(\frac{(C_1' + C_0')}{2}{}^7 + 25^7)}.$$

Step 5. Calculate CIEDE2000 $\Delta\mathrm{E}_{00}$ (see Equation 2.11).

2.1.6 Colour Appearance Model

CIE colorimetry has been successfully applied in industries since it was proposed in 1931, however, it can only be used under limited viewing conditions, e.g., daylight illuminant, high luminance, grey background and standardised viewing/illuminating geometries. When the same sample is presented under two different conditions, the colour sensation perceived by human eyes could be different.

With the rapid development of digital imaging technologies and increasing demands on cross-media colour reproduction, basic colorimetry is becoming insufficient, and a colour appearance model (CAM) is required to predict colour appearance across a wide range of viewing conditions.

2.1.6.1 CIECAM02

In 2002, a new colour appearance model, CIECAM02, was introduced and recommended by CIE (Moroney 2002, CIE 2004). Its development was based on CIECAM97s (CIE 1998, Luo and Hunt 1998) and it gives better agreement with experimental data. The schematic diagram of a colour appearance model can be simply shown in Figure 2.11 with the viewing parameters shown in the shaded area. The inputs X, Y, Z are CIE XYZ tristimulus values of the colour stimulus, X_W, Y_W, Z_W are the tristimulus values of the reference white under the test illuminant, L_A indicates the luminance of the adapting field (Fairchild 2005); Y_b denotes the luminance factor of the background, the surround conditions are described by ‘average’, ‘dim’ and ‘dark’ conditions in Table 2.2.

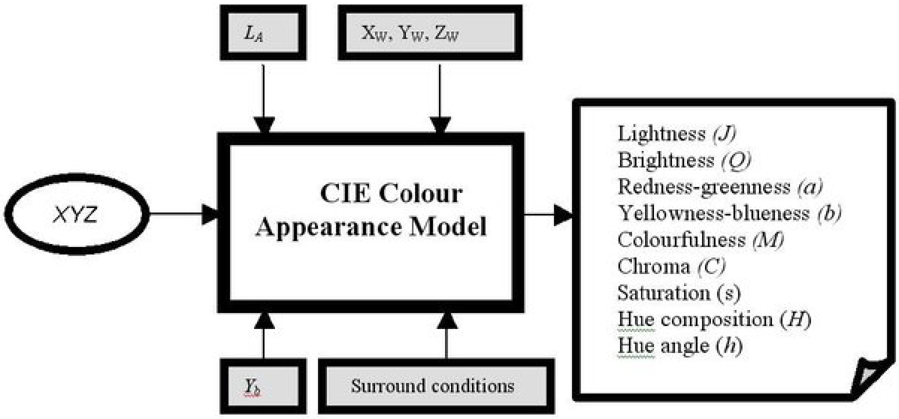

Figure 2.11 The schematic diagram of a CIE colour appearance model (CIE, 2004).

Table 2.2 Input parameters for the CIECAM02 model.

Viewing conditions	c	N_c	F
Average	0.69	1.0	1.0
Dim	0.59	0.9	0.9
Dark	0.525	0.8	0.8

There are many outputs from the CIECAM02 model describing the colour appearance attributes, such as lightness J, brightness Q, colourfulness M, chroma C, hue composition H, etc. In addition to the forward model (Figure 2.11), there is a reverse model aiming to transform human perceptual attributes back to tristimulus values, mainly recommended for applications in colour management. More details about the forward and reverse models of CIECAM02 can be found in the reference of CIE, 2004 and Xiao, 2006.

One of the most important improvement of CIECAM02 as a refinement of CIECAM97s is the use of a linear chromatic adaptation transform (CAT), known as CAT02, to simplify the model. The chromatic adaptation transform aims to enable the human visual system to adjust to widely varying colour of illumination in order to approximately preserve the appearance of object colour. In CAT02, a transform matrix, M_{CAT02}, was determined to convert CIE XYZ tristimulus values to RGB cone responses, as expressed in Equation 2.15. The matrix was normalised so that the tristimulus values for the equal-energy illuminant $(X = Y = Z = 100)$ produce equal cone responses $(L = M = S = 100)$. In addition, a factor denoting the degree of chromatic adaptation, D, is calculated using Equation (2.16) based on the adapting luminance L_A and surround factor F in Table 2.2.

$$\begin{pmatrix} R \\ G \\ B \end{pmatrix} = M_{CAT02} \begin{pmatrix} X \\ Y \\ Z \end{pmatrix} \tag{2.15}$$

where

$$M_{CAT02} = \begin{pmatrix} 0.7328 & 0.4296 & -0.1624 \\ -0.7036 & 1.6975 & 0.0061 \\ 0.0030 & 0.0136 & 0.9834 \end{pmatrix}.$$

$$D = F\left[1 - \left(\frac{1}{3.6}\right) e^{\left(\frac{-L_A-42}{92}\right)}\right] \tag{2.16}$$

Based on the CIECAM02 output attributes, a colour space $J'a'_Mb'_M$ was developed to fit all available datasets. The colour difference between two samples can be calculated in this space using Equations (2.17-2.21). Moreover, three colour spaces named CAM02-SCD, CAM02-LCD and CAM02-UCS were developed for small, large, and combined small and large colour differences, respectively, to better describe human perceptual attributes. The coefficients for each CIECAM02 based colour space and the corresponding colour-difference formulae are listed in Table 2.3.

$$J' = \frac{(1 + 100c_1)J}{1 + c_1J} \tag{2.17}$$

$$M' = (1/c_1)ln(1 + c_2M) \tag{2.18}$$

$$a'_M = M'cos(h) \tag{2.19}$$

$$b'_M = M'sin(h) \tag{2.20}$$

$$\Delta E' = \sqrt{(\Delta J'/K_L)^2 + (\Delta a'_M)^2 + (\Delta b'_M)^2} \tag{2.21}$$

Table 2.3 The coefficients for each CIECAM02 based colour space and the corresponding colour-difference formulae.

	CAM02-SCD	CAM02-LCD	CAM02-UCD
K_L	1.24	0.77	1.00
c_1	0.007	0.007	0.007
c_2	0.0363	0.0053	0.0228

Overall, the CIECAM02 colour appearance model has been widely used in academic research and industrial applications since it was recommended by CIE in 2002. However, it was reported that CIECAM02 has problems when predicting the lightness perceptual attribute for certain colour samples (Süsstrunk and Brill 2006, Brill and Süsstrunk 2007), and the predicted corresponding colours with negative tristimulus values (Li et al. 2007). In light of the above, a CIE technical committee: CIE TC8-11 on CIECAM02-

Mathematics was established in 2007 to improve the performance of CIECAM02.

2.1.6.2 CIECAM16

Li et al. (2017) proposed a new transform matrix, M_{16}, by changing the original structure of the CIECAM02 model, resulting in a new CAT named CAT16. A new colour appearance model, CAM16, was developed by combining the chromatic and luminance adaptations in the same space instead of in two different spaces. It was tested using the colour appearance datasets and proved that the CAM16 model performed better than the CIECAM02 in predicting the colourfulness and hue composition. Moreover, a CIE Technical Report was published in 2022 to recommend the CAM16 model, now known as CIECAM16 (CIE 2022), to replace the CIECAM02 model for colour management systems that involve related colours, e.g., the evaluation of photographic prints, self-luminous displays, and generally in the imaging industries.

Given a colour stimulus with known XYZ values under a test illuminant with known X_w, Y_w, Z_w values and the parameters for the surround (see Table 2.2), the calculation of the CIECAM16 forward model is as follows:

Step 1: Calculate RGB cone responses:

$$\begin{pmatrix} R \\ G \\ B \end{pmatrix} = M_{16} \begin{pmatrix} X \\ Y \\ Z \end{pmatrix}, \begin{pmatrix} R_w \\ G_w \\ B_w \end{pmatrix} = M_{16} \begin{pmatrix} X_w \\ Y_w \\ Z_w \end{pmatrix} \tag{2.22}$$

where

$$M_{16} = \begin{pmatrix} 0.401288 & 0.650173 & -0.051461 \\ -0.250268 & 1.204414 & 0.045854 \\ 0.002079 & 0.048952 & 0.953127 \end{pmatrix}$$

Step 2: Complete the colour adaptation of the illuminant in the corresponding cone response space:

$$\begin{pmatrix} R_C \\ G_C \\ B_C \end{pmatrix} = \begin{pmatrix} D_R R \\ D_G G \\ D_B B \end{pmatrix}, \begin{pmatrix} R_{cw} \\ G_{cw} \\ B_{cw} \end{pmatrix} = \begin{pmatrix} D_R R_w \\ D_G G_w \\ D_B B_w \end{pmatrix} \tag{2.23}$$

where

$$D_R = D\frac{Y_W}{R_W} + 1 - D$$

$$D_G = D\frac{Y_W}{G_W} + 1 - D$$

$$D_B = D\frac{Y_W}{B_W} + 1 - D$$

where D is the degree of adaption which is the same as that in CIECAM02 model (see Equation 2.16).

Step 3: Calculate the post adaptation cone responses:

$$R_a = 400\left[\frac{(F_L R_c/100)^{0.42}}{(F_L R_c/100)^{0.42} + 27.13}\right] + 0.1$$

$$G_a = 400\left[\frac{(F_L G_c/100)^{0.42}}{(F_L G_c/100)^{0.42} + 27.13}\right] + 0.1 \tag{2.24}$$

$$B_a = 400\left[\frac{(F_L B_c/100)^{0.42}}{(F_L B_c/100)^{0.42} + 27.13}\right] + 0.1$$

where

$$F_L = 0.2k^4(5L_A) + 0.1(1 - k^4)^2(5L_A)^{1/3}$$

where

$$k = \frac{1}{5L_A + 1}$$

If R_a is negative, then

$$R_a = -400\left[\frac{(F_L R_c/100)^{0.42}}{(F_L R_c/100)^{0.42} + 27.13}\right] + 0.1$$

The R_{aw}, G_{aw}, B_{aw} can be calculated from R_{cw}, G_{cw}, B_{cw} in the same way.

Step 4: Calculate the redness-greenness a, yellowness-blueness b and hue angle h (between 0° and 360°):

$$a = R_a - \frac{12G_a}{11} + \frac{B_a}{11} \tag{2.25}$$

$$b = \frac{(R_a + G_a - 2B_a)}{9} \tag{2.26}$$

$$h = tan^{-1}(\frac{b}{a}) \tag{2.27}$$

Step 5: Using the following unique hue data in Table 2.4, set $h' = h + 360$ if $h < h_1$, otherwise $h' = h$, and choose a proper i ($i = 1, 2, 3, 4$ or 5) so that $h_i \le h' \le h_{i+1}$. Calculate the eccentricity factors e_t and hue quadrature composition H:

$$e_t = \frac{1}{4}[\cos(\frac{h'\pi}{180} + 2) + 3.8] \tag{2.28}$$

$$H = H_i \frac{100(h' - h_i)/e_i}{(h' - h_i)/e_i + (h_{i+1} - h')/(e_i + 1)} \tag{2.29}$$

Table 2.4 Unique hue data for calculation of hue quadrature (Li et al. 2017).

	Red	yellow	Green	Blue	Red
i	1	2	3	4	5
h_i	20.14	90.00	164.25	237.53	380.14
e_i	0.8	0.7	1.0	1.2	0.8
H_i	0.0	100.0	200.0	300.0	400.0

Step 6: Calculate achromatic response A:

$$A = \left[2R_a + G_a + \frac{B_a}{20} - 0.305\right] N_{bb} \tag{2.30}$$

where

$$N_{bb} = 0.725(\frac{1}{n})^2$$

$$n = \frac{Y_b}{Y_w}$$

Step 7: Calculate the correlate of lightness J:

$$J = 100(\frac{A}{A_w})^{cz} \tag{2.31}$$

where

$$A_w = \left[2R_{aw} + G_{aw} + \frac{B_{aw}}{20} - 0.305\right] N_{bb}$$

$$z = 1.48 + \sqrt{n}$$

Step 8: Calculate the correlate of brightness Q:

$$Q = (\frac{4}{c})\left(\frac{J}{100}\right)^{0.5}(A_W + 4){F_L}^{0.25} \tag{2.32}$$

Step 9: Calculate the correlates of chroma C, colourfulness A, and saturation s:

$$t = \frac{(\frac{50000}{13} N_c N_{cb}) e_t (a^2 + b^2)^{1/2}}{R_a + G_a + (21/20)B_a} \tag{2.33}$$

$$C = t^{0.9}\left(\frac{J}{100}\right)^{0.5}(1.64 - 0.29^n)^{0.73} \tag{2.34}$$

$$M = C{F_L}^{0.25} \tag{2.35}$$

$$s = 100\left(\frac{M}{Q}\right)^{0.5} \tag{2.36}$$

where

$$N_{cb} = N_{bb}$$

There is a reverse model for CIECAM16, mapping the perceived correlates (J, C, h or $Q,\ M, s, H$) to the CIE XYZ tristimulus values under the test illuminant. More details can be found in CIE Colorimetry (CIE 2018).

The acceptance of the CIECAM16 model has made great progress for colour appearance applications, furthermore, a new uniform colour space, CIECAM16-UCS, was developed based on the this model to replace the CIECAM02-UCS space. Three coordinates in the CIECAM16-UCS colour space, J', a', b' are defined as:

$$J' = \frac{1.7J}{1 + 0.007J}$$
$$a' = M' \cos(h) \tag{2.37}$$
$$b' = M' \sin(h)$$

where

$$M' = \ln(1 + 0.0228M)/0.0228$$

The CIECAM16-UCS colour difference between two samples subscripted as 0 and 1 can be calculated as the Euclidean distance between them in the CIECAM16-UCS colour space, and the colour-difference formula can be further improved by applying a power correction, as shown in the following equations:

$$\Delta E' = \sqrt{(J_0' - J_1')^2 + (a_0' - a_1')^2 + (b_0' - b_1')^2} \tag{2.38}$$

$$\Delta E = 1.41(\Delta E')^{0.63} \tag{2.39}$$

2.2 Skin and Skin Colour

Skin is the largest organ and the outermost tissue of the human being (Igarashi et al. 2005). The colour of skin is probably one of the colours that we see most often in our daily lives, and it directly connects with the visual perception of facial attractiveness, health and age (Fink et al. 2006, De Riga et al. 2010, Jones et al. 2016). The study on skin colour has been applied to various multidisciplinary applications. Apart from the colour reproduction of skin in amateur and professional photography (Zeng and Luo 2013), cinematography and printing (Pedersen et al. 2010), these applications include the photographic recording of skin colour for medical diagnosis or treatment response (Choi et al. 2012, Ly et al. 2020), skin-colour based face detection for computer vision applications (Jones and Rehg 2002, Brancati et al. 2017), the identification of skin colour preference in the cosmetic and personal healthcare industries (Caisey et al. 2006, Lee et al. 2019), and the potential manufacture of facial prostheses in 3D colour printing (Xiao et al. 2014). For all these applications, it is of vital importance to understand the structure of the skin and find a reliable technique to objectively quantify the colour of skin.

2.2.1 Skin Components

Skin has a very complex structure that consists of many components, such as cells, fibres, veins, capillaries and nerves (Igarashi et al. 2005). It is mainly composed of three layers: the epidermis, dermis and hypodermis, as shown in Figure 2.12.

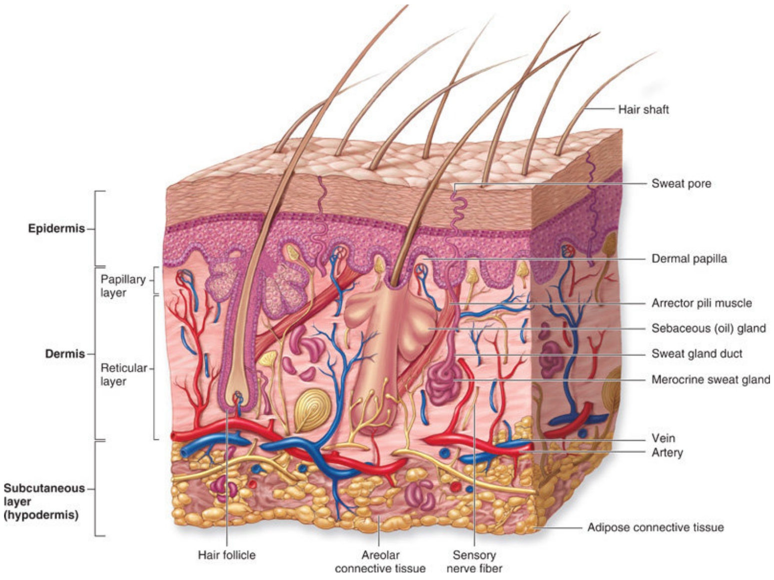

Figure 2.12 The cross-sectional schematic diagram of skin (©The McGraw-Hill Companies, Inc.).

There are two main pigments that determine the skin colour: melanin and haemoglobin (Angelopoulou 2001). Melanin is especially important for contributing differences in skin tones. It is produced in the cells called melanocytes within the skin epidermis (Figure 2.13) and its function is to protect the body by absorbing or scattering ultraviolet radiation before it damages skin cells. People have different skin colours principally because there are different amounts of melanin produced by the melanocytes. Haemoglobin is a red coloured pigment found in blood vessels and it will make the skin appear redder when blood vessels are closer to the surface of the skin. In addition, an orange and yellow pigment in the skin called carotene also helps to determine the colour of the skin. Excess amounts of carotene will result in accumulation in tissues and lead to yellowish skin colour appearance (Ogura et al. 2011).

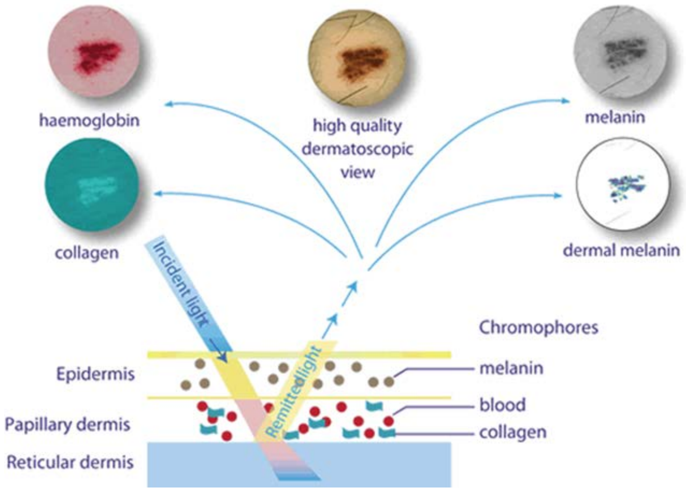

Figure 2.13 The schematic diagram of skin chromophores.

Skin pigmentation is usually the result of individual genetics, geography, and the ultraviolet radiation from the sun (Richards et al. 2003). Human skin exhibits great colour variations from the darkest brown to the lightest white due to the existing pigmentations within the skin. Naik et al. (2022) reviewed the previous research work on assessing skin colour variations among different populations and reported that the ethnic skin colour variations are remarkable in skin structure and functions as well as difference in dermatological disease patterns.

2.2.2 Facial Skin Colour

It is well known that the sebum secretion over the face is different, e.g., the nose is the region to have more sebum secreted on the face, followed by the forehead and chin, compared to other regions such as the cheeks (Igarashi 2005). Similarly, the colours of skin on a human face vary from different regions. It is acknowledged that there is more redness on cheeks, dullness around eyes and suntan for forehead (Yoshikawa 2009). These colours are perceived, observed and evaluated comprehensively as facial skin colour. Figure 2.14 illustrates the interpreted facial skin colour in specific regions.

It was reported that facial redness increases the perception of healthy and attractive colour appearance (Stephen et al. 2009, Thorstenson et al. 2017). Skin colour homogeneity or skin colour heterogeneity, driven by the distributions of skin chromophores, is positively associated with the perception of age, health and attractiveness on the human face (Fink et al. 2006, 2012). Additionally, different skin colouration in the face can be used to judge the physical status of a person as healthy or unhealthy, particularly in the periorbital, cheek, and forehead areas (Jones et al. 2016).

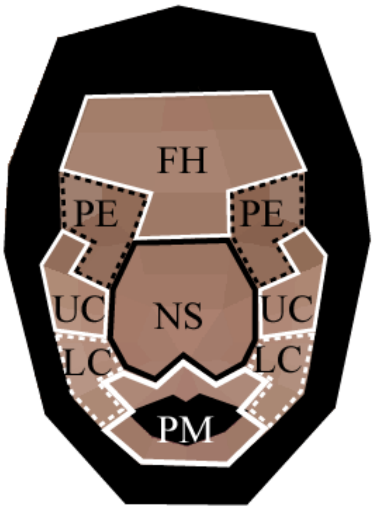

Figure 2.14 The interpreted facial skin colour in specific regions: forehead (FH), periphery of eyes (PE), upper cheek (UC), lower cheek (LC), nose (NS), and periphery of mouth (PM) (Yoshikawa 2009).

2.2.3 Skin Colour Measurement

The measurement of skin colour and its appearance have been investigated in previous studies (Clays et al. 2000, Xiao et al. 2012, Wang et al. 2018). Based on CIE colorimetry, different types of colour measurement instruments were developed and widely used for quantifying object colours, such as a colorimeter, spectrophotometer and spectroradiometer. For measuring human skin colour, the methods can be generally divided into two types: those based on contact measurements and those based on non-contact measurements. Currently, spectrophotometers and tele-spectroradiometers are the two main types of instruments that are most widely used for measuring skin colour. In addition to conventional spectrophotometers and tele-spectroradiometers, it has been widespread to use digital cameras that characterise surface colour and visual texture with the development of digital imaging systems.

2.2.3.1 Spectrophotometer Measurement

A spectrophotometer is a contact-measurement instrument, measuring the colour of a non-self-luminous object by contacting its surface in a selected area. It has an internal light source, usually a tungsten-halogen light source or a xenon flash lamp (Hunt and Pointer 2011), to illuminate the sample so that the amount of light reflected from the surface of the sample can be measured at different wavelengths of the visible spectrum. Typically, the range of wavelengths measured using a spectrophotometer is from 400 nm to 700 nm with intervals of 10 nm. Since a spectrophotometer measures the reflectance factor, a calibration procedure including white and zero calibration is required so that the intensity of light at each group of wavelengths can be scaled to a range of human perception from 0 to 100, where zero is completely dark and 100 is perfect white.

Table 2.5 Studies on skin colour measurement using spectrophotometers.

Authors	Spectrophotometer	Human Population	Body Location
Xiao et al. 2012	Konica Minolta CM-2600d (di:8°, 3 mm)	Chinese	Face, hand, arm
Del Bino and Bernerd, 2013	Datacolour Check (di:8°, 8 mm)	Caucasian, Hispanic, African, Asian.	Breast
Matias et al. 2015	Mexameter MX-18	Fitzpatrick skin type II and III	Back
Wang et al. 2017	Datacolour 600 (de:8°, 8 mm); X-Rite SpectroEye (45°:0°, 4.5 mm)	Chinese, Caucasian, Africans, Sri Lankans	Face, hand, arm
Wang et al. 2018	Konica Minolta CM-700d (di:8°, 3 mm / 8 mm)	Chinese, Caucasian, South Asian, African	Face, neck, hand
Melgosa et al. 2018	Konica Minolta CM-700d (d:8°, 8 mm), CM2600d	Caucasians, Orientals	Face
He et al. 2020	Konica Minolta CM-2600d (di:8°, 3 mm)	Indonesian, Chinese, Caucasian, Mexican, African	Face
Amano et al. 2020	Konica Minolta CM-700d (di:8°, 8 mm),	Not restricted	Arm
Jiang et al. 2022	Konica Minolta CM-2600d (di:8° / de:8°, 8 mm)	Chinese	Face, neck, hand

According to the measuring geometry, there are three main types of spectrophotometer: 0°:45° (or 45°:0°), sphere and multi-angle spectrophotometers. For sphere spectrophotometers, there are two types of measurement modes: specular component included (SCI) and specular component excluded (SCE). A spectrophotometer can provide different sizes of measurement apertures, often denoted small, middle and large aperture size. A suitable spectrophotometer with an appropriate measurement mode for a specific application depends on the sample material, desired functionality and portability.

For measuring skin colour, spectrophotometers are widely used to measure the spectral reflectance of human skin within the visible spectrum. CIE XYZ tristimulus values or CIELAB values can be derived from CIE standard illuminants and CIE standard colorimetric observers. Table 2.5 summarises recent studies on skin colour measurement using spectrophotometers. Generally, spectrophotometers have high accuracy and consistency on measuring surface colours, and they provide different settings for various purposes, giving reliable results of spectral reflectance, CIE colorimetric data and colour-difference values. However, there are some limitations for spectrophotometer measurement, e.g., the measurement aperture size is restricted, wet and liquid samples cannot be measured using a spectrophotometer since it is a contact-measurement device.

2.2.3.2 Spectroradiometer Measurement

A spectroradiometer is a type of non-contact measurement instrument, measuring the amount of radiation of a self-luminous object such as a television and a computer display, or an object illuminated by a light source. It must be borne in mind that the measurement geometry of the light from self-luminous colours may affect the results (Hunt and Pointer 2011). Compare to a spectrophotometer, there is no fixed illumination and viewing geometry integrated in a spectroradiometer. For a non-self-luminous object, an external light source has to be provided to illuminate the object so that the reflected light can be measured using the spectroradiometer. In such cases, it is highly required to have a stable and uniform illumination for obtaining accurate and repeatable measurement results. One of the advantages of spectroradiometer measurement is that the measured results better correspond to the actual viewing conditions.

In addition, a light source can be measured using a spectroradiometer based on a stable white reflecting surface (reference white) with known spectral power distribution. When measuring the absolute radiant power by using a spectroradiometer, a calibration must be performed before measurement, which is usually offered by the instrument manufacturer as part of the instrument package. Furthermore, colour measurement instruments are always evaluated for uncertainty, repeatability and accuracy (Berns 2019), and the results are usually reported in a statement for users.

Spectroradiometers are also utilised for skin colour measurement. Regarding the variability of skin colour measurement between a spectrophotometer and a spectroradiometer, Wang et al. (2017) reported that the spectral reflectance measured using a spectroradiometer had a similar shape to that of a de:8° spectrophotometer measurement which presented a slightly lower amplitude. The reflectance factor achieved from the 45°:0° spectrophotometer is obviously smaller than that from the de:8° device in the long wavelength range greater than 580 nm, although both instruments are contact-measurement instruments. In addition, Wang et al. (2018) investigated the effect of different measurement parameters on skin colour measurement of the forehead and cheekbones, e.g., different measurement aperture sizes and different pressure for the spectrophotometer, and different measurement distances for the spectroradiometer.

2.2.3.3 Camera Measurement

For non-contact measurement instruments, a high-quality digital camera could be one of the options, extracting colour data from the captured images for quantitative analysis. Since colour images collected from a digital camera are in RGB colour space which is dependent on the device used, known as device-dependent parameters, and the colour possibly varies among different cameras. A colour characterisation procedure should be conducted so that the relationship between the RGB signals generated by the digital camera and the corresponding CIE colorimetric values can be quantified. Usually, a colour characterisation model is determined for the camera to transform RGB values of digital images to CIE colorimetric values. The process of camera colour characterisation will be introduced in Section 2.3.

A digital imaging system consisting of a standardized digital camera and a controlled, stable lighting environment has been widely used for skin colour measurement, especially considering that spectrophotometers and spectroradiometers are not suitable for those applications which need to measure a wide range of skin area because of their limited apertures/angles. An example is the DigiEye non-contact colour measurement and imaging system, developed by VeriVide Ltd, as shown in Figure 2.15. It consists of a Nikon D7000 SLR (digital single-lens reflex) camera controlled by the DigiEye software and a large viewing cabinet providing consistent and uniform daylight environment. Xiao et al. (2016b) used this device to capture the colour images of human faces and reconstructed spectral reflectance of skin from camera RGB images. In addition, various digital imaging systems were developed to study facial colour distributions, skin colour heterogeneity, dermatology diagnosis (Kikuchi et al. 2015 and 2020, Ly et al. 2020) .

Figure 2.15 DigiEye colour imaging equipment with a large cabinet.

2.2.4 Skin Colour Database

In order to investigate the uncertainty in skin colour measurement and recommend protocols for good measurement practice, CIE Technical Committee *CIE 1-92: Skin Colour Database* was established to encourage the collection of skin images and skin colours covering different ethnicities, gender, age and body locations. Its aim is to understand the characteristics of skin colours and develop a publicly accessible database of skin reflectance data. With the increasing demands of multi-disciplinary applications of human skin colour, various skin colour databases including spectra data and CIE LAB values were developed to provide the reference for evaluating skin colour reproduction.

2.2.4.1 SOCS

In 2003, the ISO published an international standard: *Graphic technology - Standard object colour spectra (SOCS)* database for evaluating the colour reproduction of image input devices (ISO 2003). It includes 8213 human skin colours from six groups: SHISEIDO, KAO, OOKA, KAWASAKI, OULU and SUN, covering a relatively large number of skin colours for different genders, ethnicities and body locations (forehead, cheek, neck and arm). Table 2.6 lists the information of instrument types, human subjects and measured body locations of these six groups of skin colours. It can be seen that most skin colour data were collected from Japanese and Caucasian participants, and the number of human subjects from other ethnic groups is limited. Based on these skin colour data collected, ISO/TR16066 recommends six typical skin colour groups (ISO/TR 2003):

- Bare North Asian skin,
- Foundation-applied North Asian skin,
- Bare South Asian skin,
- Foundation-applied South Asian skin,
- Bare Caucasian skin
- Bare Negroid skin.

The SOCS database did not report the details of the instrument used, and different types of colour measurement instruments with different measurement settings used made it problematic to compare between different datasets.

Table 2.6 The six groups of skin colour databases included in SOCS (Xiao 2013).

	Instrument Types	Human subjects	Body locations
SHISEIDO	Contact (d:0° SCE)	Asian females (most Japanese)	Forehead, cheek, neck
KAO	Contact (d:0° SCE)	Japanese Females	Forehead, cheek, arm, neck
OOKA	Non-contact & contact	Japanese (most males)	forehead, cheek
KAWASAKI	Non-contact & Contact	Most Japanese males	Forehead, cheek
OULU	Contact (d:8° SCE)	Most Caucasian, Negroid, Asian	Forehead, cheek
SUN	Contact (d:8° SCE)	Caucasian, Negroid and other ethnics	Forehead, cheek, neck, hand

2.2.4.2 L’Oréal

Colour measurements on human skin were extensively conducted by the L’Oréal Ltd. for various research purposes. In 2007, more than 1000 women including Caucasian and half-caste (France, United States, Mexico, and Brazil), Asian (Japan, Korea, China, and Thailand) and African descent were involved in a study where a Photo Research PR-650 spectroradiometer was used to measure the bare skin colours at the forehead, cheekbone and forearm in the Chromasphere device which was developed by the L'Oréal Ltd. to provide a constant diffusing lighting environment (Rigal et al. 2007). In 2010, colour images of 385 female faces (121 African-American, 80 Caucasian, 120 Chinese and 64 Mexican, aged from 18 to 87) were captured, and skin colour data were derived from the images by performing colour characterisation using a Macbeth ColorChecker chart (Rigal et al. 2010). The effect of age on skin colour and colour heterogeneity in the four ethnic groups were investigated based on CIELAB values. Moreover, Colomb et al. (2018) conducted skin colour measurements on cheeks of 1204 Indian females aged from 18 to 84 years, using a Photo Research PR-650 spectroradiometer to obtain the CIELAB values.

2.2.4.3 Shiseido

Facial skin colour measurements were extensively conducted by Shiseido Ltd. during the years of 1991-2015, with 3181 healthy Japanese women aged from 20 to 59 years involved (Kikuchi et al. 2018). The bare skin colour was measured at the area under the cheek by using three colour measurement instruments, and the spectral reflectance data of the facial skin were collected in the wavelength range of 400 nm to 700 nm at intervals of 10 nm. More detail information can be found in Table 2.7 for when the colour measurements were taken, the number of human subjects, the measurement instrument and settings.

Based on the collected skin colour database, Kikuchi et al. (2018) reported long-term skin colour changes in Japanese women's face and investigated the factors relevant to skin pigmentations that affect the skin colour changes.

Table 2.7 Information about Shiseido's facial skin colour measurements.

Years	No. of subjects	Instrument
1991-1992	794	Konica Minolta CM-1000RHs (de:8°, 10 mm)
1999-2002	847	Konica Minolta CM-1000RHs (de:8°, 10 mm)
2004-2006	350	Konica Minolta CM-2600d (di:8°, 8 mm)
2013-2015	644	Konica Minolta CM-2600d (di:8°, 8 mm)
	546	Konica Minolta CM-700d (di:8°, 8 mm)

2.2.4.4 Xiao et al.

Xiao et al. (2017) developed a new skin colour database by measuring skin colours of four body areas (forehead, cheek, back of hand, inner arm) of 960 individuals from four different ethnic groups: Caucasian, Chinese, Kurdish, Thai. This database includes 3860 skin colour data in terms of CIE XYZ tristimulus values under CIE illuminant D65 and CIE 2° standard colorimetric observer, which was used to investigate the variations in different ethnic skin colours. Table 2.8 gives relevant information about the collection of this skin colour database.

Table 2.8 Information about the collection of the skin colour database developed by Xiao et al.

	Number	Site	Instrument
Caucasian	187 (102 F, 85 M)	UK	Konica Minolta CM-2600d (di:8°, 3 mm)
Chinese	202 (65 F, 137 M)	China	
Kurdish	145 (74 F, 72 M)	Iraq	
Thai	426 (283 F, 143 M)	Thailand	X-Rite SP62 (di:8°, 4 mm)

Additionally, there is a skin reflectance database developed by Xiao et al. (2016b) which consists of 4392 colour data measured using a CM-2600d spectrophotometer on nine body locations of 482 subjects from three ethnic groups: Caucasian, Chinese and Kurdish. This database was used to improve the method for skin reflectance reconstruction from camera RGB images.

Another similar skin colour database was reported by Wang (2017) in her PhD dissertation, named the Leeds-Liverpool skin colour (LLSC) database. It was collected from 188 human participants from four ethnic groups: Caucasian, Oriental, South Asian and African. Three colour measurement instruments, a Konica Minolta CM-700d spectrophotometer, a Photo Research PR650 spectroradiometer and a VeriVide DigiEye digital imaging device, were used to measure skin colour data of each subject at 10 different body locations on face, neck, hand and arm. Over 10000 spectral data and 900 2D images of skin colour were collected, and the development of this skin colour database can be summarised as the following:

- 188 subjects including 86 Oriental, 79 Caucasian, 13 South-Asian and 10 African,

- 10 body locations measured by using a Konica Minolta CM-700d spectrophotometer,
- 5 body locations measured by using a PhotoResearch PR650 spectroradiometer,
- Each body location measured 3 times,
- 5 colour images captured for each subject.

2.2.5 Skin Colour Chart

In addition to colour measurement instruments described in Section 2.2.3, a skin colour chart could be used as a tool for skin colour reproduction, skin colour evaluation, and as a reference chart for skin colour image capture. It is usually developed based on massive data of colour measurements on actual human skin, either printed or painted colours. The presence of a skin colour chart effectively improves the standardisation of visual colour assessments.

2.2.5.1 Pantone SkinTone Guide

The Pantone SkinTone Guide, Figure 2.16 (left), was developed by scientifically measuring thousands of actual skin tones of human participants in a diverse range of ethnicities and age groups by using X-Rite spectrophotometers (Pantone 2012). It includes 110 skin tones numbered from 1Y01 SP (the lightest yellow tone) to 4R15 SP (the reddest tone), as shown in Figure 2.16 (right). Each Pantone SkinTone number is composed of a four-digit alpha numeric number where the first two indicate the hue or undertone of the skin and the second two represent the lightness and darkness of the skin.

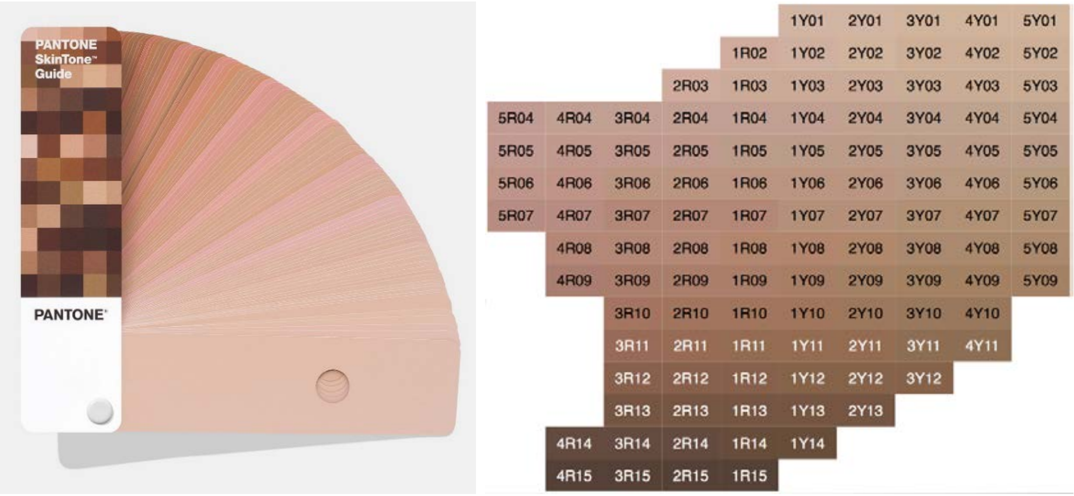

					1Y01	2Y01	3Y01	4Y01	5Y01
				1R02	1Y02	2Y02	3Y02	4Y02	5Y02
			2R03	1R03	1Y03	2Y03	3Y03	4Y03	5Y03
5R04	4R04	3R04	2R04	1R04	1Y04	2Y04	3Y04	4Y04	5Y04
5R05	4R05	3R05	2R05	1R05	1Y05	2Y05	3Y05	4Y05	5Y05
5R06	4R06	3R06	2R06	1R06	1Y06	2Y06	3Y06	4Y06	5Y06
5R07	4R07	3R07	2R07	1R07	1Y07	2Y07	3Y07	4Y07	5Y07
	4R08	3R08	2R08	1R08	1Y08	2Y08	3Y08	4Y08	5Y08
	4R09	3R09	2R09	1R09	1Y09	2Y09	3Y09	4Y09	5Y09
		3R10	2R10	1R10	1Y10	2Y10	3Y10	4Y10	
		3R11	2R11	1R11	1Y11	2Y11	3Y11	4Y11	
		3R12	2R12	1R12	1Y12	2Y12	3Y12		
		3R13	2R13	1R13	1Y13	2Y13			
	4R14	3R14	2R14	1R14	1Y14				
	4R15	3R15	2R15	1R15					

Figure 2.16 Pantone SkinTone Guide (left) and the 100 skin tones included (right).

As shown in Figure 2.16 (left), the Pantone SkinTone Guide is composed of individual large-size (1.75” x 7”) swatch with a central hole (10 mm diameter) for easy colour communication and evaluation, recommended to match skin colours under simulated D65 illuminations. Its application could be in different fields, such as beauty, fashion, photography, medical, printing and graphic design, etc.

2.2.5.2 L’Oréal Skin Colour Chart

De Rigal et al. (2007) introduced a new Skin Colour Chart (as shown in Figure 2.17) developed by L’Oréal Ltd., which was designed to standardise the visual evaluation related to skin colours. Fifty-five skin colours were generated in the L’Oréal Skin Colour Chart, based on the skin colour database collected from more than 1000 women from different ethnic groups. It is presented as a sort of fan of 52 colour swatches, and each has a hole with a diameter of 3 cm for evaluating a defined skin area. De Rigal et al. reported that this chart represents true skin colour without metamerism and covers almost all skin colours encountered around the world.

Figure 2.17 L’Oréal Skin Colour Chart.

2.2.5.3 Spectromatch Silicon skin colour chart

The silicon skin colour chart was developed by Spectromatch Ltd., consisting of 90 individual skin colour samples made with silicon (Figure 2.18). It has a large skin colour gamut covering various skin tones from different ethnic groups, and its aims is to provide an accurate reference chart for soft tissue prostheses applications. The spectral reflectance data of the 90 silicon skin colour samples were reported in the study published by Xiao et al. (2016), and this chart was used to calibrate a digital camera for the purpose of reconstructing skin reflectance from the captured colour images.

Figure 2.18 Silicon skin colour chart developed by Spectromatch Ltd.

2.3 Colorimetry with Digital Cameras

As described in Section 2.2.3.3, a digital camera can be used as a non-contact instrument to carry out colorimetric measurements on objects, especially those with complicated shapes or patterns that are tedious to be measured by using a spectrophotometer or a tele-spectroradiometer. Considering that the colour images captured using a digital camera are in a device-independent RGB colour space, this section will review the principles and methods for CIE colorimetric measures with digital cameras.

2.3.1 Overview

A digital camera is an optical instrument that records still or moving images, based on an image sensor such as a CCD (Charged Coupled Device) or a CMOS (Complementary Metal–Oxide–Semiconductor) detector converting images into pixels. The greater the number of pixels, the higher the resolution and quality of the created image. Most cameras can capture two-dimensional (2D) images in width and height, while some more advanced models can capture three-dimensional (3D) images in width, height and depth. In other words, 2D cameras lack geometrical information and provide solely flat images, while 3D cameras are stereoscopic cameras that add an illusion of depth in images to replicate three dimensions. For a stereoscopic imaging system, multiple cameras are used and placed at different angles to capture multiple images simultaneously, or a single moving camera is used to capture photos at different times.

A digital single-lens reflex camera (digital SLR or DSLR) is a type of digital camera that combines the optics and the mechanisms of a single-lens reflex camera with a digital imaging sensor. It has been extensively used in photogrammetric applications with good image quality. Figure 2.19 shows the diagram of a DSLR camera, listing the components of a DSLR camera.

With a DSLR camera, the light travels through the lens and then to a mirror that alternates to strike an image sensor when the shutter release button is pressed. The signal output by the image sensor is processed within the camera to create image data which can be stored on a memory card. The characteristics of an image sensor can be quantified as camera spectral sensitivities, which are three functions of wavelength describing the relative efficiency of light detection for colour filters and image sensors (Jiang et al. 2013). The camera spectral sensitivity functions can be used to map the spectral information in a scene to the RGB response values recorded by a digital colour camera. This process of camera image capture is similar to the action of the human colour vision system that is characterised by a group of colour matching functions sensitive to three types of photoreceptors in the retina (see Section 2.1.1).

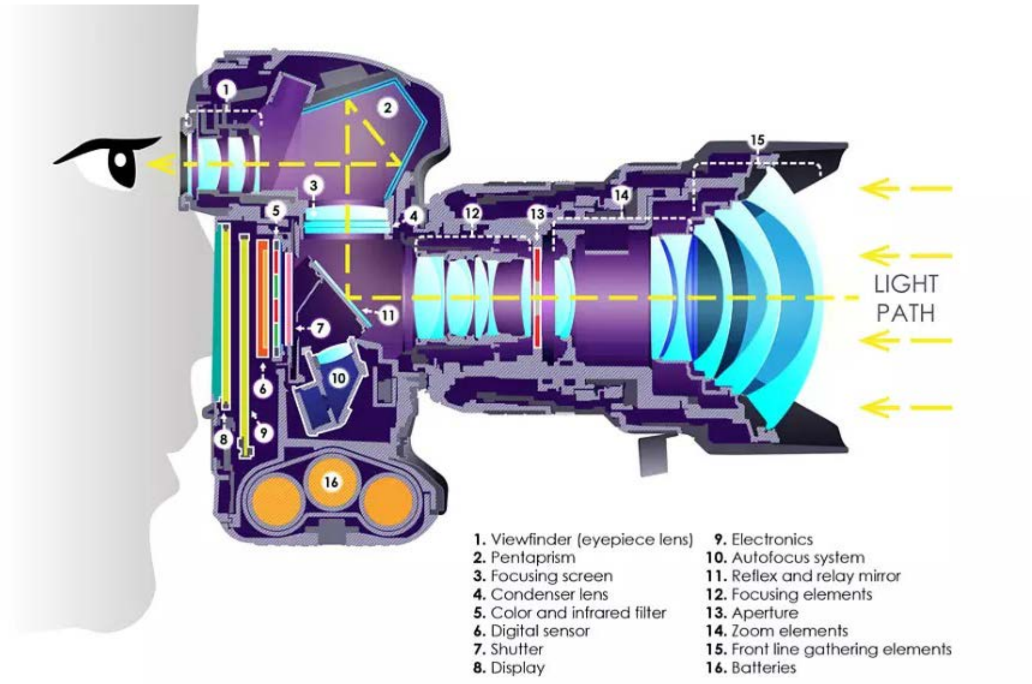

Figure 2.19 Diagram of a DSLR camera.

Image downloaded from https://www.ephotozine.com/article/this-cutaway-diagram-shows-the-inside-of-a-dslr-30546.

2.3.1.1 Camera Settings

For the acquisition of high-quality digital colour images, it is essential to understand camera settings before taking image captures, because different camera settings affect the colour information of the captured image. Appropriate parameters should be selected and used for different lighting conditions. The amount of light that reaches the image sensor inside the camera can be controlled by manipulating three variables: aperture, shutter speed and ISO speed, commonly known as the exposure triangle.

The aperture is one of the most important settings in a digital camera. It is the size of the opening "window" of the camera lens that controls the amount of light that reaches the image sensor. The wider the opening "window" is, the more light the camera sensor will capture. The aperture of a digital camera can also be expressed as a number, known as f-number, or f-stop, such as f/16, f/11, f/8, f/5.6, f/4, f/2.8, f/2, f/1.4. Small numbers in f-stop represent large apertures, and large numbers represent small apertures, as shown in Figure 2.20.

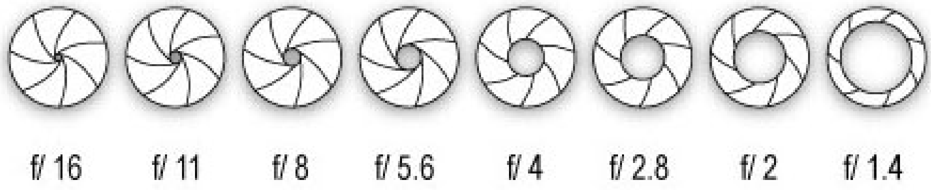

Figure 2.20 Diagram of different aperture sizes.

The aperture size of a digital camera affects the brightness of the captured image. Typically, a larger aperture is preferred in darker environments and a smaller aperture is desired in high and bright lighting conditions. However, it should be noted that the aperture size always works together with the shutter speed to control how much light passes through the lens to the sensor. In addition, the aperture size of the camera lens also has an interesting effect on how the light is focused for a scene. If an image is taken with a larger aperture (such as f/1.4), the background will blur while the subject stays in focus, known as a shallow depth of field. On the contrary, a small aperture (such as f/16) will give a deeper depth of field, which means a large area of the image will be in focus.

Shutter speed is another fundamental setting of a camera that is also related to the main camera exposure. It represents the length of time the camera shutter stays open and captures light, and it is measured in seconds, such as 2’’, 1’’, 1/2, 1/4, 1/8, 1/15, 1/30, 1/60, 1/125, 1/250, 1/500, 1/1000, 1/2000.

The smaller the shutter speed number, the shorter the exposure time. In the case of using a slower shutter speed (such as 1/2 second), it allows the camera to gather more light, while a faster shutter speed (such as 1/2000 second) allows to freeze the action and avoid blurry photos. The aperture and shutter speed of a camera work together to control the amount of light gets to the sensor. For example, the camera will use a faster shutter speed with a larger aperture (such as f/1.4), while with a smaller aperture (such as f/16) the camera will use a slower shutter speed.

The ISO speed is the last parameter in the camera exposure triangle. It is used to brighten or darken an image by adjusting the sensitivity of the camera sensor. It gives an extra option to manipulate the camera exposure in addition to aperture and shutter speed. Each camera has a different range of ISO values, and a common set could be ISO 100, ISO 200, ISO 400, ISO 800, ISO 1600, ISO 3200, ISO 6400. The higher the ISO value, the more sensitive the sensor is to light. If a picture is taken in the same lighting conditions, increasing the ISO value will produce increasingly brighter images. However, one needs to be careful using a high ISO value during image capture, since it will be detrimental to the quality of the image, adding more image noise and making it too grainy.

The three variables in the exposure triangle, aperture, shutter speed and ISO speed, must always be in balance to take the right exposure and acquire good-quality colour images. For example, ISO 100 is a lower sensitivity, so it requires more light to create a good exposure. In this case, it is indicated that the camera will use a larger aperture or a slower shutter speed to gather more light enter to the camera.

The White Balance (WB) setting of a digital camera is a process of adjusting and balancing RGB colours with black and white in an image. It is one way to let the camera know what type of light that the scene is photographed under. Most DSLR cameras have three settings for white balance; automatic, preset and custom. By selecting the automatic white balance, the camera will use its built-in light meter to determine what type of lighting is illuminating the scene and it will attempt to estimate the colour of the illumination and correct for it. However, it doesn’t always get it right and so, if possible, it is a better option to set the WB manually. Preset white balance is where the camera uses a fixed (preset) estimation of the illumination, such as tungsten, fluorescent, daylight, and cloudy. This is a quick and simple solution to take an image with good white balance, but it is not always perfect.

Custom white balance is a manual mode that allows users to define it by capturing a grey reference card under the same lighting condition. For some advanced cameras, the white balance can be adjusted by manually inputting the value of colour temperature (in Kelvin unit). The Custom mode of white balance is preferred if colour images are being captured in a stable and well-controlled lighting environment, such as a standard viewing cabinet.

2.3.1.2 Image File Formats

There are three most common image file formats in digital camera imaging: JPEG (Joint Photographic Experts Group), TIFF (Tagged Image File Format), and different RAW files. JPEG is probably the best known out of all the image files, recommended as a ISO/IEC 10918-1 standard in 1994 (ISO/IEC 1994). It is a kind of image format with lossy compression, consequently, JPEG has much smaller storage size than TIFF and RAW image formats. Although this image format loses some image details and stores a lower-quality image, JPEG is typically set as the default output for most cameras since the image quality is sufficient for digital devices. The disadvantage of JPEGs is that less opportunity is provided for image manipulation in photo-editing software.

TIFF is a lossless-compression image format that doesn’t lose information about a photo’s data, so the file size of TIFF images is larger than JPEG images and a larger storage space is usually required. TIFF files are recommended for graphic printing to keep digital photos as high-resolution as possible. A camera RAW image file contains the uncompressed and unprocessed or minimally processed data captured by the image sensor of a digital camera. It is designed to capture the radiometric characteristics of the scene and preserve all of the data captured, resulting in large file sizes and lossless image quality. Many researchers and professional photographers prefer to record in RAW file format, because it provides maximum flexibility and full control of post processing, such as linearization, white balance, gamma correction, etc.

The RAW image formats from different camera manufacturers are not the same, e.g., Canon cameras saved RAW images in the CR2 or CRW format, Nikon cameras used NEF or NRW format, Sony cameras used SRF or ARW format. Most digital cameras enable to choose between JPEG, TIFF, RAW image formats, and it allows to capture JPEG and RAW images simultaneously.

2.3.2 Practical Considerations in Digital Imaging Systems

2.3.2.1 Illumination

The illumination in a digital imaging system is a very important factor for objectively colour measurement. A stable and uniform lighting environment is desired so that the target object can be illuminated evenly and captured in a quantitative and repeatable way, avoiding highlights and shadows. A perfect uniform illumination is seldom achieved in practice, but variation should be reduced as much as possible. In most cases, a viewing cabinet uses a number of fluorescent lamps at a suitable distance to provide reasonably even diffuse illumination. Alternatively, two directional light sources at 45° to the subject plane could be used to achieve near-uniform illumination (Hunt and Pointer 2011).

In addition, the illumination used to light the object should be the same as that used to calculate the colorimetric values in the characterisation process, because there are issues of metamerism caused by different illuminations in practice. A variety of spectral power distributions may be encountered for matching CIE specifications such as CIE standard illuminant D65. Therefore, it is essential to derive the spectral power distribution of the illumination used in the digital imaging system to calculate the corresponding colorimetric values.

2.3.2.2 Calibration and Reference Colour Chart

Depend on the specific lighting environment, the digital imaging system should be calibrated before taking image captures, which is a process of determining specific camera parameters, such as the three variables of the exposure triangle, the white balance and the focus length, to set the camera to a known state. More information related to camera settings can be found in Section 2.3.1.1. Appropriate parameters should be decided and used for consistent and good-quality image captures.

Typically, a reference colour chart including grey scales is used for creating camera profiles, correcting white balance and performing colour correction. Currently, the two widely used colour charts for camera colour calibration and characterisation are: ColorChecker Classic chart and ColorChecker Digital SG chart, as shown in Figure 2.21. The ColorChecker Classic chart is composed of 24 colour patches including 6 greyscale patches and other nature object colours such as human skin, blue sky and foliage. It is designed for use as a colour calibration tool in both traditional and digital photography.

Figure 2.21 The X-Rite ColorChecker Classic chart (left) and ColorChecker Digital SG chart (right).

The ColorChecker Digital SG chart is composed of 140 colour patches, including the 24 patches from the ColorChecker Classic chart, 17 grey scales, 14 unique skin tone colours and other nature object colours. There was a ColorChecker DC chart designed for digital camera profiling, and it has been replaced by the ColorChecker Digital SG chart. Compared to the original classic chart, the SG chart covers a larger colour gamut, and it is used as a pro-level colour calibration tool for a variety of colour-management workflows. Additionally, a wider variety of skin-tone reference colours are included in this chart to deliver further accuracy and consistency of skin colour reproduction. Based on the selected colour chart, it becomes simple and efficient to set perfect exposures and accurate white balance.

The implementation of calibration is a prerequisite for digital imaging systems, aiming to ensure the reproduction of reliable and meaningful data at all time. The colour characterisation results are only valid under the same conditions of calibration, i.e., the specific lighting environment and camera settings.

2.3.3 Colour Characterisation Method

Colour characterisation refers the quantification of a relationship between device coordinates and a device-independent colour space. The methods for camera colour characterisation could be divided into two main types: spectral sensitivity based and colour target based (Hong et al. 2000). For the former characterisation method, the spectral sensitivity of the camera sensor needs to be measured using a monochromator in the Lab, which is both time and cost-consuming. For the later characterisation method, a reference target containing a series of colour samples with known spectral reflectance or CIE XYZ tristimulus values is captured using the digital camera so that the relationship between camera RGB values and the corresponding CIE colorimetric coordinates can be characterised. Such a target used for camera colour characterisation could be the ColorChecker chart introduced in Section 2.3.2.2.

The colour target based method is much simpler and easier to be applied in comparison to the spectral sensitivity based method which requires expensive specialized apparatus. Therefore, most studies (including this study) used a reference colour chart for performing camera colour characterisation with different algorithms, such as linear regression, polynomial regressions, neural networks and lookup tables.

2.3.3.1 Linear Regression

A simple linear colour transformation between camera RGB signals and CIE XYZ tristimulus values can be expressed as:

$$\begin{bmatrix} X \\ Y \\ Z \end{bmatrix} = M \times \begin{bmatrix} R \\ G \\ B \end{bmatrix} \tag{2.40}$$

where M is a 3×3 transformation matrix converting camera RGB values to corresponding CIE XYZ tristimulus values, and it can be determined using the following equation:

$$M = \begin{bmatrix} X_R \\ Y_R \\ Z_R \end{bmatrix} \times \begin{bmatrix} R_R \\ G_R \\ B_R \end{bmatrix}^{-1} \tag{2.41}$$

where $X_R\, Y_R\, Z_R$ are the CIE XYZ tristimulus values of a number of colour patches in a reference colour chart, and $R_R\, G_R\, B_R$ are the RGB values extracted from the image captured using the digital imaging system.

The advantage of a linear transformation is its invertibility. Theoretically, the transformation relationship between camera RGB values and CIE XYZ values is linear if the digital camera gives perfect-quality colorimetric data. In practice, however, linear transformations are not adequate to characterise the digital camera because of the complexity of camera sensitivity functions. Nonlinear transformations are often used to establish the best fitting for camera colour characterisation (Hong et al. 2001).

2.3.3.2 Polynomial Regressions

One approach to improve the accuracy of camera colour characterisation is to apply polynomial regression to the transformation matrix by adding more terms. In such cases, the transformation between camera RGB values and CIE XYZ values can be expressed as:

$$T = M \times C \tag{2.42}$$

where T indicates a set of CIE XYZ tristimulus values, M is a $3 \times N$ transformation matrix and C denotes RGB matrix with N extended terms. Note that N=3 is the case of linear transformation, as expressed in Equation 2.40.

The polynomial regressions with the least-square fitting method have been extensively studies for camera colour characterisation. Hong et al. (2002) investigated the polynomials with different terms (N = 3, 5, 6, 8 ,9, 11) for colour characterisation transformation from camera RGB values to CIE XYZ values and they addressed that the black “1” and white “RGB” terms were important for achieving more accurate results. Li et al. (2003) compared five polynomial models with the order changing from 1st to 5th (N = 4, 10, 20, 35, 56) for a digital camera colour characterisation, and it was found that a higher order performed better than a lower one among the polynomial models of the 1st-4th order, while the 5th order polynomial performed worse than the 2nd order polynomial. Cheung et al. (2004a) conducted a comparative study on camera colour characterisation using polynomial regressions with different extended terms (N = 3, 4, 5, 10, 20, 35) and the results showed that the best result was given by using the 3rd order polynomial regression (N = 20). Table 2.9 lists the corresponding terms of the polynomial regressions with the 1st, 2nd and 3rd order.

Table 2.9 The corresponding terms of the polynomial regressions with the 1st-3rd order.

Order	Number of terms	Terms
1st	4	$r, g, b, 1$
2nd	10	$r, g, b, r^2, g^2, b^2, rg, rb, gb, 1$
3rd	20	$r, g, b, r^2, g^2, b^2, rg, rb, gb,$ $r^2g, , r^2b, g^2b, rg^2, rb^2, gb^2, r^3, g^3, b^3, 1$

One of the disadvantages of using polynomial regressions is the trade-off between colour predictive accuracy and the overfitting results due to the higher orders. It is possible that independent data with similar RGB values are sometimes mapped to very different CIE XYZ values. Moreover, the data outside the range of the reference colour chart are likely extrapolated in unexpected ways, resulting in large errors in colour predictions (Berns 2019).

Finlayson et al. (2015) proposed a new polynomial-type regression called Root Polynomial, which is to take each term in an order-root polynomial expansion. Table 2.10 gives the corresponding terms of the root-polynomial regressions with the 1st-3rd order, and it can be seen that the number of root-polynomial terms is reduced compared to that of polynomial terms. The results showed that the root-polynomial algorithm performed better than linear regression and offered a significant improvement over polynomial model on camera colour correction.

Table 2.10 The corresponding terms of the root-polynomial regressions with the 1st-3rd order.

Order	Number of terms	Terms
1st	3	r, g, b
2nd	6	$r, g, b, \sqrt{rg}, \sqrt{rb}, \sqrt{gb}$
3rd	13	$r, g, b, \sqrt{rg}, \sqrt{rb}, \sqrt{gb}, \sqrt[3]{r^2g}, \sqrt[3]{r^2b}, \sqrt[3]{b^2g},$ $\sqrt[3]{rg^2}, \sqrt[3]{rb^2},, \sqrt[3]{gb^2}, \sqrt[3]{rgb}, 1$

2.3.3.3 Lookup Tables

Another approach is to create a lookup table consisting of a large number of camera RGB values and corresponding CIE XYZ values of the well-sampled target colour patches in a large colour gamut, which defines the transformation between camera RGB colour space and a CIE colour space at a series of discrete measured coordinates. Interpolation is necessary in lookup tables to map the values for intermediate coordinates. The basic model used in ICC profiles standardized by the *International Colour Consortium* is lookup table, which is commonly used in printer colour characterisation (Hung 1993). A lookup table requires a high number of measurements, and it is suitable for storing and reusing complex colour transformation.

2.3.3.4 Neural Networks

In addition to the above methods, it is also possible to use neural networks to perform colour characterisation transforming from camera RGB to CIE XYZ values. Neural networks are computer models that attempt to imitate some of the functions of the human brain using certain basic structures (Westland 1998). A high-level neural network consists of input, hidden and output layers of interconnected nodes or neurons. Each neuron receives input from the previous layer, computes a weighted sum of these inputs, and produces an output that is some function of the weighted inputs (Hunt and

Pointer 2011). This process is repeated for each layer, allowing the network to learn complex patterns and representations from the input data.

Kang and Anderson (1992) applied the neural network with the Cascade Correlation learning architecture to map device values to CIE colorimetric coordinates. Cheung et al. (2004b) used a multilayer perceptron of artificial neural networks as a universal function approximator to find a map between camera RGB values and XYZ values. The network was trained by finding a set of weights that produce the smallest difference between the actual and target output vectors for a set of samples.

The method of neural networks requires a large number of training data, and it works well for highly nonlinear relationships. It should be noted that neural networks have no relationship to the physics of the imaging devices, they must be trained each time a change is made in any component of the system. In addition, the nonlinear transformation using neural networks is not reversible, and the training process takes much longer time than other methods due to an iterative process of computations.

2.3.4 Accuracy Measures

The accuracy of the camera colour characterisation model developed is typically measured by calculating colour differences between the predicted and measured CIE XYZ values of a number of test colours. In most cases, the test colours are the colour patches in the reference colour chart which is used for the determination of the colour characterisation model. However, it is suggested to separate the training data and testing data so that the validation of the model is more reasonable.

The most widely used colour difference formulae are CIELAB and CIEDE2000, and the averaged colour-difference value is usually used to quantify the predictive accuracy of the colour characterisation model. Moreover, Pointer et al. (2001) addressed that the maximum colour-difference value should be evaluated together with median colour-difference value for adequate investigation.

2.4 Colour Reproduction in 3D Printing

3D printing, also known as additive manufacturing, is an additive process whereby layers of materials are built up to create a three-dimensional (3D) part based on a CAD (computer-aided design) model or a digital 3D model. It is regarded as a revolutionary technology for customised fabrication because of its advantages in saving both time and costs. In recently years, colour 3D printing technology has been developed dramatically and widely applied in various industrial fields such as art and design practice (Walters 2009), dentistry (van Noort 2011), food (Sun et al. 2015), and fashions (Vanderploeg et al. 2017), etc. With the evolution of various 3D imaging techniques, it provides the ability to directly interconnect with advanced manufacturing techniques, allowing customisation with high accuracy and making it highly possible to achieve “What You See Is What You Get” (Xiao et al. 2016a). This section will review the current colour 3D printing technologies, colour characterisation methods of a 3D printer, colour quality evaluation for 3D printed objects, and the application of 3D printing in skin colour reproduction.

2.4.1 Colour 3D Printing Technology

Various 3D printing technologies have been developed with different functions, and they are classified into seven groups according to ASTM standard F2792 (ASTM 2012): the binding jetting, material jetting, powder bed fusion, material extrusion, sheet lamination, directed energy deposition and vat photopolymerization. Chen et al. (2022) reported that the material jetting and vat photopolymerization printers are the most accurate by comparing the printing accuracy of 16 printers that are commonly used in the medical field, which covered five distinct printing technologies and eight different vendors.

Table 2.11 Full colour 3D printing technologies.

Colour Technology	Brand	Technology	Materials
PolyJet	Stratasys	UV-Cured	Resin
ColorJet Printing	3D Systems	Powder-binder	Powder
UV-curable inkjet	Mimaki	UV-Cured	Resin
MultiJet Fusion	Hewlett Packard	Powder-fusion	Powder
Laminated Object Manufacturing (LOM)	Mcor	Paper-binder	Paper

To print a 3D object in full colour spectrum, different technologies have been developed and applied in different 3D printing systems, such as the PolyJey technology based on UV cured light from Stratasys, ColorJet Printing with powder binder from 3D Systems, UV-curable inkjet printing technology from Mimaki, MultiJet Fusion with powder fusion from Hewlett Packard, and LOM from Mcor, more information is given in Table 2.11. Full colour means thousands of colours can be produced by a 3D printer, it is different from the term of multicolour which refers to models made using multiple materials in different colour. Full-colour 3D printers can produce realistic production prototypes.

The Polyjet printing technique, a patented invention of Stratasys Ltd., is an additive manufacturing system that builds parts by jetting photopolymer droplets in CMYK colours from printer heads onto a build tray and solidifying each layer with UV-curable light, as illustrated in Figure 2.22. It is stated that Stratasys CMYK colours can be matched to 1970 printable PANTONE Colours, Solid Coated and SkinTones™. The J-series 3D colour printers developed by Stratasys Ltd. are widely used in applications of dental, anatomy, fabric and fashion. Models can be printed with a glossy or matte surface finish. Liu et al (2019) utilised a Stratasys J750 3D printer to build a 3D colour reproduction system for dental prostheses.

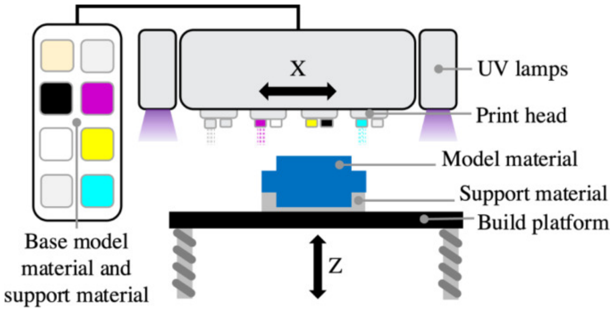

Figure 2.22 Schematic diagram of PolyJet 3D printing (Wei et al. 2022).

The ProJet ColorJet Printing (CJP) technology developed by 3D Systems Ltd. is an additive manufacturing technology that creates parts by spreading powder polymer in thin layers over the build platform with a levelling roller, and colour binders in CMY colours (cyan, magenta and yellow) are selectively mixed and jetted from inkjet print heads after each layer is spread (see Figure 2.23). The Z Corporation developed such powder-binder 3D printing technology and its Zprinters had been used for printing 3D objects in full colour. The company was acquired by 3D Systems Ltd. in 2012.

The colour 3D printing technology from Mimaki is based on UV light which was originally developed for its 2D flatbed printers. It uses white or clear liquid resin as the base material and jets CMYK colours to coat the base with soluble support material on a bed layer by layer (Figure 2.24). Each layer is cured by the UV light and a roller flattens the material layer, the process repeats until 3D prints are produced and finished in colour.

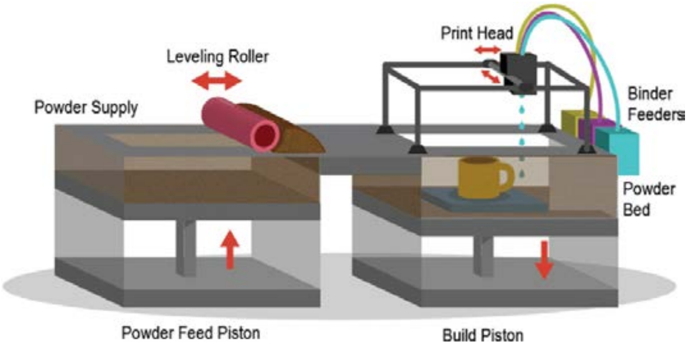

Figure 2.23 Schematic diagram of ProJet CJP technology (Espera et al. 2019).

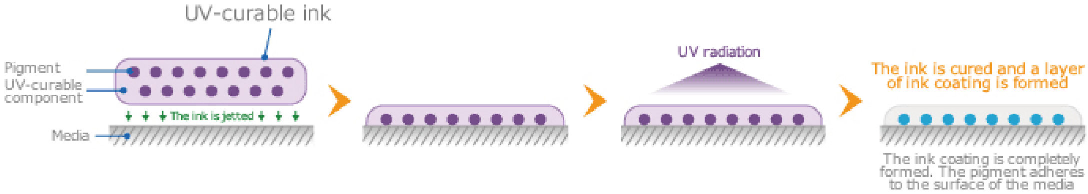

Figure 2.24 Mechanism of UV-curable inkjet technology.

Image downloaded from https://mimaki.com/supply/ink/uv-curable.html

For the printing technology of MultiJet Fusion developed by Hewlett Packard in 2016, it creates parts by depositing fusing and detailing agents in a bed of powder material, then fusing them into a solid layer. This process repeats layer by layer with more powder distributed on top of the bed.

The paper-based colour 3D printing technology from Mcor is to deposit coloured ink on each sheet of paper, then glue those paper and cut off non-object materials. Unfortunately, the company ceased trading in 2019.

2.4.2 Colour Characterisation for 3D Printers

The accuracy and consistency of colour reproduction is crucial in the 3D printing process for meeting modern aesthetic and practical needs. Reliable colour reproduction in the digital printing process is commonly achieved by performing printer colour characterisation, which defines the relationship between the input device colour space, RGB or CMY(K) and the output device-independent colour space, typically based on CIE colorimetric coordinates. This process could be divided into two models: the forward transformation aiming to predict the printed colours from the printer controlled values, and the reverse transformation derived to decompose the target colour into printer controlled values.

In the printing industry, the ICC-based colour profile is probably one of the most widely used approach to manage printed colours, and various mathematical models have been proposed for achieving higher accuracy of colour characterisation for specific purposes, such as 3D lookup tables (Green and MacDonald 2011), least-squares based polynomial regressions (Shen et al. 2012), empirical techniques based on principal component analysis (Shaw et al. 2003), the artificial neural network (ANN) (Littlewood and Subbarayan 2006), etc. Most of those models focused on simple colour transformations between RGB and CIELAB colour space.

Although the colour characterisation methods used in 2D graphic printing can be applied into 3D colour printing, it is probably difficult to achieve highly accurate colour characterisation for a 3D colour printer because there are many restrictions in 3D printing such as poor colour uniformity and different pigment penetration (Sun and Sie 2016, Yao et al. 2022). In addition, Parraman et al. (2008) reported that there are more variables that affect the finished colour of 3D colour printed objects, compared to 2D digital inkjet printing.

As colour 3D printing has become widespread in various industrial applications, it is necessary to understand colorimetric principles in 3D printing and investigate colour characterisation methods for faithful colour reproduction using 3D colour printers. Stanić et al. (2008) used two different types of colour test charts to investigate the basics of 3D colour measurements methodology, colour reproduction of basic colours and the colour gamut achievable by 3D printing. Yuan et al. (2021) reviewed colour reproduction methods in full-colour 3D printing and discussed colour accuracy issues of different colour 3D printing techniques.

For the practical applications in 3D colour printing, Xiao et al. (2016a) used a third-order polynomial regression to determine a printer colour profile transforming between printer RGB and CIE XYZ colour spaces, based on the digital Macbeth ColorChecker DC chart with 240 colour patches which was printed using a Z Corp Z510 colour printer. By printing 14 skin colour samples using the determined colour profile, the accuracy was quantified using CIELAB colour-difference formula and the average value was 4.50 CIELAB units, indicating a significant improvement compared to an average colour difference of 20.80 CIELAB units without performing colour characterisation.

In addition, with the aim of improving colour reproduction accuracy of dental prostheses, Liu et al. (2019) selected 96 colour patches to develop the colour profile of a 3D printer and the polynomial regression method with different orders were investigated to perform colour transformation between CIE XYZ and printer RGB values. With 18 tooth and gum shades printed to evaluate the 3D colour reproduction system, it was found that the third-order polynomial regression yield smaller colour differences than the quadratic polynomial, and the average colour difference achieved was 6.54 CIELAB units.

More recently, with the development of machine learning methods, it has become possible and desired to perform printer colour characterisation from complex subtractive CMYK colour system to CIELAB colour space. Velastegui and Peders (2021) used the FOGRA53 dataset consisting of 1617 colour samples and compared the performance of four different machine learning approaches: Support-Vector Regression (SVR), Artificial Neural Network (ANN), Deep Neural Networks (DNN), and Radial Basis Function (RBF) models, on colour characterisation between CMYK and CIELAB colour spaces. It was found that all these four methods could achieve very high transformation accuracy, with 99.5% of the colour-difference values obtained less than 3 units. When it came to practical printing, the DNN-based transformation method reached lower colour differences than other methods, and the average colour difference is 4.65 CIELAB units.

In the process of colour characterisation transforming from CMYK to CIELAB, Su et al. (2021) proposed an improved wavelet neural network model which was optimised by cuckoo search algorithm to reduce the colour difference. The 1296 coated FOGRA27 colour samples were employed to train the model and 100 samples were selected as the testing data. The results showed that the average colour difference of the proposed model was 3.47 CIELAB units, smaller than that of the traditional neural networks.

In generally, various methods have been applied to the process of colour characterisation of 3D colour printers to improve the accuracy of 3D colour reproduction workflow. Currently, it still lacks a standard numerical model, and a comprehensive understanding of these methods is required.

2.4.3 Colour-Difference Evaluation of 3D Printed Objects

The Section 2.1.5 reviews the currently widely used colour-difference formulae which were developed based on flat coloured samples (CIE 2001, Melgosa et al. 2017). In contrast to 2D samples, a 3D printed object has an non-uniform surface, and it is more complicated for the human visual system to process colour information, especially considering that the colour appearance of 3D objects is probably affected by 3D shape, gloss and different lighting conditions (Bloj et al. 1999, Xiao and Brainard 2008).

To understand the basic visual perception of coloured 3D objects, Hung et al. (2018) conducted a series of psychophysical experiments to quantify the visual colour differences of 3D objects using a 7-step grey scale, and it was found that chroma differences for high chroma or dark colours were not easy to visually assess. The authors suggested that the measured lightness and chroma values must be further scaled in the colour-difference formula to fit the visual data.

Jiang et al. (2021) conducted a psychophysical experiment based on 150 pairs of 3D printed samples and tested the performance of ten modern colour-difference formulae. It was reported that predictions of current colour-difference formulae were below average inter-observer variability, then they tried to optimise the k_L parametric factor in the colour-difference formulae and applied a power correction to improve the performance of colour-difference formulae in predicting visual colour differences of 3D samples. The results showed that remarkable improvements were achieved by adding a power correction with an exponent of 0.55.

Huang et al. (2022a, 2022b) used 440 pairs of 3D samples to study the influences of shape, size, and gloss on the perceived colour difference of 3D printed objects by conducting psychophysical experiments, and it was reported that these factors caused changes of visual perception. In order to test the performance of eight colour-difference formulae on predicting 3D printed objects, the visual data collected were used to quantify the agreement with the calculated colour-difference values. It was found that the CIELAB formula has the most worse performance, and the results of CIEDE2000 is equivalent to those of CIECAM02 and CIECAM16-based colour-difference formulae. Although the current colour-difference formulae were optimised to better fit the visual data, new experimental data of 3D samples are needed to develop more accurate colour-difference formulae for industrial applications.

Overall, the current colour-difference formulae developed based on 2D samples are possibly not appropriate for 3D objects, while currently there is no standard guidance for the colour-difference evaluation of 3D objects, which has stimulated industrial and academic interests. It is necessary to collect sufficient colour-difference data of 3D samples and provide a comprehensive knowledge of the visual colour perception of 3D objects.

2.4.4 Skin Colour Reproduction in 3D Printing

Colour 3D printing technologies have been applied successfully in the fabrication of soft tissue facial prostheses by combining with 3D imaging acquisition techniques. Xiao et al. (2014, 2016a) developed a colour image reproduction workflow for 3D printing facial prostheses, which are desired for patients to repair their facial deficiencies, disfigurements or injuries. Figure 2.25 shows a 3D colour image reproduction workflow for facial prostheses, including 3D image acquisition, 3D image design, colour management, colour texture mapping, 3D colour printing and postprocessing. Compared to the conventional approach to produce a soft tissue prosthesis, including the tasks of taking an impression, making a cast and hand crafting (Zardawi 2013), the advanced method based on colour 3D printing is much simpler, more efficient and low-cost.

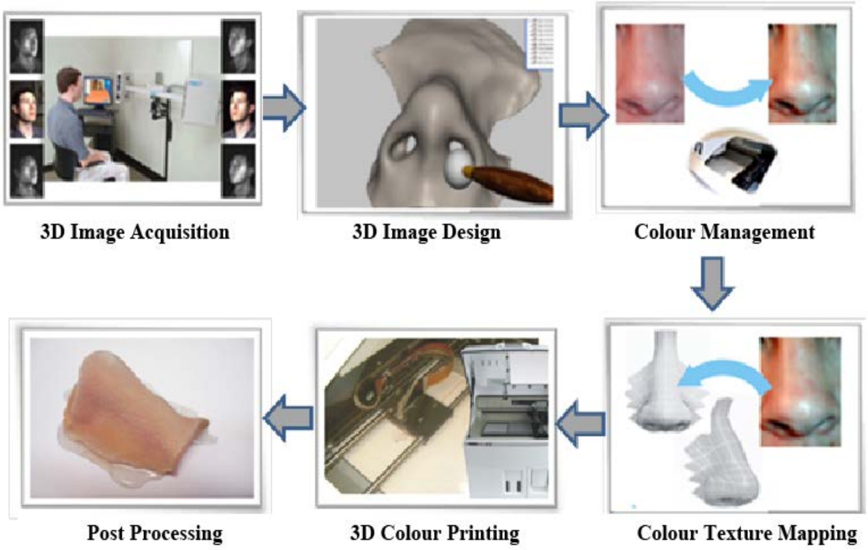

Figure 2.25 The 3D colour image reproduction workflow for facial prostheses (Xiao et al. 2014).

In the 3D colour reproduction process, colour management is one of the most important steps to achieve accurate skin colour reproduction of facial prostheses. It involves comprehensive colour characterisation for both 3D cameras and 3D printers, which was typically implemented using a conventional colour chart. In addition, the method of colour quality evaluation is another vital aspect of ensuring that the skin tones are reproduced faithfully.

In the development of a 3D colour image reproduction system for facial prostheses (Xiao et al. 2014), the colour differences achieved were 2.5-11 CIELAB units, based on 14 skin colour samples printed using a colour 3D printer. Sohaid et al. (2018) reported that the colour differences of three 3D printed facial prostheses were from 5.1 to 9.4 CIEDE2000 units, while the general acceptable colour difference for a skin-coloured specimen is 3 to 4 CIELAB units (Paravina et al. 2009). Therefore, further research into accurate colour reproduction and colour evaluation methods is needed to enhance the fidelity of skin tones achieved using colour 3D printing technologies.

2.5 Psychophysics

The tools of psychophysics are used to derive quantitative measures of perceptual phenomena that are often considered subjective (Fairchild 2005). In CIE colorimetry, psychophysical techniques provide enormous and powerful support for the research of human colour vision and colour appearance phenomena. The psychophysical experiment is of vital importance for the development of colour-difference formulae and image quality measures. Although the uncertainties associated with psychophysical experiments tend to be significantly larger than those of physical measurements, the results are equally useful and meaningful as long as those uncertainties are considered, as they always should be for physical measurements as well.

For the conduction of visual assessments in specific applications, an appropriate psychophysical technique is to be determined in experimental design in order to collect accurate visual results. This section will review the two classes of psychophysical techniques, threshold and matching method, and scaling method, that have been widely used in visual-assessment experiments within colour science, based on the book *Colour Appearance Models* (Fairchild 2005) and the ASTM E1808-96R21: *Standard Guide for Designing and Conducting Visual Experiments* (ASTM 2021).

2.5.1 Threshold and Matching Techniques

Threshold and matching experiments are designed to measure the visual perception sensitivity of human observers to a given colour stimulus. Threshold experiments are intended to determine the just-perceptible difference (JPD) in a stimulus, sometimes referred to as the just-noticeable difference (JND). Matching techniques are similar to threshold techniques, except that its goal is to determine when two stimuli are not perceptibly different.

2.5.1.1 Threshold Techniques

Threshold techniques are useful for measuring sensitivity to changes and the detectability of stimuli sensitive to small changes in stimuli (or perceptual equality). Absolute thresholds are defined as the JPD for a change from no stimulus, they are reported in terms of the physical units used to measure the stimulus, for example, a brightness threshold might be measured in luminance units (cd/m^2). While difference thresholds represent the JPD from a particular stimulus level greater than zero, and they are measured with respect to the difference between two stimuli. The lower the threshold, the higher the sensitivity. Several basic types of threshold techniques have been developed for particular applications to increase utility of the data collected, and they were divided into three types: Method of Adjustment, Method of Limit and Method of Constant Stimuli (ASTM 2021, Fairchild 2005).

The method of adjustment is the simplest and most straightforward technique for deriving threshold data, because observers control the stimulus magnitudes. This method is commonly used in matching experiments. However, it is possible to bias the results due to observer variability and adaptation effects. In contrast, the method of limit enables the experimenter to present the stimuli at predefined discrete magnitude levels in either ascending or descending series, and the threshold is defined as the minimum stimulus or difference in stimulus that can be distinguished from the reference.

In the method of constant stimuli, the experimenter chooses several stimulus magnitude levels (usually five or seven) around the threshold, and each of stimulus is presented in a random order and for multiply times. The frequency of each visual assessment can be calculated, and the threshold is generally taken to be the stimulus magnitude at which it is perceived in 50% of the trials. In the experiment of constant stimuli, two types of response can be obtained: Yes-No or Pass-Fail and Forced-Choice.

For the Yes-No procedure, observers are asked to response yes if they detect the stimulus change and no if they do not. Alternatively, the Pass-Fail procedure can be used to measure visual tolerances above threshold by providing a reference stimulus magnitude and asking observers to pass stimuli that fall below the magnitude of the reference and fail those that fall above it. The Forced-Choice procedure is to present the stimulus in one of two intervals defined by a boundary and ask observers to indicate in which of the two intervals the stimulus was presented. The observers have to make decisions even they are unsure.

2.5.1.2 Matching Techniques

Matching experiments provided the basis for CIE colorimetry, deriving the colour matching functions of the CIE standard colorimetric observers through the metameric matches. Measures of the variability in matching can be used to estimate thresholds. One type of matching experiment is called asymmetric matching that is commonly applied in chromatic adaptation experiments, where a colour match made across some change in viewing conditions. For example, in the haploscopic experiment, one eye views a test stimulus in one set of viewing conditions and the other eye simultaneously views a matching stimulus in a different set of viewing conditions until a match is produced. Another type is memory matching where observers produce a match to a previously memorised colour, such as the redness of an apple. Typically, such matches are asymmetric to study viewing conditions dependencies.

2.5.2 Scaling Techniques

Scaling experiments are intended to investigate the relationships between physical magnitudes and perceptual magnitudes of colour stimuli. Several decisions must be made by observers, depending on the type and dimensionality of the scale required. It is important to identify and decide on the suitable type of scaling method to be used before collecting data.

2.5.2.1 Paired Comparison

A paired comparison method is to present all samples in all possible pairs to the observer, usually one pair at a time, and ask observers to choose the stimulus which is closer to the reference. Since this method is not forced–choice, observers are allowed to judge both pairs of stimuli to be equal when they are unsure. The proportion of times a particular samples is judged greater in some attributes than other samples is calculated and recorded. Based on the Thurstone’s Law of Comparative Judgments (Thurstone 1927), the collected data can be transformed into interval scales on which the perceptual magnitudes of the stimuli are normally distributed.

2.5.2.2 Categorical Judgement

Categorical judgement is to ask observers to classify a large number of stimuli into various categories defined by the experimenter. It has been commonly used for colour-difference assessments. An example could be the following six categories defined for the visual experiments (Cui 2000):

1. No difference,

2. Just noticeable difference,
3. Noticeable difference,
4. Fairly large difference,
5. Large difference,
6. Very large difference.

During the visual assessments, the number of times that each sample is placed in a given category is recorded, and interval scales may be obtained by assuming that the perceptual magnitudes are normally distributed and by making use of the standard normal distribution according to the Law of Categorical Judgements (Torgerson 1954). This scaling method is an effective approach, the samples must be similar enough so that they can be placed in different categories rather than always in the same category.

2.5.2.3 Magnitude or Ratio Estimation

The magnitude estimation is to ask observers to assign numbers to the test stimuli according to the magnitude of their perceptions. Alternatively, the observers are given a number and asked to produce a stimulus with that perceptual magnitude. This is one of the few techniques that can be used to generate a ratio scale. It can also be used to generate data for multidimensional scaling by asking observers to scale the differences between pairs of stimuli.

A ratio estimation is to ask observers to find, select, or produce a sample that bears some prescribed ratios (one half or twice) to a standard, or give the observers two or more samples and ask them to state the ratios perceived in a particular attribute. In practice, this method is too difficult for most observers to use due to problems with either sample preparation or observers’ judgments.

The advantage of magnitude or ratio estimation is that observers can directly scale colour appearance attributes, such as lightness, chroma and hue, based on their visual perception of the reference stimuli under controlled viewing conditions. But the disadvantage is that the uncertainty is typically much larger than that of other matching techniques, and well-trained observers are required because of the difficulty of obtaining consistent scaling results by naive observers.

2.5.2.4 Rank Order

In a rank order experiment, the observer is asked to make an order of a given set of samples according to increasing or decreasing magnitudes of a particular perceptual attribute, e.g., the Farnsworth Munsell 100 Hue Test is designed to evaluate an individual's ability to discern colour by asking the observe to place the colour caps in order of hue. For the conduction of psychophysical experiments, it is not recommended to have one attempt to derive interval scales from rank-order data, and in order to collect consistent visual results, with a large number of observers the data may be averaged and reranked to obtain an ordinal scale.

2.5.2.5 Grey Scale

The grey scale method is to ask observers to assess the colour difference of a given pair of samples, based on the perceived colour difference from several pairs of neutral samples with different lightness. The majority of the previous colour-difference datasets were obtained using the methods of grey scale and paired comparison, e.g., Witt and Döring, (1983), Cheung and Rigg (1986), BFD (Luo and Rigg 1987a), RIT–DuPont (Berns et al. 1991), and *Leeds* (Kim and Nobbs 1997).

In order to convert the grey-scale grades (GS) given by observers to visual colour-difference results ($\Delta\mathrm{V}$), a regression technique is usually applied to derive an appropriate relationship between the GS and the $\Delta\mathrm{V}$ values. In previous studies, it could be the exponent (Luo and Rigg 1987a), polynomial with the 4th order (Melgosa et ql. 2014), and logarithm function (Jiang et al. 2021).

Additionally, the grey scale method is recommended for testing colour fastness (ISO 2010), which means the resistance of the colour of textiles to fading or running. Two grey scales consisting of nine pairs of non-glossy grey or white colour swatches were developed for assessing staining and change in colour (ISO 1993, ISO 2019).

2.6 Statistical Measures

Statistical measures are essential for quantitative data analysis, which can be used to quantify measurement uncertainty, process data collected from psychophysical experiments, test statistical significance, etc. This section will introduce basic principles and formulae of those statistical methods used in the present study.

2.6.1 Mean Colour Difference from the Mean

The concept of Mean Colour Difference from the Mean ($MCDM$) was proposed by Billmeyer and Alessi (1981) as a measure of short-term and long-term repeatability of colour measurement instruments. It is defined by averaging the colour differences between each of measurement and the mean, expressed as:

$$MCDM = \frac{\sum_{i=1,n}\sqrt{(L_i^*-\bar{L}^*)^2+(a_i^*-\bar{a}^*)^2+(b_i^*-\bar{b}^*)^2}}{n} \tag{2.43}$$

where n is the measurement number, $L_i^* a_i^* b_i^*$ are the CIELAB values of the i^{th} measurement and $\bar{L}^*\bar{a}^*\bar{b}^*$ are the averaged CIELAB values of the n measurements. The larger the $MCDM$ values, the lower the repeatability of the instrument. Typically, the calculation of $MCDM$ uses the CIELAB colour-difference formula. As the development of colour-difference formulae, the $MCDM$ calculation formula can be expressed as:

$$MCDM = \frac{\sum_{i=1,n}[f_{\Delta E}(V_i, V_{ave})]}{n} \tag{2.44}$$

where $f_{\Delta E}$ is a colour-difference formula, such as CIELAB and CIEDE2000.

The metric of $MCDM$ is used to evaluate the precision random errors of a photo-electric colour measurement instrument such as spectroradiometers and spectrophotometers, e.g., Wang et al. (2018) calculated $MCDM$ to assess the consistency within and between colour measurement instruments. For a given sample measured using a modern instrument, the $MCDM$ value of a set of measurements can usually be expected to be about 0.1 (or less) of a CIELAB colour difference unit (Hunt and Pointer 2011). Another use of $MCDM$ is to quantify colour variations (Cui et al. 2001) or intra- and inter- observer variability in a psychophysical experiment (Sarkar et al. 2010).

2.6.2 StandardiSed Residual Sum of Squares

The index of Standardized Residual Sum of Squares ($STRESS$) was proposed by García et al. (2007) and adopted by CIE (2016) to test the performance of two colour-difference formulae with respect to a given set of visual colour-difference data. It is expressed as:

$$STRESS = 100\sqrt{\left(\frac{\sum(\Delta E_i - f\Delta V_i)^2}{\sum f^2 \Delta V_i^2}\right)} \tag{2.45}$$

where $f = \frac{\sum \Delta E_i^2}{\sum \Delta E_i \Delta V_i}$, ΔE_i indicates the colour difference of the i^{th} testing pair calculated using a colour-difference formula, such as CIELAB and CIEDE2000, ΔV_i means the average visual colour difference of the i^{th} testing pair given by observers. The $STRESS$ value ranges from 0 to 100, and for a perfect agreement, the $STRESS$ value should be zero. The larger the $STRESS$ value, the less the agreement between the perceived and calculated colour differences. This metric has been widely used for testing the performance of colour-difference formulae (Melgosa et al. 2008, Huang et al. 2015, Mirjalili et al. 2019, Jiang et al. 2021).

The $STRESS$ is also used to quantify intra- and inter-observer variability in visual colour-difference assessments (Melgosa et al. 2011). For each observer, intra-observer variability is calculated as the average of $STRESS$ values of each replication made by the observer with respect to the average result of all the replications, while inter-observer variability is calculated as the $STRESS$ value between the average result of all the replications made by the observer and the average result of all the observers. Final intra- and inter-observer variability is defined as the average intra- and inter-observer variability $STRESS$ values.

2.6.3 Statistical Significance Test

Although $STRESS$ values can be used to compare the performance of two different formulae, it is not sufficient to indicate the degree of statistical significance. In order to quantify the significance of the difference between two colour-difference formulae or colour spaces tested, the measure based upon statistical F-test was used by Luo et al. (2006). With the introduction of $STRESS$ metric, García et al. (2007) proposed the following equation to perform F-test using $STRESS$ values, defined as:

$$F = \frac{STRESS_A^2}{STRESS_B^2} \tag{2.46}$$

where A and B indicates two different colour-difference formulae.

The statistical significance analyse is based on the confidential interval $[F_C, 1/F_C]$, where F_C is the critical value, and $F_C = F(df_{A,}\, df_{B,}\, 0.975)$ for the two-tailed F distribution with 95% confidence level, df_A and df_B are the degrees of freedom. The critical value F_C can be found from statistical textbooks and the results can be divided into five categories:

- If $F < F_C$, A is significantly better than B;
- If $F_C \leq F < 1$, A is insignificantly better than B;
- If $F = 1$, A is equal to B;
- If $1 < F \leq 1/F_C$, A is insignificantly poorer than model B;
- If $1/F_C \leq F$, A is significantly poorer than B.

The F-test based on $STRESS$ has been widely used to test the performance of different colour-difference formulae and analyse statistical significances (Melgosa et al. 2008, Huang et al. 2015, Mirjalili et al. 2019, Jiang et al. 2021).

2.6.4 Pearson Correlation Coefficient and Coefficient of Determination

The Pearson correlation coefficient (PCC), also known as Pearson's r, is the most common way of measuring a linear correlation between two sets of data. It is the ratio between the covariance of two variables and the product of their standard deviations, defined as:

$$r(x,y) = \frac{\sum(x_i - \bar{x})(y_i - \bar{y})}{\sqrt{\sum(x_i - \bar{x})^2 \sum(y_i - \bar{y})^2}} \tag{2.47}$$

where x_i, y_i are the i^{th} sample of the two data sets, $\bar{x}, \bar{y}$ are the average of all the samples in each data set. The Pearson's r value ranges from -1 to +1 where a value of +1 denotes a perfect agreement, 0 denotes no linear correlation, and -1 denotes a totally negative linear correlation. When the r value is close to -1 or 1, it means that the two sets of data have a stronger positive or negative correlation.

The square of the Pearson correlation coefficient, also known as the coefficient of determination (r^2 or R^2), is more commonly used to indicate the variance in the dependent variable that is accounted for by the variance in the independent variable. In regression, it is a measure of the goodness of fit of a model, i.e., how well the regression predictions approximate the real data points. The value of r^2 ranges from 0 to 1, and $r^2 = 1$ for a perfect fit.

2.7 Summary

In this chapter, the fundamental theories and previous studies relevant to the present PhD work were reviewed. Starting from the basic knowledge and principle of CIE colorimetric system, followed by literature surveys on skin and skin colour measurement. Then the colour characterisation methods for digital cameras and 3D printers were described, furthermore, the studies on 3D colour image reproduction were reviewed and discussed. In addition, the psychophysical techniques and statistical measures were introduced which are crucial for quantitative data analysis. Basically, the goal of this chapter is to provide appropriate references and give an overview of the topic of the present work for further reading and understanding.

Chapter 3
Methodology

3.1 Workflow of 3D Face Colour Reproduction

To achieve the aim and objectives of the present study, a workflow as illustrated in Figure 3.1 was developed for colour reproduction of human faces. The first step is to capture the digital 3D model of the target face including colour and geometric information using a 3D imaging system. For the purpose of achieving accurate colour images, the second step is to perform colour characterisation for the 3D cameras so that the camera RGB images can be transformed to CIE colour space which is device independent. The third step is to develop a colour profile of the 3D printer to convert the colour image from CIE colour space to the printer RGB/CYMK colour space for faithful colour reproduction. The next step is to project the characterised colour image to the manipulated 3D face model whose polygon mesh was repaired in a 3D modelling software to make the model watertight and 3D printable. Then the ready 3D face model is sent to the colour 3D printer, and after the printing is completed, the 3D printed model is taken away from the 3D printer for postprocessing, such as support material removal and polishing. The last step is to evaluate the colour quality of the 3D printed model compared to the actual face. In this workflow, colour management, including colour measurement and colour characterisation for the 3D imaging system and the 3D printer, and the evaluation of colour reproduction accuracy are key work.

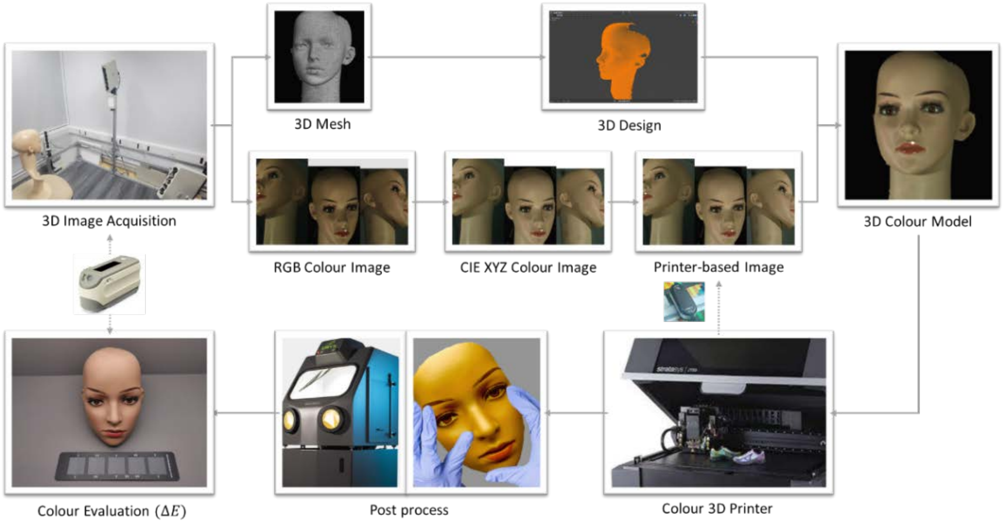

Figure 3.1 The 3D colour reproduction workflow for faces.

3.2 Apparatus

3.2.1 3dMDface System

The 3dMDface system, as shown in Figure 3.2 (left), was adopted to capture 3D images of human faces. It incorporates nine computer vision cameras from three modular units, and an industrial-grade flash system was built in for each modular unit. The 3dMD Acquisition software (3dMDface Acquisition, 3dMD, Atlanta, GA) was used to control this system to simultaneously capture colour images of a human face from the three directions with different camera viewpoints. The capture time is about 1.5 milliseconds, and the captured facial image covers 180° of the face, from ear to ear.

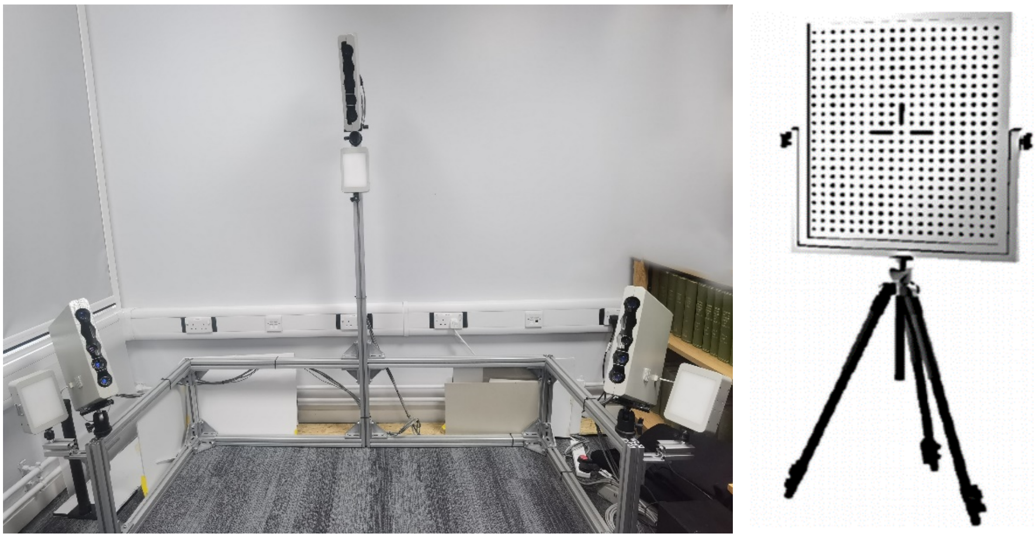

Figure 3.2 The 3dMDface system (left) and the calibration frame (right).

Before 3D facial image acquisition, a calibration procedure is required to ensure that the 3D imaging system produces accurate data measurements and alignment of the objects being captured. This process is performed in a dark environment using its build-in flash, and the calibration frame, as shown in Figure 3.2 (right), is placed in a specific position so that the cross centre can be shown simultaneously in the three live view windows captured using the cameras from three directions. In the calibration process, the 3D image acquisition of the calibration frame needs to be taken twice. For the first capture, the calibration frame is tilted 15° forward, and it is tilted 15° backward for the second capture. Figure 3.3 presents the two image acquisitions of the calibration frame. The calibration is not successful until the centre of the frame is simultaneously captured from three directions and the same to both captures. A successful calibration is necessary for the 3D imaging system to capture 3D digital models.

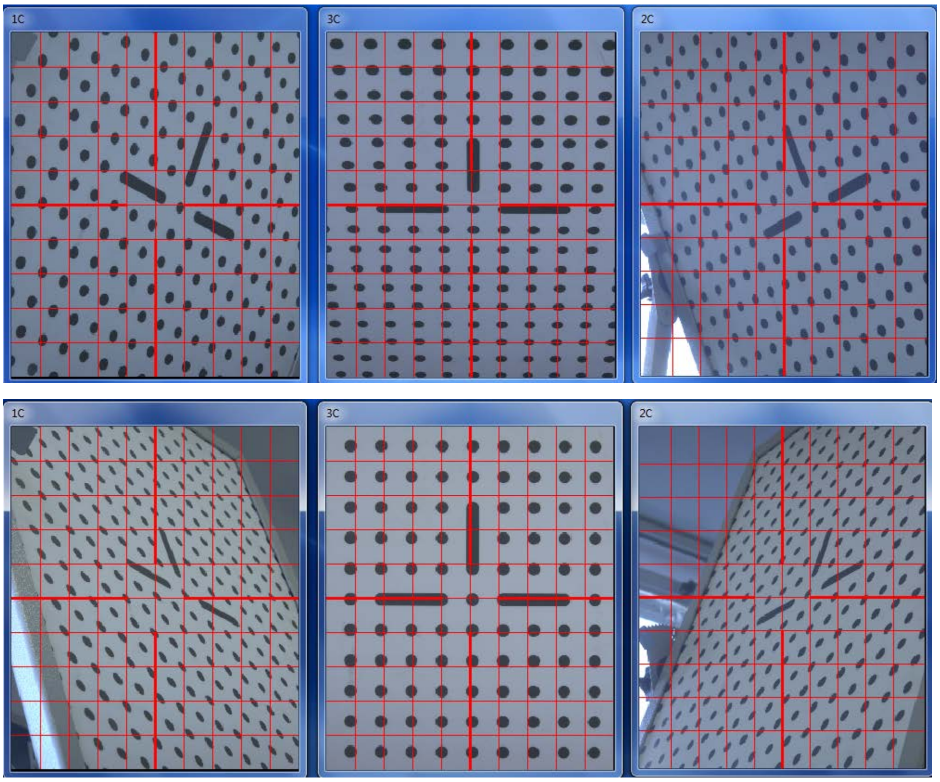

Figure 3.3 The two image acquisitions of the calibration frame in the 3dMDface system.

Based on the speckle projection technique, this system can generate a continuous 3D polygon surface mesh with a single x, y, z coordinate system from all viewpoints, and an object file is created containing the geometric data of the targe subject. Figure 3.4 shows the captured speckle projection images of a mannequin face. Simultaneously, three colour images of the face are captured using the cameras in three module units, and a bitmap image consisting of the three colour images is created to record the colour and texture information of the object, as shown in Figure 3.5. This texture bitmap image will be automatically linked and mapped to the 3D mesh model in a 3D viewer software, based on a MTL (material template library) file which is generated to specify colour, texture and reflection characteristics.

In generally, three files (obj, bmp and mtl) are created using the 3D imaging system to generate the digital 3D colour model of the face. Additional 3D data manipulation is required to repair and smooth any bad edges and make the 3D model printable. Considering that the colour appearance of a 3D face model is dependent on the 2D colour bitmap image captured using the 3D imaging system, it is therefore necessary to achieve accurate colour reproduction of the bitmap image and map it onto the 3D face model.

Figure 3.4 The captured speckle projection images of a mannequin face.

Figure 3.5 The captured texture bitmap image of a mannequin face.

3.2.2 3D Colour Printer

Based on the Polyjet colour 3D printing technology, the Stratasys J750™ colour 3D printer is able to achieve full colour 3D printing (over 500,000 colours) and create realistic prototypes with texture mapping. The size of its build tray is 490 × 390 × 200 mm, as shown in Figure 3.6. The printer supports a wide range of material properties, from rigid to flexible and opaque to transparent. The printing materials that mix together to produce a wide range of colours are VeroCyan, VeroMagenta, VeroYellow, Vero PureWhite and VeroBlackPlus™. The VeroClear material is available to adjust the opacity or translucence of the colour applied to the 3D model when needed. In this study, the VeroClear material was not used and all the printed samples were opaque. Regarding the support material, it has two options: SUP705 which can be removed with a waterjet system, and SUP706 which is soluble and easily removed in automated post-processing. In addition, there are three options of printing mode for this 3D printer: the high-speed mode using up to 3 base resins to produce in 27-micron layers, the high-quality mode using up to 6 model materials to print in 14-micron layers, and the high-mix mode using up to 6 base resins to print in 27-micron layers.

Figure 3.6 Stratasys J750^{TM} colour 3D printer.

The GrabCAD Print (GrabCAD Print, Stratasys, Rehovot, Israel) offers an open software platform for preparing print jobs on a variety of 3D printers, including the Stratasys J750 printer. The 3D printer print using the CMYK colour gamut while computer monitors use the RGB colour gamut, a sRGB icc profile and an icc profile containing the colour gamut of the printer were available in the GrabCAD Print software so that the RGB-based colour models can be printed using the Stratasys J750 printer.

3.2.3 Spectrophotometer

Two spectrophotometers, the Konica Minolta CM-2600d and the Konica Minolta CM-700d, as shown in Figure 3.7, were used to take colour measurements. Both are portable and handheld colour measurement instrument with a diffuse illumination and 8-degree viewing system (d:8°), equipped with simultaneous SCI (specular component included) and SCE (specular component excluded) measurement, and they have been widely used to measure the colour of skin (see Table 2.5 in Section 2.2.3.1).

Before taking colour measurements, the spectrophotometer should be calibrated in accordance with the manufacturer’s recommendation, typically performing dark and white calibration using the provided samples. In this study, a small aperture size of SAV 3 mm and SCI measurement mode was adopted to measure the colour of human faces and 3D printed objects. The SpectraMagic NX software (SpectraMagic NX, Konica Minolta, Tokyo, Japan) is compatible to record spectral reflectance data with wavelengths ranging from 360 nm to 740 nm and intervals of 10 nm.

Figure 3.7 Konica Minolta CM-2600d spectrophotometer (left) and CM-700d spectrophotometer (right).

3.3 Colour Management

The colour of the printed object is not only affected by the colour behaviours of the 3D printer, but also the colour accuracy of the 3D model captured using the 3D imaging system. Therefore, it is crucial to ensure consistent and accurate colour reproduction from 3D image acquisition to 3D colour printing. Based on the conventional colour management approaches developed for 2D colour image reproduction, a dedicate colour management pipeline has been applied to the workflow of 3D colour image reproduction. As shown in Figure 3.8, the colour image captured using the 3D imaging system is firstly transformed to CIE colour space, such as CIE XYZ and CIELAB, and then converted to the 3D printer-based colour space. In this process, it is of vital importance to determine a colour characterisation model with high accuracy for the 3D imaging system and the 3D colour printer, respectively.

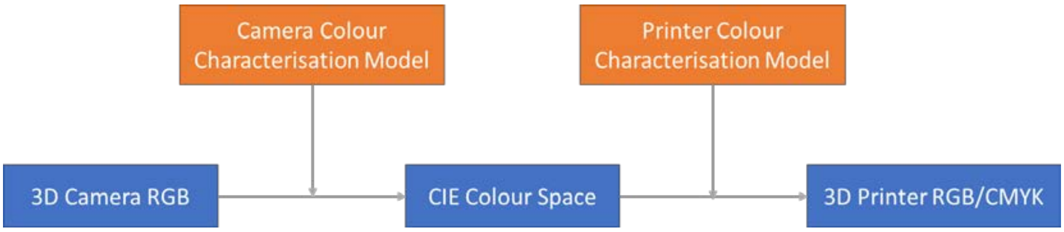

Figure 3.8 The process of colour management in 3D image reproduction.

Since the colour information of an object captured using the 3dMDface system is stored in a 2D bitmap image, it is practicable to apply the conventional colour image reproduction workflow, but specific colour characterisation methods are required to achieve higher accuracy for reproducing skin tones. Therefore, a specialised 2D digital imaging system for capturing human faces was developed to investigate the factors affecting camera colour characterisation, such as training dataset, image format and mapping methods. Furthermore, the prediction accuracy of different colour characterisation models was quantified not only using the typical colour difference method but also two newly proposed measures based on real human facial skin. The details of this part of work are described in Chapter 4.

In the light of the findings reported in 2D camera colour characterisation, a suitable and feasible method was applied to the 3D imaging system for accurately predicting the colour of facial skin from the pixel-based images, and more information is given in Chapter 4. The colour characterisation for 3D cameras makes the captured facial colour image independent of the 3D imaging system and can be communicated between different devices.

It is no doubt that the colour quality of a 3D printed object is not only affected by the quality of the captured image but also the 3D printer itself. As an output device, it is critical to understand the colour characteristics of the printer for accurate colour reproduction. Basically, printer colour characterisation is performed to transform colours between the printer-based colour space and a device-independent colour space, and the accuracy of a printer colour model can be affected by a wide variety of factors. It is therefore necessary to compare different colour characterisation methods and develop a specific protocol for the 3D printer to achieve accurate skin colour reproduction. In Chapter 5, different methods including conventional polynomial regression and new machine learning techniques were investigated on the performance of colour characterisation for a 3D printer, in both colorimetric and spectral-based approaches. Additionally, a practical accuracy of the colour characterisation model was reported based on the Stratasys J750 colour 3D printer.

In generally, colour management in the 3D colour image reproduction workflow is to determine a validated colour characterisation model for the 3D cameras and the 3D printer, respectively, which can be applied to ensure that the skin tones can be faithfully reproduced in the 3D printing process.

3.4 Colour Reproduction Evaluation

In addition to colour management, colour quality evaluation is also an important part in the workflow of accurate colour reproduction of human face using 3D printing technology. Typically, the colour-difference formulae such as CIELAB and CIEDE2000 are used to quantify the accuracy of 3D printed objects, but these formulae were developed based on 2D colour samples, and currently there is no standard guidance for the colour-difference evaluation of 3D objects. Consequently, it is necessary to collect visual colour-difference data of 3D objects, and comprehensive knowledge of the visual colour perception of 3D objects is highly desired, especially considering that it has become a topic of great concern in various industrial applications with the rapid development of colour 3D printing technologies.

To investigate the human colour perception of 3D objects in terms of the lightness, chroma, and hue dimension, psychophysical experiments were conducted to collect visual colour-difference data of 3D printed objects, which were used to test the performance of CIELAB and CIEDE2000 colour-difference formulae. Furthermore, the parametric factors in colour-difference formulae were optimised to better fit the visual colour-difference data of 3D objects, and the modified colour-difference formulae were validated using 3D printed skin colour samples. This part of research work is presented in Chapter 6.

Regarding the evaluation of the 3D colour image reproduction workflow, the accuracy is quantified by calculating the colour difference between the actual human face and the 3D printed model, which involves the precision of the 3D imaging system and the fidelity of the 3D colour printer. In Chapter 7, a 3D human face model was printed practically using the developed 3D colour image reproduction workflow integrated with the specific colour characterisation and colour evaluation methods.

Chapter 4
Image Measurement for Human Faces

In this chapter, a specific digital imaging system for human face was developed to measure skin colour based on the captured images, and the factors that affect image-based skin colour measurement, such as image format, training data, mapping method, were comparatively investigated for the development of camera colour characterisation model, which is the most important for transforming camera RGB values to CIE colorimetric values.

Typically, the method for quantifying predictive accuracy of camera colour characterisation is to use CIELAB or CIEDE2000 colour-difference formula based on a group of testing data of uniform colour patches. It is usually taken for granted that good prediction of the testing colours will lead to good performance on whole images in most cases, but this does not fairly represent what happens in practice, especially for facial skin with non-uniform colour. As a result, additional measures to evaluate the predictive accuracy of facial skin colour were introduced in this chapter. In addition, based on the designed digital imaging acquisition system for human face, a case study was conducted to investigate how the illuminations with different CCTs affect skin colour heterogeneity. Moreover, the colour characterisation was implemented for the 3D imaging system to capture accurate and consistent facial images.

4.1 Development of a 2D Imaging System

4.1.1 Design and Apparatus

To obtain good-quality colour images for quantitative analysis, a specific digital imaging system consisting of a high-resolution digital SLR camera and two THOUSLITE® LED Cubes was developed, as illustrated in Figure 4.1. The position of each component in the digital imaging system is of vital importance, because it could affect the results of colour characterisation for the camera and skin colour measurement based on the captured images once each parameter is changed.

The two LED Cubes were placed symmetrically towards the position of the human face. In literature survey, it was suggested that two directional light sources at 45° to the subject plane could achieve near-uniform illumination (Hunt and Pointer 2011). However, considering that the LED Cube is a lighting panel with a size of 300 × 300 mm (the whole dimension is 300 × 300 × 210 mm) rather than a spotlight, it is not appropriate to define as 45°. Finally, the angle of each LED Cube edge to the horizontal plane was defined as 60°, aiming to provide as uniform lighting on the human face as possible. The illumination uniformity in the developed digital imaging system was tested and the results will be given in Section 4.1.3.

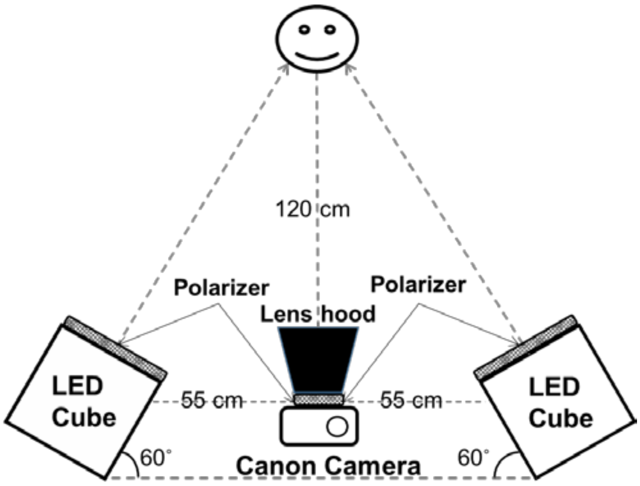

Figure 4.1 Schematic diagram of the developed digital imaging system for capturing human faces.

The Canon EOS 6D Mark II digital camera equipped with a Canon EF 24-105 mm lens, as shown in Figure 4.2 (left), was used to take image capture. It was located in the horizontal centre of the two LED Cubes. In order to avoid most specular lights in the captured images caused by reflection, a cross linear polariser with a size of 300 × 300 mm was placed vertically in front of each LED Cube to filter out the glare, and a Kalimar PL 77mm filer, as shown in Figure 4.2 (right), was placed over the camera lens with a specific rotational angle for polarisation.

Figure 4.2 Canon EOS 6D Mark II digital camera equipped with a Canon EF 24-105 mm lens (left) and the Kalimar PL 77mm filer (right).

Normally, the maximum degree of polarisation occurs in a circular degree of 90°, and the angle for minimum polarisation is 0°. Although a polarisation degree of 90° can remove most of glares in the facial images, it also causes dimming and colour shifts in the captured image, as shown in Figure 4.3 where the face of a mannequin face was captured at 0°, 45°, 75°, 90°. With the aim of producing diffuse light on the face without changing too much skin tones in the image, different polarisation degrees ranging from 0° to 90° were tested, and finally, the polarisation degree was determined as 75° to achieve good colour quality of the captured facial images.

0° 45° 75° 90°

Figure 4.3 Colour images of a mannequin face captured at polarisation degrees of 0°, 15°, 45°, 90°.

To make the digital camera in a stable and repeatable condition, the manual mode was selected for image capture instead of using automatic mode. A X-Rite ColorChecker Classic chart (see Figure 2.21) was used to determine the camera settings, which were specifically ISO 640, aperture size f/5.6, shutter speed 1/8 second. The white balance was customised as the colour temperature mode, corresponding to the CCT of the light illuminated on the human face. Table 4.1 lists the fixed settings of the digital camera before taking image captures, both JPEG and RAW images were saved. Additionally, a matt black lens hood was equipped in front of the camera lens to prevent any stray light of the two LED Cubes from directly entering the camera lens during image captures.

Table 4.1 Camera settings for capturing facial images.

ISO	Shutter speed	Aperture	White balance	Focal length	Polariser angle	Image format
640	1/8 s	f/5.6	Customised Colour Temperature	85 mm	75°	JPEG & RAW

4.1.2 The Lighting System

Based on the stable and computer controlled THOUSLITE LED technology which can generate a spectral power distribution with specific requirements, an illumination with a CCT of 6500 K was created and reproduced using the two LED Cubes. A Konica Minolta CS2000 tele-spectroradiometer, as shown in Figure 4.4 (left), was placed in the position of the camera and used to measure the created illumination against the THOUSLITE standard white tile (Figure 4.4 (right)) which was placed at the position of the human face.

Figure 4.4 Konica Minolta CS-2000 spectroradiometer (left) and THOUSLITE standard white tile (right).

The parameters of the simulated D65 illumination were measured using the CS-2000 spectroradiometer and given in Table 4.2. Figure 4.5 shows the measured relative spectral power distribution (SPD) of the illumination, which was used to calculate CIE XYZ and CIELAB values with the spectral reflectance measured on human faces. The simulated D65 illumination was saved in the LEDNavigator software (LEDNavigator V5.3.4, THOUSLITE, Changzhou, China) with its parameters and SPD so that it can be reproduced and used next time for taking image captures.

Table 4.2 The measured parameters of the simulated D65 illumination in the digital imaging system.

	CCT	Ra	Duv	Luminance
D65	6544 K	95	0.0064	127.45 cd/m^2

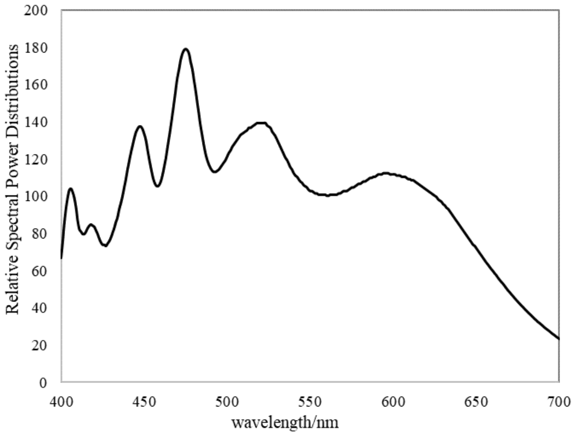

Figure 4.5 The relative SPD of the simulated D65 illumination in the digital imaging system.

4.1.3 System Validation

The uniformity of the lighting in the target area was tested by using a uniformity board, which was placed at the same position as the human face and then captured using the digital camera with the same settings. The intensity of each pixel was derived from the captured image, and the histograms of red, green and blue channels are shown in Figure 4.6. In order to quantify the lighting uniformity, the RGB values in the target area were converted to CIELAB values using the default $rgb2lab$ function in MATLAB (MATAB 2020, MathWorks, Natick, MA), note that the colour accuracy was not the aim in this step. The results showed that the lightness L^* values ranged from 76.5 to 78.5 in the subject area, which are very similar, and the $MCDM$ value calculated using CIELAB colour-difference formula was 0.39. It is indicated that the light illuminated on the area of the face is uniform and constant, which can used for quantitative image analysis on skin colour measurement. In addition, it can be seen from the RGB intensity histograms that the white balance of the camera is good for capturing images, with no or very few colour shifts of the neutral board.

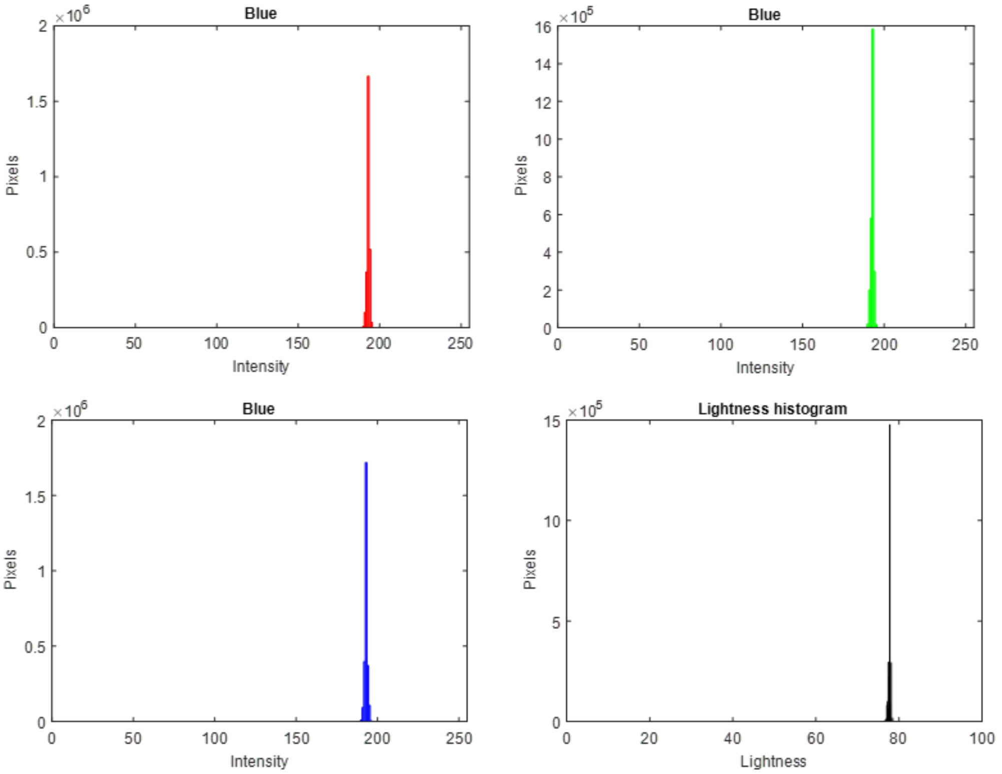

Figure 4.6 Histograms of RGB intensity and lightness L^* for testing lighting uniformity.

The camera responses to light intensity were characterised using the grey scales (12 neutral patches) in the ColorChecker Digital SG chart (Figure 2.21). Both RGB and RAW images of the chart were saved, and the digital data of each neutral patch were extracted in MATLAB. A Konica Minolta CM-2600d spectrophotometer was used to measure the light intensity of each neutral patch. The relationship between the camera response and light intensity is illustrated in Figure 4.7, where the non-linear relationship (left) is for RGB image data, and the linear relationship (right) is for RAW image data.

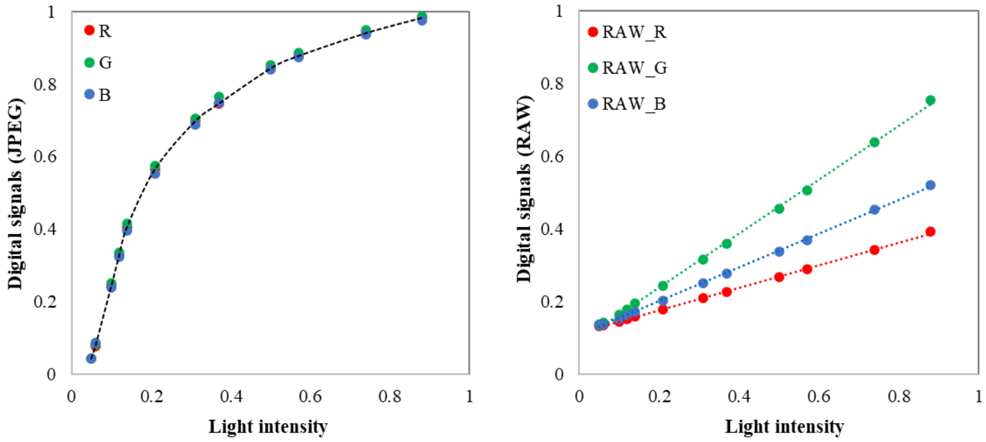

Figure 4.7 The relationship between light intensity and camera digital responses for RGB (left) and RAW (right) image data.

4.1.4 Image Acquisition

The image acquisition process for human faces was conducted in a dark room, and the LED lighting system produced the only illumination. The Canon EOS 6D Mark II DRGB camera with specific settings (see Table 4.1) was connected to Canon EOS Utility software (EOS Utility 3, Canon, Tokyo, Japan) to remotely control image captures. Before attending the collection of facial images, the human participant was asked to keep face clean without any makeup, and no bangs of hair in front of forehead. Then the participant was instructed to sit in front of the camera at a distance of about 120 cm (See Figure 4.1) and put face on a fixed chin rest. Moreover, the participant was asked to keep still and look at the camera lens, the digital camera was controlled remotely to capture the image of the face against a black background. Figure 4.8 shows the shooting interface of a mannequin face.

Both JPEG (.JPG) and RAW (.CR2) images of the human face were automatically saved in the computer after each capture. The resolution of the image is 6240 pixels (width) × 4160 pixels (height), equal to a 26 MP image with a 3:2 aspect ratio. It is important to ensure that each captured image is clear and sharp. If an image is blurry, it needs to be captured again until a clear image is obtained.

WhiteBalance
Color Temperature
6500 K
☑ Apply to shot images
Focus
Live 1-point AF
Picture Style Neutral
Detail set. 7 , 2 , 2 , 0 , 0 , 0
WB SHIFT 0,0
HDR Mode Disable HDR

Figure 4.8 The remote shooting interface of capturing a mannequin face.

4.2 Spectrophotometer Measurement

The Konica Minolta CM-2600d spectrophotometer with a SAV aperture and SCI measurement mode, as shown in Figure 3.7, was used to measure the skin colours of five facial positions: forehead (FH), right cheekbone (CBR), left cheekbone (CBL), nose tip (NT) and chin (CH), as illustrated in Figure 4.9. The measurement position for the forehead is the intersection of the horizontal midline of the whole forehead and the vertical midline of the whole face, and it is similar to take colour measurements on the chin. For colour measurement on both cheekbones, the position is the centre of the cheekbone. The spectral reflectance data measured using the spectrophotometer were used to calculate the corresponding CIE XYZ tristimulus values and CIELAB values with the CIE 1931 standard colorimetric observer and the SPD of the simulated D65 illumination used in the digital imaging system. To evaluate the predictive accuracy of camera colour characterisation in section 4.4, the spectrophotometer measurement data were considered as the ground truth and compared to the predicted results.

In the present study, 144 human subjects from different ethnicities were invited to participate in the capture of facial images and skin colour measurements. Table 4.3 gives the number of the participants by ethnicity and gender. It can be seen that most participants are female, and there are more Chinese and Caucasian than other ethnicities. The “others” in Table 4.3 indicates 6 Africans, 4 Japanese, 1 Pakistani, 1 Arab and 1 Turk. Most of the participants were in the age group of 20-29 years. Before their participation, each was asked to sign a consent form, in accordance with the ethical review procedure of the University of Leeds. Figure 4.10 plots all the measured spectral reflectance data of facial skin colours collected from the 144 human participants.

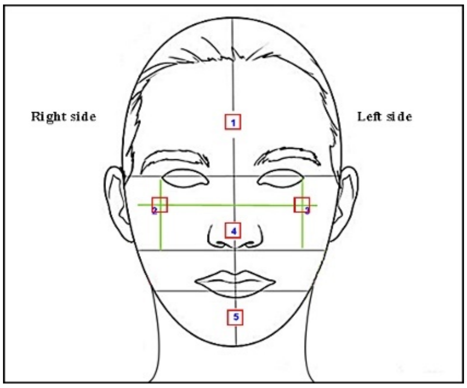

Figure 4.9 The five positions measured on each human face (1. forehead, 2. right cheekbone, 3. left cheekbone, 4. nose tip, 5. chin).

Table 4.3 Information about the participants.

	Chinese	Caucasian	Indonesian	Mexican	Others	Sum
Male	11	15	9	6	2	43
Female	40	17	22	11	11	101
Sum	51	32	31	17	13	144

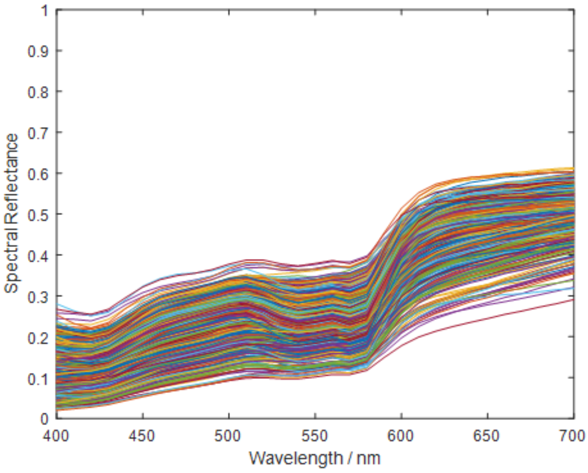

Figure 4.10 The spectral reflectance measured on the five facial locations of 144 human participants.

4.3 Colour Characterisation for the Digital Camera

A camera colour characterisation model is usually determined based on a reference colour chart (also called training data) and a mapping method. This section will introduce different image formats, training datasets, and mapping methods that were used for the determination of camera colour characterisation models.

4.3.1 Image Formats

Both RGB and RAW image data were used as the camera digital signals to predict skin colours. For the saved JPEG images, the RGB values of each pixel were extracted using the *imread* function in MATLAB. For the RAW images, the open source raw-files converter *dcraw* was used to decode the RAW image to TIFF format without colour correction (Coffin, 2018), and the RAW RGB values of each pixel was derived from the decoded TIFF image in MATLAB.

4.3.2 Training Datasets

The two existing colour charts: X-Rite ColorChecker Digital SG chart with 140 colour patches as shown in Figure 2.21 (right) and the Spectromatch silicon skin colour chart with 95 colour samples as shown in Figure 2.18, were selected and used separately as the training dataset for the determination of the camera colour characterisation model. Based on the developed digital imaging system, each colour chart was placed in the same position as the human face and captured using the digital camera with the same settings. The averaged RGB/RAW values of each patch were derived from the captured images in MATLAB. In addition, the spectral reflectance of each colour patch was measured using a CM-2600d spectrophotometer, and the corresponding CIE XYZ tristimulus values and CIELAB values were calculated with the CIE1931 CMFs and the measured SPD of the 6500 K illumination.

From the facial skin colour data collected in this study, the colour data of 200 facial locations of 40 human subjects (10 Caucasian, 10 Chinese, 10 Indonesian and 10 Mexican) were used as a separate training dataset, which include the CIE XYZ tristimulus values calculated from the spectral reflectance data measured using the spectrophotometer and the RGB/RAW image data of the five facial positions in the captured images. Specifically, an area of 50 × 50 pixels was selected for each position in the facial image, trying to keep the facial positions for image data extraction the same as those for spectrophotometer measurements. The RGB/RAW values of the 2500 pixels were averaged to represent the image data of the facial position. Overall, three training datasets were used for performing camera colour characterisation, which are:

- CCSG: the X-Rite ColorChecker Digital SG chart with 140 colour patches,
- SSCC: the Spectromatch silicon skin colour chart with 95 skin colour samples,
- FSCD: the 200 facial skin colour data collected from human participants.

4.3.3 Mapping Methods

The linear transformation, polynomial regression (PR) with 1-3 orders, root-polynomial regression (RPR) with 1-3 orders and neural network (NN) were used as the mapping methods to transform camera image data to CIE XYZ tristimulus values, respectively. For the PR and RPR methods, the extension terms of each order are listed in Table 4.4, note that the first order PR and RPR has the same terms and was named as 1st PR. For the neural network method, the *fitnet* function in MATLAB was used with the *trainbr* method (Bayesian regularization backpropagation) to train an optimised mapping between the input (RAW/RGB values) and output vectors (CIE XYZ tristimulus values). The architecture used has three hidden layers, where the first hidden layer size is 5, the second is 25, the third is 5, and the number of epochs is 1000. Specifically, seven mapping methods used for performing camera colour characterisation.

Table 4.4 The extension terms for linear, 1st PR, 2nd PR, 3rd PR, 2nd RPR, and 3rd RPR methods.

	Number	terms
Linear	3	r, g, b
1st PR	4	$r, g, b, 1$
2nd PR	10	$r, g, b, r^2, g^2, b^2, rg, rb, gb, 1$
3rd PR	20	$r, g, b, r^2, g^2, b^2, rg, rb, gb,$ $r^2g, r^2b, g^2b, rg^2, rb^2, gb^2, r^3, g^3, b^3, 1$
2nd RPR	7	$r, g, b, \sqrt{rg}, \sqrt{rb}, \sqrt{gb}, 1$
3rd RPR	14	$r, g, b, \sqrt{rg}, \sqrt{rb}, \sqrt{gb}, \sqrt[3]{r^2g}, \sqrt[3]{r^2b}, \sqrt[3]{b^2g},$ $\sqrt[3]{rg^2}, \sqrt[3]{rb^2},, \sqrt[3]{gb^2}, \sqrt[3]{rgb}, 1$

4.3.4 Determination of Colour Characterisation Models

Based on the three training datasets (CCSG, SSCC, FSCD) with known CIE XYZ tristimulus values calculated under the simulated D65 illumination and the corresponding RAW/RGB values extracted from the captured image, the seven mathematical methods, linear, 1st PR, 2nd PR, 3rd PR, 2nd RPR, 3rd RPR and NN, were applied respectively to determine the colour characterisation model with the least-square fitting method. A total of 42 different colour characterisation models (2 image formats × 3 training datasets × 7 methods) were generated to predict facial skin colours in terms of CIE colorimetric values from the captured images.

4.4 Validation of Colour Characterisation Models

4.4.1 Testing Dataset

The 100 facial skin colour data collected from 20 participants (5 Caucasian, 5 Chinese, 5 Indonesian and 5 Mexican) were used as the testing data, which are different from the FSCD training dataset. Figure 4.11 shows the distributions of the collected skin colour data in the CIELAB lightness-chroma L^*C^* plane (a) and the chromatic a^*b^* plane (b), where the dot symbols indicate the 200 skin colours that were used as a training dataset, and the cross symbols denote the 100 skin colours that were used as the testing data to evaluate the performance of the model determined. The training and testing datasets are openly available in Zenodo (He 2021).

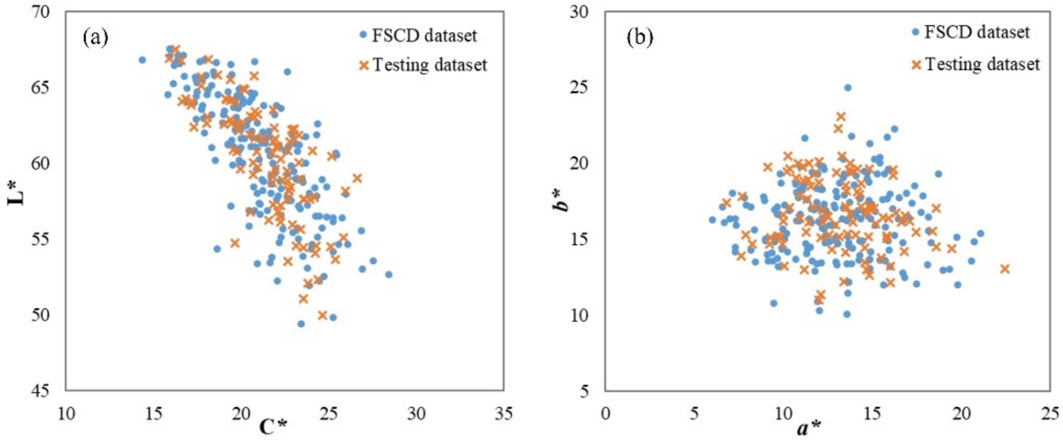

Figure 4.11 Colour distributions of the FSCD training data and the testing data in CIELAB L^*C^* (a) and a^*b^* (b) plane.

For the facial images collected as the testing data, the RGB/RAW values of each facial location were derived from an area of 50 × 50 pixels, and the averaged values were transformed to CIE XYZ values using each colour characterisation model generated. The colour prediction accuracy was evaluated not only by using the conventional method of CIELAB colour difference, but also the two newly introduced measures, facial colour contrast and skin colour gamut.

4.4.2 Colour Difference

The traditional method for quantifying the prediction accuracy of colour characterisation model is to calculate the averaged CIELAB colour difference between instrument measurements and the corresponding predictions of a group of testing data. The equation is expressed as:

$$\Delta E_{ab}^{*} = \frac{1}{n}\sum_{i=1}^{n} \sqrt[2]{(L_{0i}^{*} - L_{1i}^{*})^2 + (a_{0i}^{*} - a_{1i}^{*})^2 + (b_{0i}^{*} - b_{1i}^{*})^2} \qquad (4.1)$$

where n is the number of the testing data (n = 100), i indicates the i^{th} testing data, L_0^*, a_0^*, b_0^* indicate the CIELAB values calculated from spectral reflectance measured on actual human faces, and L_1^*, a_1^*, b_1^* represent the CIELAB values predicted by each colour characterisation model. The larger the CIELAB colour-difference value, the lower accuracy of the corresponding characterisation model.

The results of CIELAB colour difference calculated between the measurement and each model prediction are given in Figure 4.12, where (a) shows the results obtained when using JPEG image data as camera digital values, and (b) represents the results based on RAW image data. Error bars were calculated using the standard error of the mean for each model.

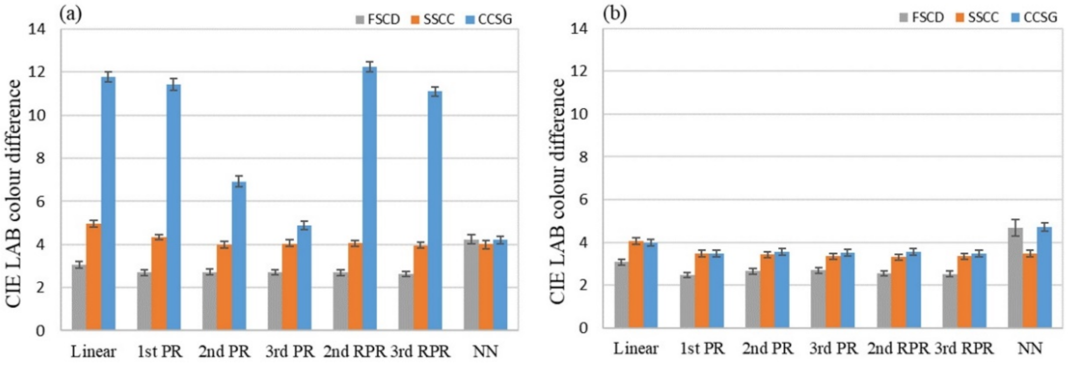

Figure 4.12 Histogram of the average CIELAB colour difference for each prediction model based on RGB (a) and RAW (b) image data.

It can be clearly seen in Figure 4.12 (a) that the colour differences vary greatly for the three different training datasets and the seven different mapping methods. The CCSG training dataset (blue bars) has considerably larger colour-difference values than the other two datasets, except when a neural network was used as the mapping method. In comparison, when the RAW image data were used for skin colour prediction, the variations among different training datasets and mapping methods became much smaller. Noticeably, the CCSG chart produced very similar CIELAB colour-difference values to the other two training datasets, as shown in Figure 4.12 (b), which indicates that the training dataset has little effect on predictive accuracy when using RAW images as camera digital signals. In addition, when the FSCD training dataset was used, in most cases it gave the smallest colour difference for both image formats except for the neural network model (NN).

Tables 4.5 and 4.6 list the average and maximum CIELAB colour-difference values of each colour characterisation model for RGB and RAW image data, respectively. With RGB values as camera digital signals, the 3rd RPR mapping method predicted the smallest colour differences for the FSCD and SSCC datasets, 2.63 ΔE_{ab}^{*} and 3.96 ΔE_{ab}^{*}, respectively, followed by the 1st PR (2.69 ΔE_{ab}^{*}) and 2nd PR method (3.97 ΔE_{ab}^{*}). For the CCSG training dataset, the smallest colour difference was achieved by the NN technique with the value of 4.21 ΔE_{ab}^{*}, followed by the 3rd PR method (4.87 ΔE_{ab}^{*}).

Table 4.5 The average CIELAB colour differences based on RGB and RAW image data (the smallest value for each dataset is shown in bold).

	Training	Linear	1st PR	2nd PR	3rd PR	2nd RPR	3rd RPR	NN
RGB	FSCD	3.06	2.69	2.72	2.71	2.69	**2.63**	4.23
	SSCC	4.97	4.34	3.97	4.04	4.06	**3.96**	4.01
	CCSG	11.76	11.43	6.93	4.87	12.25	11.10	**4.21**
RAW	FSCD	3.08	**2.47**	2.65	2.70	2.55	2.53	4.68
	SSCC	4.06	3.48	3.43	3.35	**3.32**	3.35	3.48
	CCSG	3.98	3.48	3.56	3.51	3.54	**3.47**	4.73

Table 4.6 The maximum CIELAB colour differences based on RGB and RAW image data (the smallest value for each dataset is shown in bold).

	Training	Linear	1st PR	2nd PR	3rd PR	2nd RPR	3rd RPR	NN
RGB	FSCD	9.53	6.51	6.26	6.05	8.10	**5.96**	16.62
	SSCC	8.35	7.52	8.68	8.78	7.80	**7.36**	8.55
	CCSG	17.00	17.16	14.63	**9.17**	17.73	15.97	14.69
RAW	FSCD	7.78	**5.75**	8.21	7.75	6.46	6.32	18.63
	SSCC	10.68	6.84	6.94	**6.75**	7.00	6.94	7.06
	CCSG	8.50	**7.69**	8.07	7.74	8.19	7.76	8.79

For the average results based on RAW image data (Table 4.5), the 1st PR, 2nd RPR and 3rd RPR methods predicted the smallest colour-difference value for the FSCD, SSCC and CCSG datasets, respectively. The colour differences were significantly reduced to less than 4 ΔE_{ab}^{*} for the CCSG dataset, compared with the results based on RGB images. In addition, it can be observed in Table 4.6 that the colour characterisation models achieving the smallest maximum colour-difference value (bold numbers) does not always correspond to the average colour difference results, which suggests that more measures need to be considered to better evaluate the performance of colour characterisation model on image measurement for human facial skin colour.

4.4.3 Facial Contrast

Skin colour of human face is non-uniform and unevenly distributed, it provides essential information of an individual such as youth and health. In this study, the facial colour contrast amongst the five facial locations is introduced and used to present the overall colour variation of the face, and the differences between each two facial locations were calculated in each colour component, CIELAB lightness L^{*}, redness $+a^{*}$ and yellowness $+b^{*}$. Therefore, a total of ten differences were calculated for facial contrast, as shown in Table 4.7.

Table 4.7 The ten differences between each two different facial locations.

	FH	CBR	CBL	NT	CH
FH					
CBR	Δ				
CBL	Δ	Δ			
NT	Δ	Δ	Δ		
CH	Δ	Δ	Δ	Δ	

In order to evaluate the degree of preservation of facial colour contrast in the images predicted using different colour characterisation models, the Pearson Correlation Coefficient was used to quantify the relationship between the facial colour contrast of the objective measurements of an actual human face and those estimated from the corresponding facial image by using colour characterisation models. The larger the Pearson $r$value, the better the preservation of facial contrast of the prediction model.

The results of facial colour contrast in each colour attribute (lightness, redness and yellowness) are shown in Figure 4.13, where (a) and (b) show the results from RGB and RAW image data, respectively. Regarding facial contrast for lightness, the FSCD dataset gives the best predictions, with Pearson r values greater than those for the SSCC and CCSG datasets. For the facial contrast of redness and yellowness, different prediction models gave similar results, except the NN model which gave poor performance for FSCD dataset.

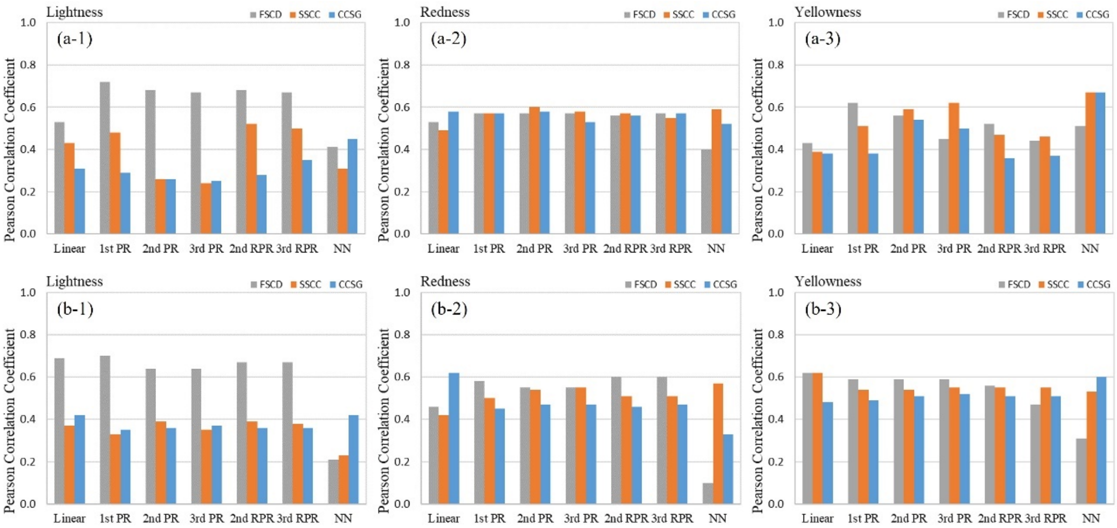

Figure 4.13 Histogram of facial colour contrast PCC in lightness, redness and yellowness based on RGB (a) and RAW (b) image data.

To compare the effect of different training datasets and mapping methods on the prediction of facial colour contrast, the Pearson r values of the three attributes were averaged and the results are given in Table 4.8. From the results based on RGB image data, the 1st PR method gives the largest r value of 0.64, based on the FSCD training dataset. For the SSCC training dataset, the 1st PR, 2nd RPR and NN methods have the same Pearson r values of 0.52. The model based on a neural network performed better for the CCSG dataset with the Pearson r value of 0.55. In comparison, the worse correlation achieved for the FSCD and SSCC training dataset is 0.44 by using the NN method and the linear transformation, respectively. For the CCSG dataset, the 2nd RPR method gave a worst performance with the Pearson r value of 0.40.

For the results based on RAW images, the 1st PR method achieved the largest Pearson r value, 0.62, based on the FSCD dataset. For the SSCC and CCSG datasets the best performance was achieved using the 2nd PR method and the linear transformation, respectively. The neural network model gave the worst predictive results when the FSCD dataset was used as the training data, with a PCC value of only 0.21, which indicates that it is not recommended to apply a neural network with facial skin colour data to determine a colour characterisation model. In addition, the results based on

RAW image data are generally better than those of RGB image data for preserving facial colour contrast.

Table 4.8 The averaged Pearson r values for each prediction model based on RGB and RAW images.

	Training	Linear	1st PR	2nd PR	3rd PR	2nd RPR	3rd RPR	NN
RGB	FSCD	0.50	**0.64**	0.60	0.56	0.59	0.56	0.44
	SSCC	0.44	**0.52**	0.48	0.48	**0.52**	0.50	**0.52**
	CCSG	0.42	0.41	0.46	0.43	0.40	0.43	**0.55**
RAW	FSCD	0.59	**0.62**	0.59	0.60	0.61	0.58	0.21
	SSCC	0.47	0.46	**0.49**	0.48	0.48	0.48	0.44
	CCSG	**0.51**	0.43	0.45	0.45	0.44	0.44	0.45

4.4.4 Skin Colour Boundary

The above two methods to validate the predictive accuracy were limitedly based on the five specific facial locations, for 3D colour image reproduction it is crucial to ensure good colour prediction of the whole skin area, which is also desired for the image-based measurements in cosmetics and medical applications. Therefore, a skin colour gamut in terms of CIELAB values was introduced to verify the colour distributions of the skin-related pixels in the facial images predicted by each model.

Considering the colour distributions of the skin colour data collected in the present study (Figure 4.11) and the skin colour database developed for four ethnic groups (Caucasian, Chinese, Kurdish, Thai) by Xiao et al. (2017), a general skin colour gamut, with the lightness L^*ranging from 40 to 75, the a^* value from 0 to 30 and the b^* value from 5 to 35, was defined to validate the colour characterisation models. Given that the aim was to compare the performance of the 42 colour characterisation models rather than deciding the exact skin colour boundary, this gamut was approximately defined in a cuboid shape, and it is expected that the prediction model can convert most of the skin-colour pixels falling within the predefined gamut and the least colours outside the boundary.

To predict skin colours from facial images, the non-skin regions, such as the hair, eyes and mouth, were removed from each image, and the colour of the remaining pixels was estimated by each colour characterisation model converting the extracted RAW/RGB values of each pixel to CIE XYZ tristimulus values. The percentage of the pixel-based colours outside the gamut was calculated for each facial image, and the average result of all the testing images was used to validate the model performance, expressed in Equation (4.2), where m indicates the number of testing facial images (m = 20), N is the number of the skin colour pixels in each facial image, and n is the number of colours predicted to be outside of the predefined colour gamut. The larger the percentage value, the poorer the accuracy of the corresponding colour characterisation model in estimating skin colours.

$$P = \frac{1}{m}\sum_{i=1}^{m}(n/N) \tag{4.2}$$

After applying each colour characterisation model, the percentage of colours outside the predefined skin colour gamut was calculated for each facial image, and the averaged results for the 20 testing images are listed in Table 4.9. It is shown that different colour characterisation models determined using three training datasets and seven mapping methods lead to obvious differences in estimating pixel-based skin colours from RGB images. For instance, the 3rd RPR method predicted 0.11% colours outside the skin colour gamut for the FSCD training dataset, but 12.30% was achieved for the CCSG training dataset. The minimum percentage value achieved for the FSCD training dataset was 0.07% using the 1st PR method. For both SSCC and CCSG training dataset, the linear transformation predicted the least number of colours outside the skin gamut, which are 1.42% and 0.06%, respectively.

Table 4.9 Percentages (%) of non-skin colours based on RGB and RAW image data (the smallest value for each dataset is shown in bold).

Images	Training	Linear	1st PR	2nd PR	3rd PR	2nd RPR	3rd RPR	NN
RGB	FSCD	2.86	**0.07**	0.15	1.40	0.12	0.11	1.05
	SSCC	**1.42**	1.43	3.70	2.27	2.17	1.90	2.74
	CCSG	**0.06**	0.57	6.39	0.76	2.67	12.3	0.47
RAW	FSCD	0.00	**0.00**	0.60	0.84	0.43	0.09	0.95
	SSCC	0.80	1.16	0.86	0.72	0.69	**0.69**	1.03
	CCSG	**0.24**	1.45	0.94	1.38	1.27	1.65	0.87

Based on RAW images, these models predicted fewer colours outside the predefined skin colour gamut, which indicates most skin colours were smoothly estimated. Compared with the SSCC and CCSG datasets, the FSCD dataset applied to the seven mapping methods almost has the smallest percentage of colours beyond the defined skin colour gamut, with the percentage values ranging from 0.00% to 0.95%. The value of 0.00% means that the colour of each pixel in the facial image was predicted within the predefined skin colour gamut. In addition, the largest number (1.65%) achieved for RAW images is given by using the 3rd RPR mapping method and the CCSG dataset, and the same to RGB images with the largest value of 12.3%.

4.4.5 Discussion

4.4.5.1 Factors Affecting the Colour Characterisation Model

Regarding the two image formats in camera colour characterisation, RGB image data result in larger variation in the predictive accuracy of different training datasets and mapping methods, indicating that it is more dependent on the selection of training data and mapping method. In contrast, different models have very similar predicted results for RAW images. This is probably because RGB images have a complex nonlinear power law relationship between digital signal response and light intensity, while RAW images have a linear relationship with light intensity. In addition, it was confirmed that the predictive accuracy of CIELAB colour difference based on RAW images was generally better than RGB images. This agrees with the results reported by Zhang et al (2017) that RAW images would be better than RGB images for predicting spectral reflectance.

The three different training datasets have a significant impact on skin colour prediction, especially for RGB images. Although the CCSG colour chart has been widely used for camera colour characterisation in various industrial applications (Fairchild et al. 2008), it gave the worst predictive accuracy in terms of CIELAB colour difference. The possible reason for this is that there is a very limited number (fourteen) of skin-colour patches in the CCSG chart which is insufficient for predicting skin colours. Consequently, the CCSG chart is not the most suitable training dataset for skin colour estimation based on RGB images. In comparison, the SSCC training dataset provides slightly better performance on predictive accuracy than the CCSG chart, since it covers a wide range of skin tones. The FSCD training dataset has the best performance in predicting skin colours, showing that real skin colour data is to be preferred as the training dataset to achieve more accurate colour prediction, specifically for quantitative image analysis of wide facial skin area.

In terms of mapping methods, it was previously reported by Li et al. (2003) that a higher order polynomial model performs better than a lower order model for higher predictive accuracy of camera colour characterisation. The similar results were found only when CCSG training dataset was used based on RGB images. This is not surprising because most studies were conducted based on the ColorChecker chart instead of specific colour chart for camera colour characterisation, and few studies focus on the investigation of different methods for skin colour prediction.

Although the linear transformation has larger predicted errors in terms of CIELAB colour difference, most colours in the facial images were predicted within the skin colour gamut. In comparison, smaller colour differences were achieved by using some methods, but it is possible to cause overfitting of prediction so that the skin colour pixels in facial images were predicted outside the skin colour gamut. In general, the 1st PR method has good performance on predictive accuracy in terms of the three evaluation measures.

In addition, the difference between the results of 2nd, 3rd RPR and that of 2nd, 3rd PR methods is not obvious since the root-polynomial regression is a simple (low complexity) extension of polynomial regression (Finlayson et al 2015). Figure 4.14 shows an example of skin colour distributions in a^*b^* plane with the averaged CIELAB values predicted using the seven different mathematical methods and the FSCD training dataset, where the red squares indicate the predefined skin colour gamut in a^*b^* plane. Although all methods gave similar averaged CIELAB values, there is large variation in the colour scatters predicted by the 3rd PR and NN mapping methods, resulting in many predicted colours outside the skin colour gamut. It is suggested that the mapping method with complex extensions is not suitable for predicting pixel-based skin colours, since the complex mapping method may have an overfitting problem for the colours near to the gamut boundary. The neural network gave stable performance in terms of CIELAB colour difference for different training datasets and two image formats, but the results of predicting pixel-based colours are not satisfactory. This is probably because the number of samples in the training dataset is insufficient for predicting the colour of each pixel in the image.

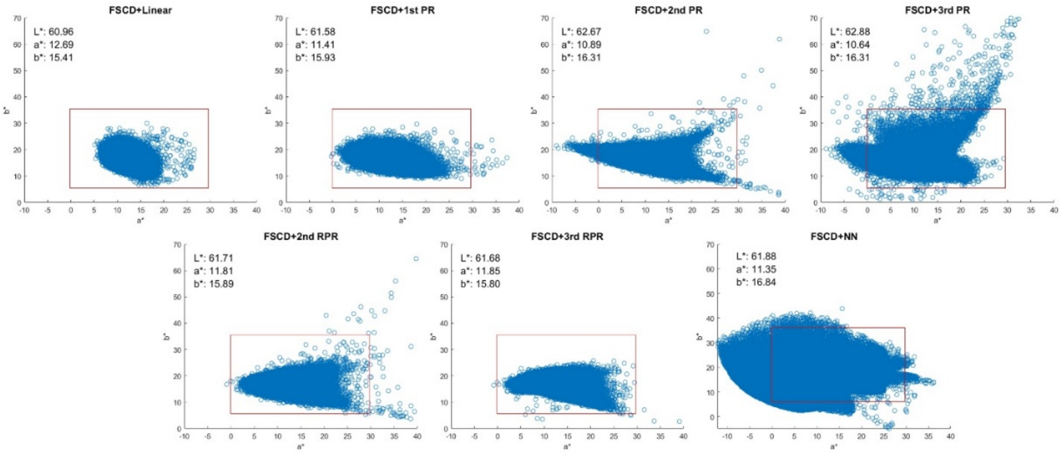

Figure 4.14 An example of colour distributions with the averaged CIELAB values predicted using the seven mapping methods and the FSCD training dataset (the red squares indicate the predefined skin colour gamut in a^*b^* plane).

4.4.5.2 Evaluation Measures

The colour difference between the measured and predicted data is a simple and conventional metric to quantify the predictive accuracy, and most studies rely on this approach to develop a colour characterisation model. However, it was found in this study that colour difference is not enough for the comprehensive evaluation of colour characterisation, especially for image-based colour analysis. For instance, the colour difference predicted using the 1st PR and 3rd PR mapping methods from RGB images was 2.69 and 2.71 ΔE_{ab}^*, respectively, which are similar in value, but there were separately 0.07% and 1.40% predicted colours outside the skin colour gamut. In such a case, the 1st PR method is recommended to convert image data to CIE colour coordinates. Moreover, the colour difference is dependent on the absolute difference of testing points between the ground truth (instrument measurements) and the predictions, regardless of the characteristics of facial skin such as its colour heterogeneity. In this study, two additional measures are proposed, the facial colour contrast which is concerned with the relative relationship between five different facial positions, and the skin colour gamut which is predetermined to validate all pixel-based skin colours.

To achieve accurate image-based measurement for skin colour, it is expected that the facial colour contrast predicted from the facial image is well preserved with that of the actual human face. Regarding the results of facial colour contrast, different models chieved similar Pearson r values less than 0.65. This is probably because of: (i) the colour characterisation model for predicting skin colours, (ii) the method for quantifying facial colour contrast. It requires further investigation on quantifying facial colour contrast, which is an important factor for achieving faithful skin colour reproduction of the human face.

The introduction of the proposed skin colour gamut allows to validate all the pixel-based skin colours predicted from the whole facial skin area, rather than focusing on the limited five facial locations. As shown in Figure 4.14, there is an evident difference between the skin colour distributions in a^*b^*plane estimated using different colour characterisation models, although the averaged CIELAB values were similar (1.5 ΔE^*_{ab}). This indicated that the average colour-difference values are not adequate to objectively quantify the predictive accuracy of human skin colour, especially for wide facial skin area. In addition, although it was confirmed that the skin colour gamut is an effective measure to evaluate the prediction accuracy of the overall detail colours, a cubic gamut in orthogonal CIELAB colour space is simply defined from L^*, a^*, b^* three dimensions. It is recognised that an ellipsoid may better represent skin colour distributions and thus the specification of the boundary of the skin colour gamut should be further investigated.

4.4.5.3 Recommendation

To develop an image-based measurement system for facial skin colour, three components are indispensable: the digital imaging system for human faces, colour characterisation for camera, and the validation of the colour characterisation model. In the digital imaging system, it is necessary to provide diffuse illumination on the human face to accurately estimate skin colour from the captured image, and a linear polariser filter was equipped to the light source and the camera lens to reduce the specular light in the captured facial images.

Regarding the determination of the colour characterisation model, it is necessary to carefully select the training dataset and the mapping method. In general, the skin-colour related colour chart is recommended instead of ColorChecker chart as the training dataset for higher predictive accuracy in most cases, and the skin colour data collected from human faces is preferred to perform image-based measurement for facial skin colour. Moreover, the RAW image format has more stable performance as camera digital signals than the RGB images. As for the mapping method, the 1st polynomial regression is suggested for predicting colours in both specific facial positions and wide facial skin area. When mainly focusing on the colour at specific facial positions, the 3rd PR and 3rd RPR methods also have good performance.

In addition, there is no doubt that colour difference is a simple way to quantify predictive accuracy, but it only focuses on the absolute accuracy of individual facial locations. More aspects should be considered to validate the predictive performance of the model. The two newly introduced measures, facial colour contrast representing the relative relationship amongst five different facial locations and skin colour gamut for validating all pixel-based skin colours, play a role in the validation of a prediction model.

4.5 A Case Study on Skin Colour Heterogeneity under Different Illuminations

4.5.1 Introduction

Skin colour heterogeneity is an indicator of colour spatial distributions in a given facial area, and it influences the overall skin colour appearance of human skin. The colour heterogeneity on human faces is affected by some factors such as climatic conditions, ethnicity, age, etc. (De Rigal et al. 2010, Kukuchi et al. 2015). In addition, the light source as one of components producing colours can significantly affect the colour appearance of human skin. Therefore, it is desired to quantify skin colour heterogeneity under different lightings and investigate how the illumination affects the perception of skin colour.

Melgosa et al. (2018) conducted a study to investigate how facial contrast was affected by different white light-emitting diode (LED) sources and CIE recommended traditional illuminants. It was found that both the body area differences and the discrepancies of colour differences between Caucasian and Oriental subjects were small for the 18 illuminants tested. Chauhan et al. (2019) investigated just noticeable colour difference of facial images under different illuminations, based on skin colour patches representing Caucasian and Chinese skin types. They concluded that facial images under TL84 (CCT = 3900 K) have a larger discrimination threshold than the D65 illumination (CCT = 6100 K).

Considering that conventional colour measurement instruments often fail to measure skin colours of a wide facial area due to their limited measurement aperture, an image-based approach is required to analyse skin colour heterogeneity on human faces. Based on the specific digital imaging system developed for capturing facial images, this case study was conducted to objectively quantity skin colour heterogeneity under various illuminations with different CCTs including the simulated D65 daylight.

4.5.2 Illuminations and Image Capture

Based on the stable and well-controlled LED lighting system in the digital imaging system (Figure 4.1), six illuminations with different CCTs of 2850 K, 3500 K, 5000 K, 5500 K, 6500 K and 9000 K were created and saved in the LEDNavigator software, respectively. A Konica Minolta CS2000 tele-spectroradiometer was used to measure each of the six lightings by targeting at a white tale illuminated in the position of the human face. Table 4.10 lists the measured parameters of each illumination, and Figure 4.15 plots the relative SPDs of the six illuminations used for image capture. Note that the illumination of 6500 K is the same to the one used for camera colour characterisation in previous sections.

Table 4.10 Parameters of each illumination measured using the CS2000 tele-spectroradiometer.

	2850 K	3500 K	5000 K	5500 K	6500 K	9000 K
CCT (K)	2848	3516	5014	5514	6544	9033
Ra	91	98	96	97	96	96
lux(cd/m^2)	112.62	117.88	118.3	123.48	127.45	119.65
Duv	0.003	0.0035	0.0059	0.0066	0.0064	0.0058

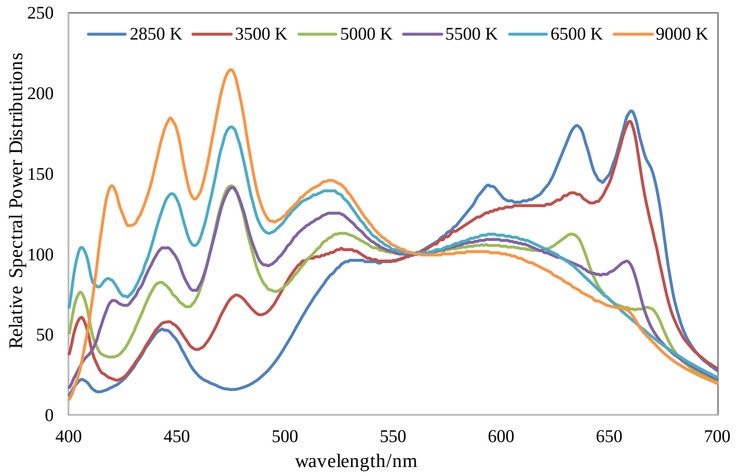

Figure 4.15 The relative SPDs of the six illuminations produced in the digital imaging system.

To investigate the effect of different illuminations on skin colour heterogeneity, the developed digital imaging system described in Section 4.1 was used to capture images of human faces under the six illuminations with different CCTs. The camera settings were manually adjusted to ISO 640, aperture size f/5.6, shutter speed 1/8 second, and the white balance was customised as the CCT value of each illumination used for image capture, i.e., when taking image capture under the illumination of 2850 K, the white balance was customised as 2850 K, and it was changed to 9000 K when using the illumination of 9000 K. The process of facial image acquisition is the same as that described in the Section 4.1.4. Six image captures were taken for each face under the six illuminations. The RAW images without post-processing were collected and used for image analysis on skin colour heterogeneity.

In this case study, 25 human participants from different ethnic groups (5 Indonesian, 5 Caucasian, 5 Chinese, 5 Mexican and 5 African) were involved to collect facial images under the six different illuminations, including 9 males and 16 females. All the participants were in the age group of 20-30. A total of 150 facial images were collected using the digital imaging system.

4.5.3 Methodology

Camera colour characterisation was performed under each light source to determine the model transforming from the RAW RGB values to CIE XYZ tristimulus values for each facial image. In light of the results achieved in Section 4.4, the 95 colour samples with different skin tones in the Spectromatch silicon skin colour chart were used as the training samples and captured under each illumination using the digital camera with the specific settings. The RAW RGB values of each colour sample were extracted from the captured images using the open source raw-files converter *dcraw* in MATLAB. A Konica Minolta CM-2600d spectrophotometer with a 3 mm aperture size and SCI measurement mode was used to measure the spectral reflectance of each sample, and the CIE XYZ tristimulus values were calculated with the CIE 1931 standard observer and the measured SPD of each illumination (Figure 4.15). In addition, the third-order polynomial regression was applied with the least-square fitting method to determine the colour characterisation model under each illumination to convert RAW RGB values to CIE XYZ values.

In this study, the CIECAM16-UCS described in Section 2.1.6.2 was used to quantify the colour difference of facial skin under different light sources. The CIE XYZ tristimulus values under different illuminations were converted to CIECAM16-UCS colour appearance attributes J', a' and b', using the Equations 2.22-2.37. Compared to CIELAB colour space, the CIECAM16-UCS has a better model of chromatic adaptation, and it transforms skin colours under a specific illumination to the equivalent under an equal-energy white condition (illuminant E). The CIECAM16-UCS colour difference formula is expressed in Equations 2.38-2.39, with a power function corrected.

The mean colour difference from the mean ($MCDM$) with CAM16-UCS colour difference was used to quantify skin colour heterogeneity under different illuminations. The larger the $MCDM$ values, the greater the skin colour heterogeneity. For the local colour heterogeneity, it is defined as the average colour difference between each pixel and the average of the facial area of 100 × 100 pixels ($n = 10000$ in $MCDM$). For the facial position difference, it is defined as the average colour difference between each facial location (50 × 50 pixels) and the average of the 5 facial locations ($n = 5$ in $MCDM$).

4.5.4 Results and Discussion

4.5.4.1 Colour Characterisation Accuracy

The skin colour data collected from 25 human participants were used to quantify the accuracy of the colour characterisation model. For the facial images captured under each illumination, the RGB values of each pixel in the facial area of 50 × 50 pixels were averaged and converted to the corresponding CIE XYZ values using the camera characterisation model. The colour difference between the CIE XYZ values calculated from the spectrophotometer measurement and the model prediction was calculated using the CAM16-UCS colour difference formula.

The average results for the six different illuminations are given in Table 4.11, where the predictive errors achieved using the colour characterisation models were between 2.13 to 2.39 units. These values indicate that the generated colour characterisation models have agreeable and similar performance for different illuminations on predicting CIE colorimetric values of facial skin, based on the RAW images captured using the digital imaging system.

Table 4.11 Prediction accuracy in terms of CIECAM16-UCS colour difference of different colour characterisation models.

	2850 K	3500 K	5000 K	5500 K	6500 K	9000 K
$\Delta E_{CAM16-UCS}$	2.39	2.30	2.19	2.18	2.13	2.18

4.5.4.2 Local Colour Heterogeneity

Based on the colour characterisation model developed for each light source, the RAW RGB values of each pixel in the facial area of 100 × 100 pixels were converted to CIE XYZ values and then transformed to CAM16-UCS colour space. The $MCDM$ with the CIECAM16-UCS colour difference formula was used to quantify skin colour heterogeneity in each facial area under the six illuminations with different CCTs. The average results of the five facial areas under each illumination are given in Table 4.12, where the bold and underlined numbers respectively indicate the maximum and minimum colour-difference value under the six illuminations. It can be seen that the largest skin colour heterogeneity of the subjects from different ethnicities always occurs under the illumination with a CCT of 2850 K, and the smallest colour heterogeneity was produced under the illuminations of 5000 K.

Table 4.12 The average $MCDM$ values of the five facial areas under six illuminations.

	2850 K	3500 K	5000 K	5500 K	6500 K	9000 K
Indonesian	**2.46**	2.17	1.82	1.84	1.83	1.88
Caucasian	**2.68**	2.38	2.12	2.12	2.12	2.12
Chinese	**2.54**	2.26	1.90	1.99	1.93	1.98
Mexican	**2.69**	2.19	1.82	1.84	1.87	1.90
African	**3.55**	3.11	2.53	2.56	2.67	2.56

Figure 4.16 illustrates the histogram of skin colour heterogeneity of the human participants from five ethnicities, and the dashed line indicates the trend under the six illuminations. It can be seed that the $MCDM$ values decreased with an increase in the CCT of the light sources of 2850 K to 5000 K. Under the light sources with the CCT between 5000 K to 9000 K, there were slight changes in skin colour heterogeneity. The results suggested that larger skin colour heterogeneity exists under the light sources with lower CCT, and when the CCT of the light source is higher than 5000 K, the colour heterogeneity differs little with the change of CCT.

Considering that skin colour is reddish as well as yellowish and the light sources with lower CCT appears warmer (reddish), the skin colour variations are possibly more obvious under the light source with similar colour appearance. In order to further investigate the effect of the CCT of light source on local skin colour heterogeneity, the chin area of five females from different ethnicities was taken as an example. Figure 4.17 presents the skin colour distributions of the 10000 pixels in $a'b'$ and $J'M'$ plane with the boundaries illustrated, where the red, green, blue, cyan, magenta and yellow colours indicate the results under the light sources of 2850 K, 3500 K, 5000 K, 5500 K, 6500 K and 9000 K, respectively.

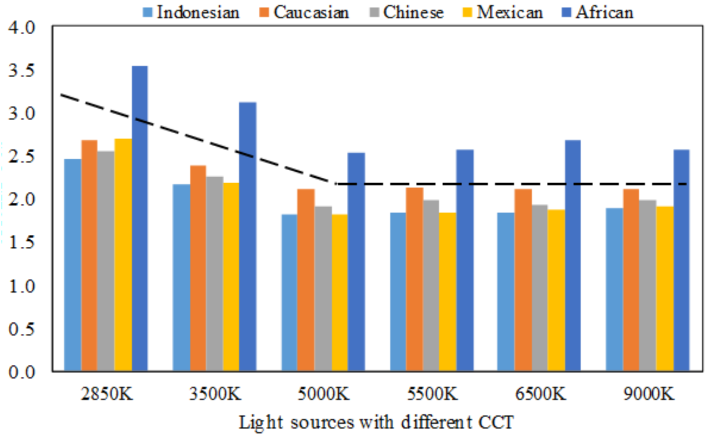

Figure 4.16 Skin colour heterogeneity in CIELAB units under six light sources.

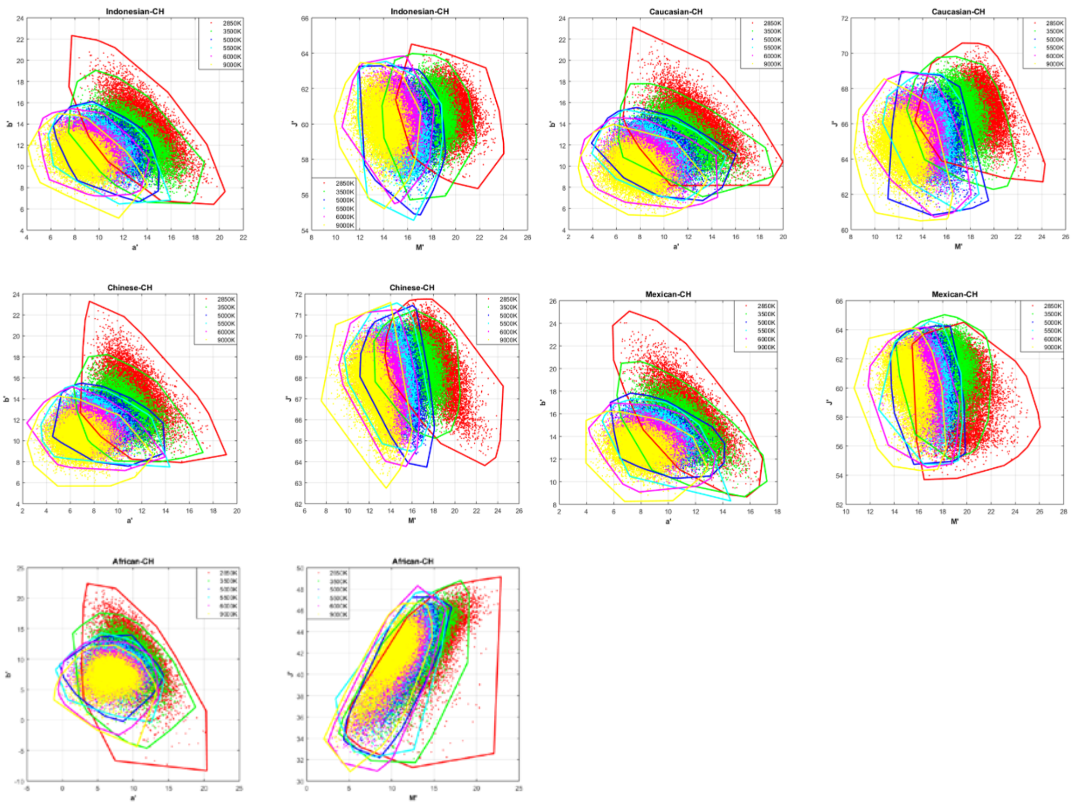

Figure 4.17 Skin colour distributions and the boundary in $a'b'$ and $J'M'$ plane for the chin area.

From the colour distributions of the chin area in $a'b'$ plane in Figure 4.17, it can be clearly seen that the skin colour boundary under the illumination of 2850 K (the red line) is the largest among the six light sources, followed by the boundary under the 3500 K illumination (the green line). In contrast, the skin colour boundaries under the other four light sources are relatively smaller. The results are similar to the $MCDM$ values given in Table 4.12, indicating that a light source with lower colour temperature results in larger skin colour variation.

In addition, with the increasing CCT of the light source, the colour distributions of the chin area shift to the $-a'$ and $-b'$ axis, which means that the colours become less reddish and less yellowish. This is affected by the change of colour temperature of the illumination. From the skin colour distributions in $J'M'$ plane, the variation in lightness (J') scale remains similar and close under the six different light sources, but the range and variation of the colourfulness (M') scale decreased with an increasing CCT of the illumination. Additionally, the skin colours of the chin area are discrete, this is possibly because of the existence of skin texture, pores or fine hair in the facial skin area.

Table 4.13 The skin colour gamut sizes in $a'b'$ and $J'M'$ plane (volumes in $J'a'b'$ colour space) under each illumination.

	2850 K	3500 K	5000 K	5500 K	6500 K	9000 K
Indonesian - $a'b'$	**112**	88	56	63	56	59
Caucasian - $a'b'$	**126**	88	69	63	74	67
Chinese - $a'b'$	**112**	73	54	59	59	65
Mexican - $a'b'$	**97**	77	45	50	53	53
African - $a'b'$	**372**	253	135	151	163	159
Indonesian - $J'M'$	**52**	49	46	49	43	41
Caucasian - $J'M'$	**57**	49	52	41	49	49
Chinese - $J'M'$	**55**	37	35	39	39	48
Mexican - $J'M''$	**86**	60	48	50	53	56
African - $J'M'$	**228**	154	96	122	121	101
Indonesian - $J'a'b'$	**490**	425	295	325	272	275
Caucasian - $J'a'b'$	**536**	418	353	285	342	310
Chinese - $J'a'b'$	**444**	270	212	226	244	294
Mexican - $J'a'b'$	**729**	467	281	317	314	322
African - $J'a'b'$	**1982**	1298	659	728	786	766

Based on the algorithm of convex hull in MATLAB, the sizes of the colour boundary of each facial area in $a'b'$ and $J'M'$ plane and $J'a'b'$ colour space were computed separately for each light source, and the average results are given in Table 4.13. It can be seen that the area and volume of skin colour distributions under 2850 K illumination is the largest, followed by the results achieved under the light of 3500 K. In addition, the area of colour distributions in $a'b'$ plane is larger than that in $J'M'$ plane by a factor of 1.5-2.0 under each light sources. It is indicated that the lightness changes less than other chromatic attributes as the CCT of the light source changes. Furthermore, it can be seen from Table 4.13 that the African faces have more discrete skin colour distributions, followed by the Mexican faces. This is caused by the ethnicity and possibly affected by living environments, diet habits and other biophysical properties of the different ethnic groups (Richards et al. 2003).

4.5.4.3 Facial Position Difference

In addition to the local skin colour heterogeneity, the facial position differences were investigated under different light sources. Table 4.14 gives the average results of the facial position differences for each ethnic group under the six illuminations with different CCTs. It is shown that the facial position differences for each ethnic group vary slightly under the six light sources, indicating that the illuminations with different CCTs have little effect on the differences between different facial positions. Compared to the results of the local skin colour heterogeneity, the facial position differences are smaller, this is probably because the skin colour variation was averaged and diminished. In addition, it is normally desired for human beings to have smooth and even complexion to improve the visual perception of health and attractiveness, and it was reported that the difference between skin area and non-skin area is preferred to enhance facial contrast (Melgosa et al. 2018).

Overall, based on the developed digital imaging system for capturing facial images, a case study on skin colour heterogeneity under six illuminations with different CCTs was conducted, and the results were quantified by calculating $MCDM$ values in terms of CAM16-UCS colour differences. It was found that the local skin colour heterogeneity was the largest under the illumination of 2850 K, and it decreased with an increase in CCT. There were slight changes in local skin colour heterogeneity under the light sources with a CCT of 5000 K to 9000 K. Regarding facial position differences, the effect of different illuminations is not obvious. In addition, different ethnicities have a significant effect on skin colour variations including local skin colour heterogeneity and facial position differences, which is greater than the influence caused by different illuminations.

Table 4.14 The average $MCDM$ values of the five facial areas under six illuminations.

	2850 K	3500 K	5000 K	5500 K	6500 K	9000 K
Indonesian	2.52	2.54	2.59	2.60	2.60	2.61
Caucasian	1.72	1.69	1.73	1.71	1.70	1.71
Chinese	1.86	1.82	1.83	1.83	1.81	1.83
Mexican	1.85	1.85	1.88	1.88	1.88	1.90
African	3.53	3.52	3.60	3.60	3.61	3.65

4.6 Colour Characterisation for the 3D Imaging System

4.6.1 Introduction

The colour information of a human face is captured and saved in a 2D bitmap image using the 3dMDface system. The colour characterisation process performed for the developed digital imaging system was applied to the 3D imaging system. Considering that certain glares were found in some facial areas such as the forehead and cheeks in the bitmap image, it is not appropriate to use the skin colour data of human faces collected in this system as the training dataset to determine the camera colour characterisation model. Instead, a specific skin colour chart was applied to transform 3D camera RGB values to CIE colorimetric values.

It is notable that the ethnicity has an observable effect on skin colour heterogeneity, and it was reported by Xiao et al. (2017) that skin colour differences between ethnicities are significant especially in the yellowness dimension. Therefore, it is sensible to use different skin colour charts for different ethnic groups for accurate skin colour reproduction. In this section, a specific colour chart developed for Chinese skin tones was adopted to perform colour characterisation for the 3dMDface system based on the captured bitmap image, and the accuracy of the developed colour characterisation model was validated using skin colours of Chinese participants' actual faces, rather than using uniform skin colour patches as previous studies (Xiao et al. 2014, Sohaib et al. 2018).

4.6.2 Colour Characterisation Process

The skin colour chart, as shown in Figure 4.18 (left), was developed based on an existing skin colour database collected by Xiao et al. (2017). It consists of 216 colour patches including a series of grey scales, 14 skin colour patches from the ColorChecker digital SG chart, 18 natural colour patches with high chroma and other skin colour patches generated from the skin colour database. Both boundary colours and cluster centroid colours of the skin colour database were included in this chart. A Konica Minolta CM-700d spectrophotometer with an aperture of SAV 3 mm and SCI measurement mode was used to measure each colour patch of the skin colour chart. Figure 4.18 (right) presents the colour distributions of the 216 patches in CIE a^*b^* and L^*C^* plane. It can be observed that this skin colour gamut covers the colour distributions of the facial skin colour data collected in the present study (Figure 4.11).

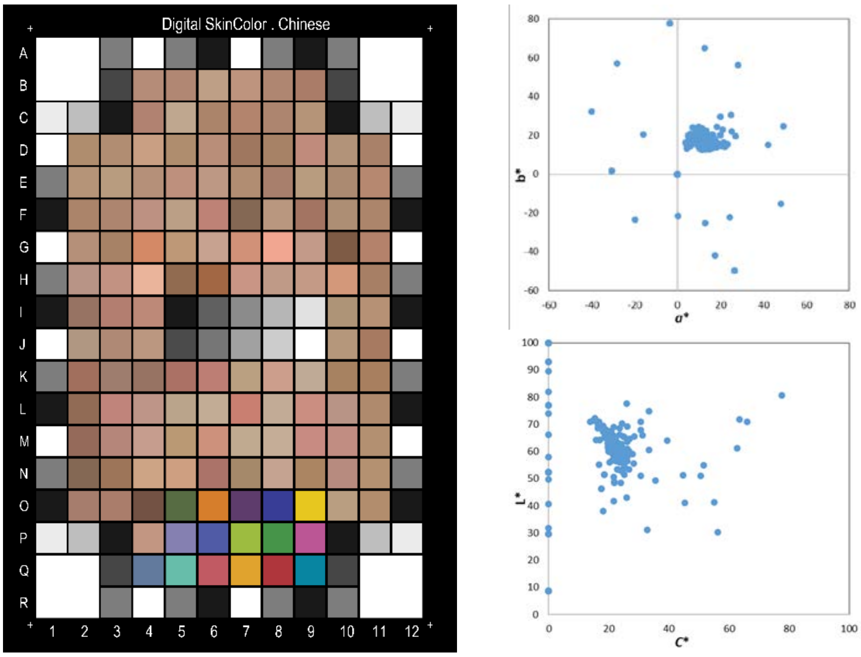

Figure 4.18 The skin colour chart developed for Chinese population (left) and the colour distributions in a^*b^* and L^*C^* plane.

The skin colour chart was placed in the position of the calibration plate and captured using the 3dMDface system after a successful calibration. A bitmap image was created using the 3D imaging system, consisting of three colour images from three directions, as shown in Figure 4.19 (left). The front-facing image in the bitmap captured from the central camera unit was used to extract RGB values of each colour patch in MATLAB.

Based on the RGB values of the 216 colour patches and the corresponding CIE XYZ tristimulus values measured using a spectrophotometer, polynomial regressions with 1-3 orders were respectively applied with the least-square fitting method to determine a colour characterisation model for the 3D imaging system. Additionally, the ColorChecker digital SG chart was also captured using the same procedure of the 3dMDface system, and a comparison was made on the predictive accuracy of the two colour charts transforming 3D camera RGB values to CIE XYZ values.

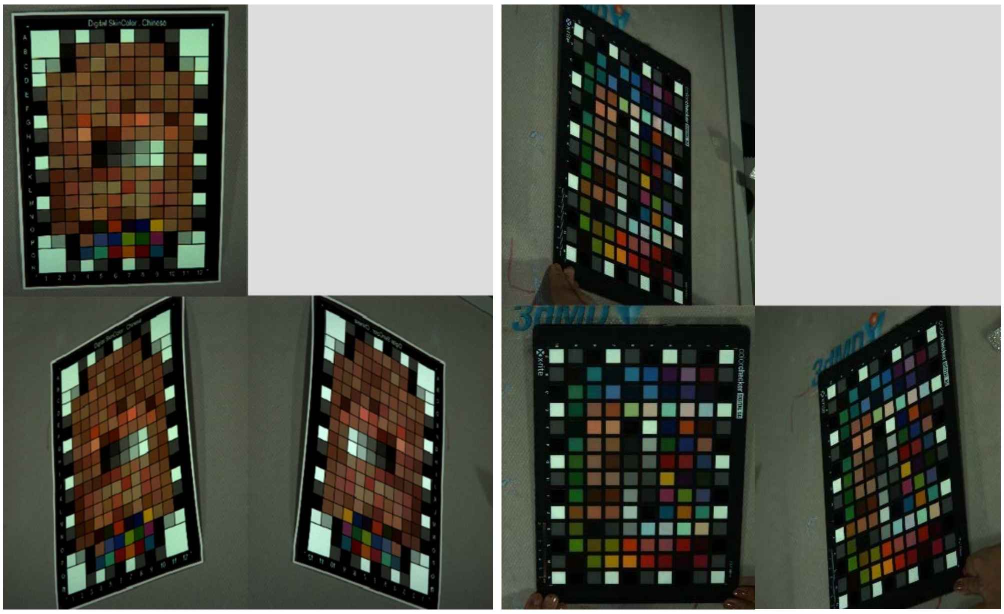

Figure 4.19 The bitmaps of the skin colour chart (left) and the ColorChecker digital SG chart (right) captured using the 3dMDface system.

4.6.3 Validation and Accuracy

Rather than using uniform colour patches, actual human skin colours were collected in this study to validate the performance of the colour characterisation model generated for the 3D imaging system. Five Chinese females were invited to participate in the 3D image acquisition which was conducted in a dark room, and the built-in flash in the 3D imaging system was the only illumination for 3D image capture. A calibration procedure was completed before taking facial images using this system. The human subject was asked to sit on a chair placed in a specific position that is the same as the calibration plate. The height of the chair was adjusted so that the human face can be shown simultaneously in the three live view windows. During the 3D image acquisition using the 3dMDface software, the subject was asked to keep still until the capture is finished. It is important to ensure that no undesired image characteristics such as imaging artifacts and blurring appear in the bitmap image, otherwise, a new image capture should be taken.

Figure 4.20 gives an example of the bitmap image captured for a Chinese female using the 3D imaging system. The five facial positions (forehead, right and left cheekbones, nose tip and chin) illustrated in Figure 4.9 were located on the front-facing image in the bitmap, and the corresponding RGB values of each facial position were extracted and averaged in MATLAB. Based on the colour characterisation model developed using the colour chart, the averaged RGB values of each facial position in the bitmap image were converted to CIE XYZ tristimulus values, and the corresponding CIELAB values were calculated with CIE standard illuminant D65. The performance of different colour characterisation models developed using different approaches is quantified by calculating the CIELAB colour differences between the spectrophotometer measurements on the actual human faces and the skin colours predicted from the bitmap using the colour characterisation model.

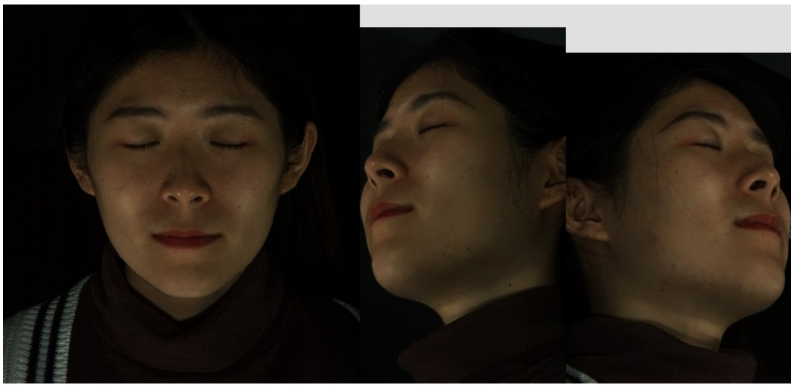

Figure 4.20 An example of the captured bitmap image of a Chinese female.

Tables 4.15 and 4.16 give the average and maximum CIELAB colour differences of 25 human facial skin colour data, respectively, where the rows indicated different training dataset and the columns denote different orders of polynomial regressions. The 3rd order polynomial regression gave a smallest average colour difference (3.84 CIELAB units) for the SG chart, while for the skin colour chart, a CIELAB colour difference of 3.16 was achieved using the 1st polynomial regression. In addition, when the skin colour chart was adopted to perform camera colour characterisation for the 3D imaging system, the colour differences achieved are smaller than the results produced using a ColorChecker SG chart, which shows the advantage of the skin colour chart as training data for accurate skin colour reproduction of the 3D imaging system.

It was found that both the average and maximum colour-difference values decreased when the SG chart and the skin colour chart were combined together as the training data, which are 2.90 and 5.12 CIELAB units, respectively. Considering that the colour characterisation model is to be applied to the whole facial image, the combination of both colour charts and the 2nd polynomial regression were utilised to determine the colour characterisation model for the 3D imaging system. Figure 4.21 shows the new bitmap image of the participant’s face in Figure 4.21 after applying the camera colour characterisation model. It can be clearly seen that the skin colours of the human face are more faithful and realistic than the original image captured using the 3dMDface system.

Additionally, the accuracy of skin colour reproduction without performing any colour characterisation for the 3D imaging system was quantified by calculating the CIELAB colour differences between the captured facial images and the spectrophotometer measurements on the actual human face, and the results acquired are given in Table 4.17. The average colour difference of 5 Chinese female faces was 32.71 CIELAB units, which indicates that the 3D imaging system has a poor ability to reproduce facial skin tones accurately. It can also be recognised from Figure 4.20 that the lightness of the human face in the captured image is much lower, this is probably because of the industrial-grade flash built in the 3dMDface system. Therefore, it is necessary to perform camera colour characterisation for the 3dMDface system to reduce the predictive colour differences. Compare the results before and after applying the camera colour characterisation model, the average colour difference decreased from 32.71 to 2.90 CIELAB units, indicating a significant improvement in accurate skin colour reproduction.

Table 4.15 The average CIELAB colour-difference values testing for different colour characterisation methods.

	1st order	2nd order	3rd order
SG chart	4.48	4.30	**3.84**
Skin Chart	**3.16**	3.34	3.40
SG + SC	3.03	**2.90**	3.20

Table 4.16 The maximum CIELAB colour-difference values testing for different colour characterisation methods.

	1st order	2nd order	3rd order
SG chart	7.12	6.92	**6.63**
Skin Chart	5.23	5.25	**5.19**
SG + SC	5.55	**5.12**	5.28

Table 4.17 The average CIELAB colour-difference values without performing colour characterisation.

	Mean	Minimum	Maximum
ΔE_{ab}^{*}	32.71	**29.98**	37.31

Figure 4.21 The modified bitmap image of a Chinese female after applying the colour characterisation model.

4.7 Summary

In this chapter, colour characterisation of the digital imaging system was performed for image-based measurement of human facial skin, and different methods were investigated for accurate skin colour reproduction. Specifically, a bespoken digital imaging system was developed to collect facial colour images of 144 human participants, and the factors affecting image-based facial skin colour measurement were investigated:

- Two image formats: RGB and RAW,
- Three training datasets: FSCD, CCSG, SSCC,
- Seven mapping methods: the linear transformation, polynomial regressions and root-polynomial regressions with 1-3 orders, neural network.

The predictive accuracy of different camera colour characterisation models was quantified not only using the conventional CIELAB colour-difference formula, but also two newly introduced measures: facial colour contrast and skin colour boundary. Moreover, based on the specific digital imaging system and the developed camera colour characterisation model, facial skin colour variations under six illuminations different with CCTs were investigated, and it was found that larger local skin colour heterogeneity exists under the light source with lower CCT (2850 K).

In addition, the colour characterisation of the 3dMDface system was performed and validated for accurate skin colour reproduction of human faces. Specifically, a colour characterisation model was determined based on a skin colour chart and a ColorChecker SG chart. The facial skin colour data of five Chinese participants were used to evaluate the developed colour characterisation model for the 3D imaging system. Furthermore, the predictive accuracy before and after performing camera colour characterisation was compared. The outcomes are:

- A specific skin colour chart was applied to the colour characterisation of the 3D imaging system, rather than using the conventional colour charts,
- Actual skin colours of human faces instead of uniform skin colour patches were used to validate the predictive accuracy,
- The average colour difference of human facial skin decreased from 32.71 to 2.90 CIELAB units by performing camera colour characterisation, and the maximum colour difference was reduced from 37.31 to 5.12 CIELAB units,
- A specific colour characterisation model with high accuracy was determined for the 3D imaging system and successfully applied to the captured facial images for realistic skin colour reproduction.

Chapter 5

Colour Characterisation for the 3D Printer

Colour characterisation is a fundamental part of colour management. The process of colour characterisation for a 3D printer is to ensure accurate colour reproduction of 3D printed objects by developing a mathematical model that describes how the printer produces colours. Typically, the colour characterisation model is determined to transform between the device-dependent colour space (printer RGB or CMYK), and the device-independent colour space, such as CIELAB. Although the colour characterisation methods developed for 2D printers have been applied to 3D colour printers, currently it still lacks a standard numerical model for accurately predicting the colour of 3D printed objects. To achieve more accurate colour reproduction of a human face, the methods for determining a colour characterisation model of a 3D printer were investigated. Furthermore, a skin colour chart was applied in practical printing process to enable the printer faithfully produces the desired skin tones for a 3D face model.

5.1 Investigation on Colour Characterisation Methods

With the development of machine learning methods, it has become widespread to perform colour characterisation transforming between device-dependent colour space to device-independent colour space. However, few research focuses on the comparison of different colour characterisation methods for a 3D CMYK colour printer. This study was conducted to explore how the conventional polynomial regressions and new machine learning methods affect the colour characterisation results, based on a large dataset consisting of 2016 colour samples.

Specifically, the CMYK combinations of the 2016 samples were regarded as the input vectors, and the spectral reflectance, CIE XYZ and CIELAB were considered as the output, respectively. The third order polynomial regression and the deep neural networks (DNN) with multiple layers were separately applied to determine colour characterisation models converting from the input vectors to the output values. The accuracy of the colour characterisation models determined in different approaches was quantified by calculating CIELAB and CIEDE2000 colour differences under CIE standard illuminant D65.

5.1.1 Dataset

The dataset was generated using a Stratasys J750 3D printer, which consists of 2016 colour samples with each sample represented in CMYK colour space and spectral reflectance data ranged from 400 nm to 700 nm with intervals of 10 nm that were measured using a X-Rite i1PRO3 spectrophotometer. The measured spectral reflectance data were used to calculate the corresponding CIE XYZ and CIELAB values with CIE 1931 standard observer and CIE illuminant D65 using Equations (2.1) and (2.4-2.6). In practical applications, all the required data as CIE recommendations may not be available because the measurement was made at intervals of 10 nm and data at the spectral extremes were omitted (truncation). ASTM (2017) provides tristimulus weighting factors at 10-nm and 20-nm intervals for CIE standard and recommended illuminants and CIE 1931 and 1964 standard observers, which can be used for any degree of truncation by adding the weights at the unmeasured wavelengths to those at the extreme measured wavelengths.

Figure 5.1 illustrates the distributions of the 2016 colour samples in a^*b^* and L^*C^*plane, which refers to the colours and tones that the 3D printer can produce. In addition, the colour distributions generate a colour gamut of the 3D printer, where the colours range from -84.90 to 74.49 for the a^* redness-greenness scale, 5.77 to 93.53 for the L^* lightness, and -48.20 to 113.17 for the b_{10}^* yellowness-blueness dimension. Figure 5.2 plots the spectral characteristics of the four CMYK primaries with 100% density.

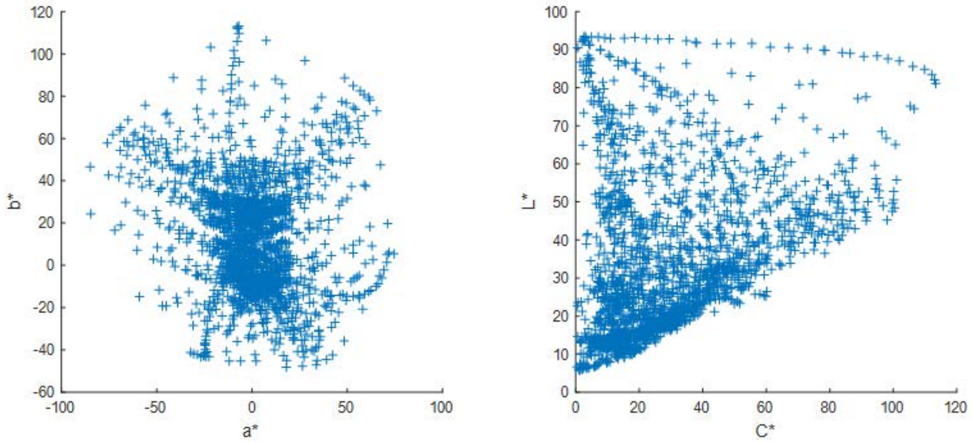

Figure 5.1 Colour distributions of the 2016 samples of the dataset in a^*b^* and L^*C^* plane.

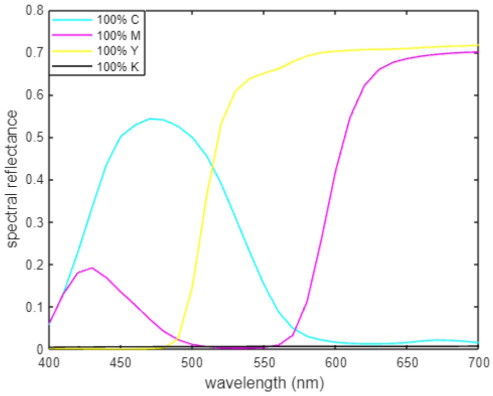

Figure 5.2 Spectral reflectance of the CMYK primaries with 100% density.

5.1.2 Methodology

5.1.2.1 Input and Output Vectors

In order to ensure that the printed colours match well with the target colours, a forward colour characterisation was performed to transform from printer input vectors to the output vectors. The relationship can be expressed in Equation (5.1), where P indicates the input vectors (CMYK combinations), C denotes the output vectors, and M means the colour characterisation model converting the input vectors to the output vectors.

$$C = PM \tag{5.1}$$

Regarding the output vectors, the spectral reflectance data (r), CIE XYZ tristimulus values and CIELAB values were selected as the device-independent colour space, respectively. In addition, the logarithmic-based approach applied to CIE XYZ values was also used to investigate the effect of different output data types on printer colour characterisation.

The use of spectral reflectance data as the output is beneficial for spectral reconstruction from device-dependent colour space, which is critical for practical applications since spectral data contain essential information that cannot be obtained from CIE XYZ and CIELAB values. By applying Principal Component Analysis (PCA), it is possible to reduce the dimension of the spectral data and derive the basis function U_K that are sufficient to describe the spectral reflectance (Shaw et al. 2013, Xiao et al. 2016). Marimont and Wandell (1992) stated that the principal components are usually 5-10 for providing an accurate estimation for natural objects. In the present study, the principal components of the spectral reflectance of the 2016 colour samples were determined as 6 after testing from 1 to 31.

As expressed in Equation (5.2), the coordinate vector β can be achieved from the basis function U_K and the spectral reflectance r, which was regarded as the output after performing PCA on spectral data. The CMYK values were firstly converted to the coordinate vector β, and then the spectral reflectance data was reconstructed with the basis function U_K, using the Equation (5.3). More details in colour transformation using PCA can be found in the study conducted by Xiao et al. (2016).

$$\beta = (U_K)^T r. \tag{5.2}$$

$$r = U_K \beta. \tag{5.3}$$

In totally, five output data types were used for printer colour characterisation:

- CIE XYZ,
- log(XYZ): the logarithm to CIE XYZ,
- CIELAB,
- r: spectral reflectance data,
- PCA(r): principal components of spectral data.

5.1.2.2 Polynomial Regression

Given the number of the training data is n, the 3rd-order polynomial regression was applied to the input CMYK matrix, making it expanded from $n \times 4$ to $n \times 35$ dimensions. The third order was selected due to the complex colour transformation between the subtractive printer CMYK combinations to a device-independent colour space. By performing matrix operations in MATLAB, the colour characterisation model M was determined using the Equation (5.4). A 35×3 matrix was derived for the output vectors of CIE XYZ and CIELAB values which were in $n \times 3$ dimensions. When the spectral data r and PCA(r) were treated as the output values, the corresponding colour characterisation matrix determined was 35×31 and 35×6, respectively.

$$M = CP^{-1} \tag{5.4}$$

5.1.2.3 Deep Neural Networks

The architecture of the deep neural networks used in this study contained multiple hidden layers to distribute different neurons and process the information sequentially layer by layer, as shown in Figure 5.3. The first input layer was the predictor variables CMYK, then followed by four fully connected layers (*Fc*) with a swisher layer (*Sw*) in between, and the final regression layer was the output predictions, such as CIE XYZ, CIELAB, spectral reflectance.

The numbers of the neurons in the four fully connected layers were given in Table 5.1. For the CIEXYZ- and CIELAB-based colour characterisation, the numbers of the neurons in the four fully connected layers were 21-77-21-3, respectively. For the spectra-based colour characterisation, the numbers in the four *Fc* layers were defined as 22-66-33-31 because of the higher dimensions of the spectral data. The parameters were the same for the principal components of spectral data (PCA(r)), except the number in the last layer was 6, which was consistent to the dimensions of the output variables. There is no specific method to determine the number of the neurons in each layer, these numbers were chosen in this study based on literature surveys and a testing procedure.

The network transforming from the input to the output variables were trained in MATLAB with the optimisation method of Adam. Five attempts were made with the maximum epochs number of 2000 and the learning rate of 0.01. Based on the optimal results of the 5 attempts, another neural network was trained to achieve better results, with the maximum epoch number of 4000 and the learning rate of 0.01 for CIELAB predictions and 20000 and 0.001 for spectral estimation, respectively.

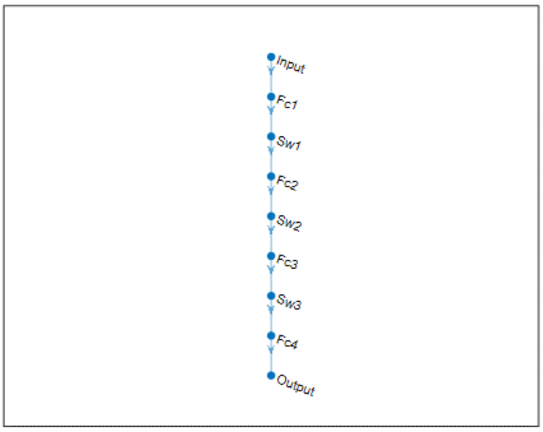

Figure 5.3 The configuration of the deep neural networks implemented (Fc: fully connected layer, Sw: swisher layer).

Table 5.1 The number of the neurons in the four fully connected layers.

	CIE XYZ	Log(XYZ)	CIELAB	r	PCA(r)
Number	21-77-21-3	21-77-21-3	21-77-21-3	22-66-33-31	22-66-33-6

5.1.2.4 Colour Characterisation Process

The process of colour characterisation is illustrated in Figure 5.3. For the dataset consisting of 2016 colour samples, it was divided into a training dataset and a testing dataset. Based on the training dataset consisting of CMYK values and corresponding colour measurement data, the methods of the 3rd polynomial regression and the deep neural networks were separately applied to determine the corresponding colour characterisation model, which was performed in MATLAB. Since there were five types of output variables, a total of ten colour models were generated for the forward colour characterisation of the 3D printer.

Regarding the reverse colour characterisation converting from target colour data to printer controlled CMYK values, the colour accuracy cannot be quantified directly from the estimated and actual CMYK colour values. Therefore, only the results of forward colour characterisation were included in Section 5.1. The process and results of reverse colour characterisation for the 3D printer were presented in Section 5.2.

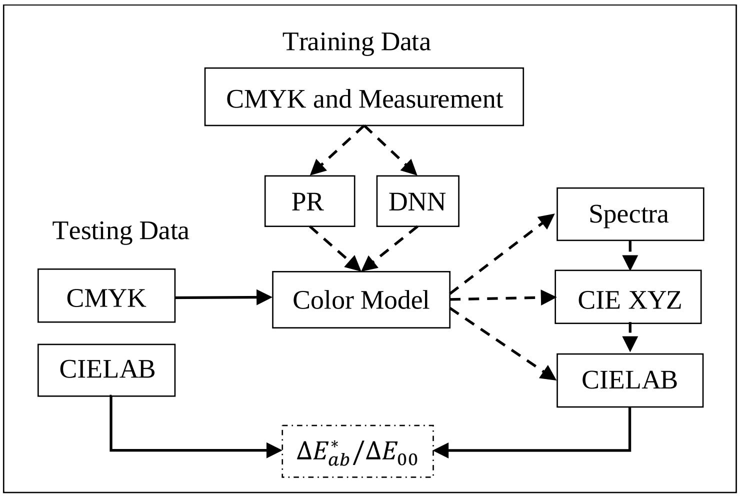

Figure 5.4 Process of forward colour characterisation for a 3D printer using different approaches and the validation procedure**.**

5.1.2.5 Model Evaluation

The 10-fold cross validation was applied to evaluate the accuracy of the colour characterisation models developed using different approaches, which means that the fitting procedure was performed 10 times with each fit consisting of 90% of the total data set selected at random and the remaining 10% used for validation. Consequently, 1814 of 2016 colour samples were used as the training data and the remining 202 colour samples were considered as the testing data for each process of performing colour characterisation.

The accuracy of each colour characterisation model was quantified by calculating the CIELAB and CIEDE2000 colour-difference values between the predictions and the measurements of the 202 testing data. Moreover, to assess the accuracy of the spectral data estimated by each model, the root-mean-square error ($RMSE$) was calculated in comparison to the raw measured spectral reflectance.

Additionally, in order to investigate the impact of the amount of training data on colour characterisation accuracy, different percentages of the entire dataset ranging from 5% to 95% were used as the training data, respectively, and the remaining colour samples were considered as the testing data. Table 5.2 lists the percentages and corresponding numbers of training data and testing data for exploring the effect of the sizes of training data, particularly for the method of deep neural network. The validation procedure was performed 10 times for each training dataset to achieve reliable results, when the percentage equalled to 90%, it was the case of 10-fold cross validation.

Table 5.2 The percentages and corresponding numbers of the training data and testing data.

	5%	10%	15%	20%	25%	30%	35%	40%	45%	50%
Train	101	202	302	403	504	605	706	806	907	1008
Test	1915	1814	1714	1613	1512	1411	1310	1210	1109	1008
	55%	60%	65%	70%	75%	80%	85%	90%	95%	
Train	1109	1210	1310	1411	1512	1613	1714	1814	1915	
Test	907	806	706	605	504	403	302	202	101	

5.1.3 Results

5.1.3.1 Model Performance

The average results of the 10-fold cross validation for the forward colour characterisation using different approaches are illustrated in Figure 5.5, and the corresponding CIELAB and CIEDE2000 colour-difference values are given in Table 5.3. It can be clearly seen that the method of deep neural networks gave much better performance than the 3rd polynomial regression, with the average colour differences smaller than 2.69 CIELAB units and 1.78 CIEDE2000 units for the five output variables. In comparison, the method of the 3rd polynomial regression produced greater colour differences, particularly for the cases of using CIE XYZ, spectral data (r) and principal components of spectral data (PCA(r)) as the output.

Regarding the results achieved using the 3rd polynomial regression, the best accuracy was produced using CIELAB as the output, with the average colour difference of 4.69 CIELAB units, followed by the logarithm of CIE XYZ (5.74 CIELAB units). For the results of the other three types of output variables, the average colour differences reached were larger than 11 CIELAB units (7 CIEDE2000 units).

As for the results produced using the deep neutral network, all the average colour differences attained were smaller than 3 CIELAB units (2 CIEDE2000 units). The smallest maximum value (5.52 CIELAB units and 3.47 CIEDE2000 units) was given when using the logarithm of CIE XYZ values as the output, which are similar to the best results obtained using the 3rd polynomial regression.

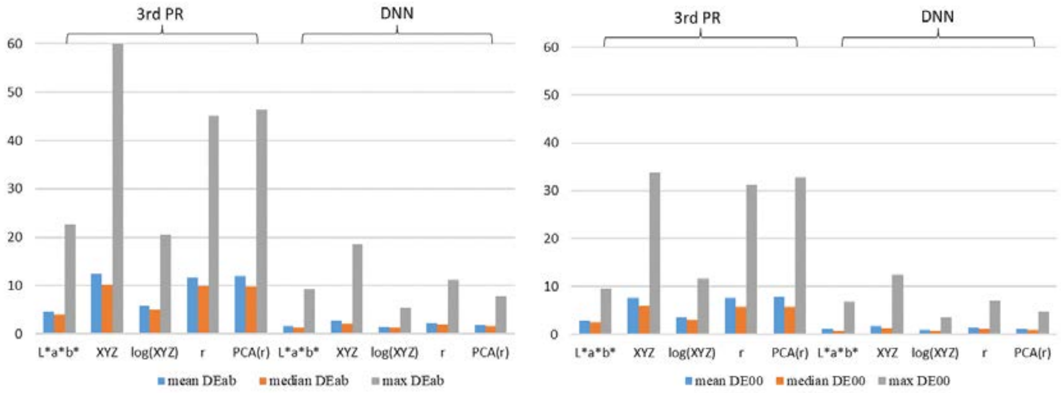

Figure 5.5 Histograms of CIELAB and CIEDE2000 colour differences of 10-fold cross validation for each model under CIE illuminant D65.

Table 5.3 CIELAB and CIEDE2000 colour differences of 10-fold cross validation for each method under CIE illuminant D65.

		CIELAB			CIEDE2000		
		Mean	Median	Max	Mean	Median	Max
3rd PR	Lab	4.69	3.95	22.72	2.89	2.55	9.49
	XYZ	12.44	10.26	60.46	7.63	5.86	33.69
	log(XYZ)	5.74	4.94	20.63	3.47	3.05	11.58
	r	11.74	9.86	45.16	7.70	5.75	31.21
	PCA(r)	12.05	9.75	46.34	7.80	5.81	32.87
DNN	Lab	1.59	1.27	9.25	1.06	0.87	6.91
	XYZ	2.69	2.13	18.53	1.78	1.35	12.47
	log(XYZ)	1.49	1.26	5.52	1.00	0.84	3.47
	r	2.34	1.93	11.19	1.40	1.16	6.99
	PCA(r)	1.84	1.62	7.82	1.18	1.03	4.84

Considering the colour-difference perceptibility and acceptability in industrial applications, the colour differences of the testing data were classified into three groups: $\Delta\mathrm{E} \leq 3$, $3 < \Delta\mathrm{E} \leq 6$, and $\Delta\mathrm{E} > 6$, according to the research work carried out by Hardeberg (2001), which were correspondingly defined as “Hardly perceptible”, “Perceptual, but acceptable” and “Not acceptable” (Velastegui and Pedersen 2021). Figure 5.6 illustrates the CIELAB and CIEDE2000 colour difference distributions in the three $\Delta\mathrm{E}$ groups. It shows that over nearly 60% of colour differences predicted using the deep neural networks method were less than or equal to 3 CIELAB units (over 80% in CIEDE2000 units). In contrast, only a minority (less than 35%) of the CIELAB colour differences estimated using the 3rd polynomial regression method were equal to or smaller than 3 units. When CIELAB and the logarithm of CIE XYZ values were used as the output, approximately 60% and 50% of CIEDE2000 colour differences were in the group of $\Delta\mathrm{E} \leq 3$.

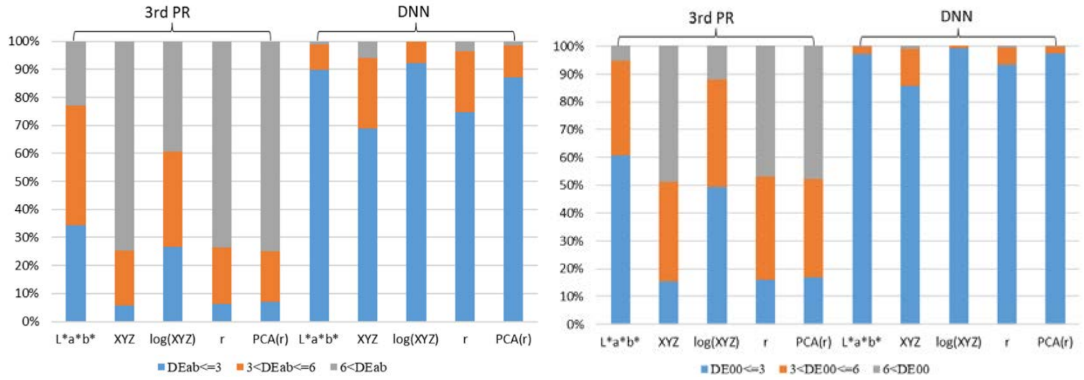

Figure 5.6 CIELAB (left) and CIEDE2000 (right) colour-difference distributions in the three $\Delta\mathrm{E}$ groups.

Regarding the results based on the 3rd polynomial regression and the spectral data, it failed to achieve a good performance, with an average colour-difference value of 11.74 CIELAB units (7.7 CIEDE2000 units). The same to the results produced using the principal components of spectral data, which resulted in over 70% of colour differences greater than 6 CIELAB units (almost 50% for CIEDE2000 units). In comparison, the method of deep neural networks gave a significantly better performance on spectral estimation, approximately 25% of colour differences larger than 3 CIELAB units and 10% in CIEDE2000 units.

To quantify the error in spectral estimation, the average $RMSE$ values of the 202 testing data between the predicted and the measured spectral data were calculated, and the results are given in Table 5.4. The $RMSE$ values obtained using the deep neural networks method were 0.51% and 0.48% for the spectra r and PCA(r), respectively, smaller than the values achieved using the polynomial regression method.

Table 5.4 The average $RMSE$ values of different methods in spectral estimation.

	PR + r	PR + PCA(r)	DNN + r	DNN + PCA(r)
$RMSE$	0.0206	0.0218	0.0051	0.0048

Figure 5.7 shows nine random examples of the spectral reflectance estimated using the PR (left) and DNN (right) methods, respectively, where the orange curves represent the measured spectral reflectance and the blue colour indicates the spectral data predicted from CMYK values. It can be seen that the spectral data estimated using the DNN method are much closer to the measured results, while for the PR predicted results the differences between the estimated spectral data and the measurements are obviously larger. For instance, the two curves in the lower left corner of Figure 5.7 (left) differ greatly, and the corresponding colour differences were 49.00 CIELAB units and 35.10 CIEDE2000 units. The CIELAB values of this sample were 18.49, 0.42, 25.48, which had very low lightness and higher yellowness. From Table 5.3, the maximum colour difference produced using the DNN method for spectral estimation was 11.19 CIELAB units and 7.82 CIEDE2000 units. It is indicated that the DNN method is suitable to predict spectral reflectance data from printer CMYK.

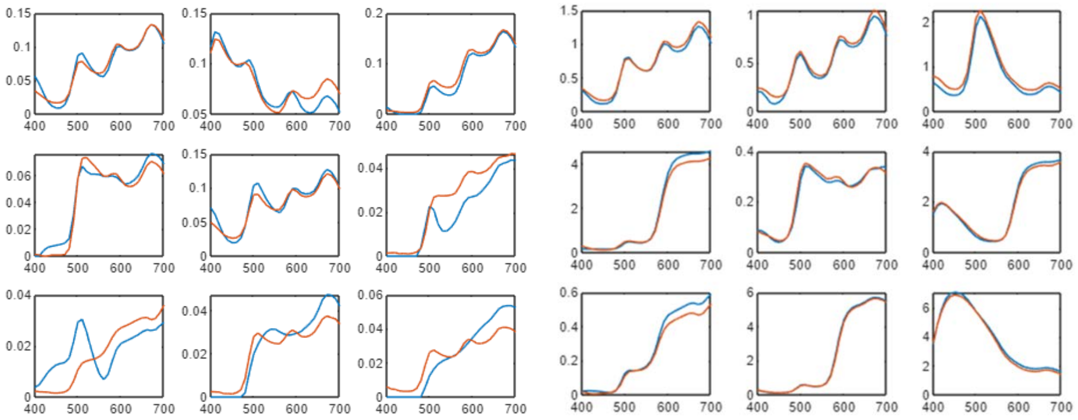

Figure 5.7 Nine random examples of spectral estimation respectively using the 3rd PR (left) and the DNN method (right).

In addition to quantifying the accuracy of colour characterisation for CIE illuminant D65, the colour differences under CIE illuminant A were calculated to investigate the effect of different illuminations on the colour characterisation results. The average results of 10-fold cross validation under CIE illuminant A are shown in Figure 5.8, which are very similar (slight smaller) to the colour-difference values achieved under CIE illuminant D65 (Figure 5.5). It is indicated that the two illuminations with different CCTs have negligible effect on the accuracy of colour characterisation for the 3D printer. Furthermore, it is evidenced that the DNN method yielded a higher level of accuracy than the PR method in characterising colours from printer CMYK.

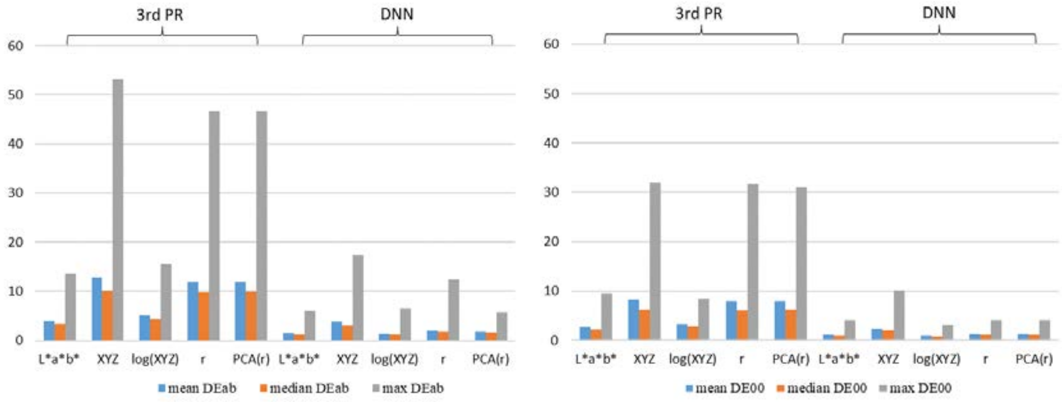

Figure 5.8 Histograms of CIELAB and CIEDE2000 colour differences of 10-fold cross validation for each model under CIE illuminant A.

5.1.3.2 Effect of Different Training Data Sizes

The accuracy of colour characterisation is not only determined by the method utilised, but also relies on the quality and diversity of the training data. In the present study, the effect of different sizes of training data on performing colour characterisation was investigated by quantifying the predicted errors. Figure 5.9 shows the average colour differences achieved using 5%-95% of the whole dataset as training data, and Figure 5.10 presents the results obtained through the DNN method.

Regarding the results in Figure 5.9, the largest colour difference was produced for each of the five output variables when the size of the training data was 101 (5% of the entire dataset), and the values decreased as the number of the training data increased to 302 colour samples (15%), indicating that more training data resulted in improved performance. However, once the size of the training data exceeded 302, the colour differences produced using the PR method remained stable regardless of further increases in the training data size, which were approximately 13 CIELAB units (8 CIEDE2000 units) for the outputs of CIEXYZ, spectra and PCA(r), and 5 CIELAB units (3 CIEDE2000 units) for CIELAB and the logarithm of CIE XYZ.

Similarly, the colour differences calculated using the DNN method, as shown in Figure 5.10, decreased dramatically from about 20 to 3 CIELAB units (from 12 to 2 CIEDE200 units), as the number in the training dataset increased from 101 to 1310 (5%-65%), afterwards, the colour-difference values differed very little with an increase in the size of the training data. In addition, it is evident that the results achieved using the DNN method were affected significantly by the training data size, and a larger training dataset including diverse and representative samples can provide a higher accuracy of capturing the underlying features and characterising the relationship. In comparison, different training data sizes have little effect on the predicted results for the PR method.

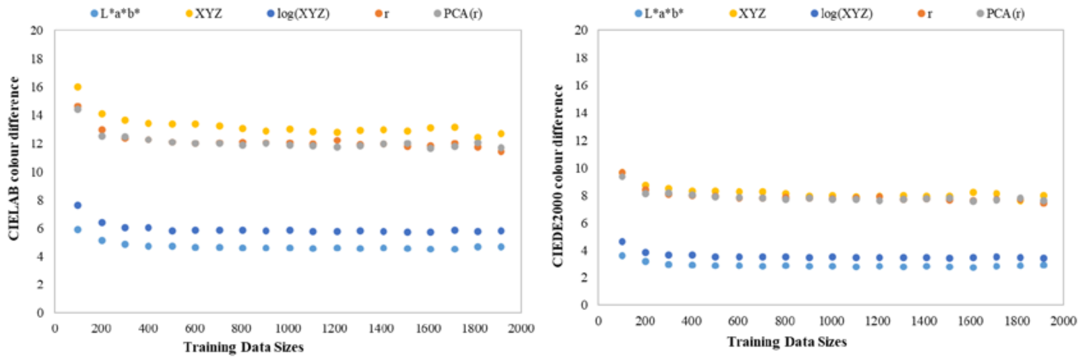

Figure 5.9 The average CIELAB (left) and CIEDE2000 (right) colour differences achieved using different training data sizes for the PR method.

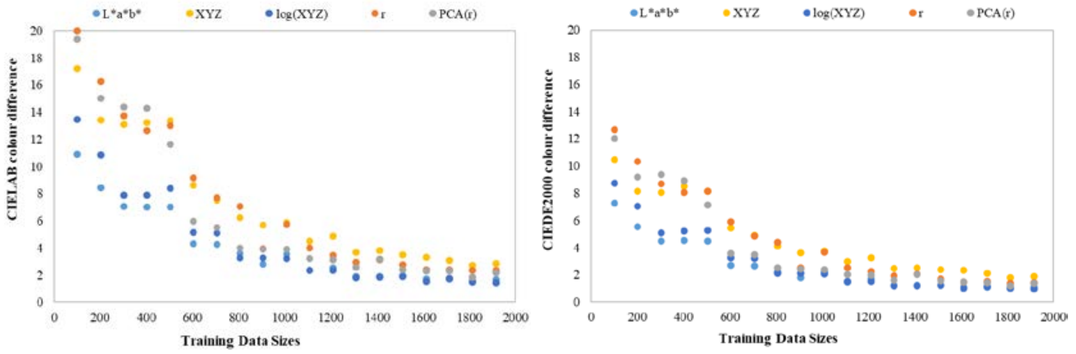

Figure 5.10 The average CIELAB (left) and CIEDE2000 (right) colour differences achieved using different training data sizes for the DNN method.

5.1.4 Discussion

Based on a large database consisting of 2016 colour samples, the deep neural networks method yielded less than 3 CIELAB units (2 CIEDE2000 units) in the forward colour characterisation for a 3D printer, outperforming the 3rd polynomial regression which produced colour differences of 4.69-

12.44 CIELAB units (2.89-7.80 CIEDE2000). The advantages were significant when CIE XYZ, spectra, and the principal components of spectra were treated as the output of colour characterisation, with approximately 10 CIELAB units and 6 CIEDE2000 units reduced by using the DNN method. It is indicated that the 3rd polynomial regression method cannot accurately characterise the relationship between CMKY values and spectral data. This is probably due to the high dimensions and complex features of the spectral reflectance. In such cases, the DNN method is preferred because it has better self-learning capabilities for complex patterns and provide higher accuracy. Velastegui et al. (2021) used a FOGRA53 dataset consisting of 1617 colour samples to compare the performance of four different machine learning approaches on colour space transformation between CMYK and CIELAB colour spaces, and it was found that the Deep Neural Networks produced 99.5% of colour differences less than 3 CIELAB units.

One interesting finding is that the logarithm of CIE XYZ gave higher accuracy than CIE XYZ as the output of printer colour characterisation, reducing nearly 7 CIELAB units (4 CIEDE2000 units) for the PR method and about 1 unit for the DNN method. This is possibly because of the similarity between a logarithmic function and a power law function which was applied to the calculation from CIE XYZ to CIELAB values, as shown in Equations (2.4-2.6), leading to the results predicted from the logarithm of CIE XYZ were closer to CIELAB values than the predictions from CIE XYZ. Typically, the logarithm of tristimulus value Y is used as a uniform lightness scale (Ohta and Robertson 2006). In this study, the prediction results of CIELAB and the logarithm of CIE XYZ as the output were more accurate than the other three variables, and CIELAB achieved the smallest colour difference for the PR method, the logarithm of CIE XYZ produced the best accuracy for the DNN method.

Additionally, the impact of the training data size on the accuracy of printer colour characterisation was explored, with the amount of the training data varied from 101 to 1915. The results revealed that the PR method exhibited minimal dependence on the size of the training data for colour estimation, while the colour differences estimated using the DNN method decreased significantly as the number of the training data increased. This is related to the approach and complexity in these two methods. The polynomial regression is a simple and fast algorithm, fitting a relationship by minimizing the sum of square errors between the predicted and the actual values, while the deep neural networks is a powerful and complex machine learning tool capable of learning features at multiple levels of abstraction.

Although the DNN method provided accurate prediction results, it highly relied on the training data size. The optimal number of training data was at least 1310 (65% of the dataset) for achieving consistent smaller colour differences in this study, which indicates that the amount of the training data is preferred to be greater than that of the testing data. In addition, the process of training a network was time-consuming, and the larger the training data size, the more time it takes. Specifically, it took about 200 minutes to complete a 10-fold cross validation based on a common laptop with the Intel® Core™ i5-1035G1 CPU processor. The time was reduced to approximately 40 minutes when using a high-performance desktop PC with the intel® XEON® Silver 4214 CPU processor which was desired to perform neural network training. In contrast, the PR method only took less than 1 second to give the results of a 10-fold cross validation. Therefore, it is generally compromised between prediction accuracy and processing time.

5.2 Practical Colour Characterisation

In addition to theoretical analysis of the accuracy of forward colour characterisation using various approaches, a practical experiment was conducted based a Stratasys J750 3D printer to perform reverse colour characterisation which quantified how the printer responds to different colours. The primary goal of this practical experiment was to ensure accurate and consistent colour reproduction of Chinese skin tones, as the participants in the skin colour data collection (described in Chapter 4) were mostly Chinese. Furthermore, given the significant variation in skin tones among different ethnic groups, it would be advantageous to perform colour characterisation separately for each group to enhance prediction accuracy.

5.2.1 3D Print of the Skin Colour Chart

In order to accurately reproduce facial skin tones, the Chinese skin colour chart consisting of 216 colour patches, as shown in Figure 4.18, was used to perform reverse colour characterisation of the Stratasys J750 printer in practice, which aimed to transform the output vectors back to the input vectors for well control of the printed colours. Specifically, the target skin colour chart with known CIELAB values was designed as an A4 size (210 mm × 290 mm) RGB image with each patch being 15 mm × 15 mm in MATLAB. A 3D model was created in Blender with a size of 210 mm (length)

× 290 mm (width) × 5 mm (height), and the RGB image of the skin colour chart was mapped onto the 210 mm × 290 mm surface of the 3D model, as shown in Figure 5.11. The digital 3D model of the skin colour chart was sent to a Stratasys J750 3D printer in GrabCAD Print, with Vivid CMYK and high mix printing mode selected. The printing process took approximately 3-4 hours.

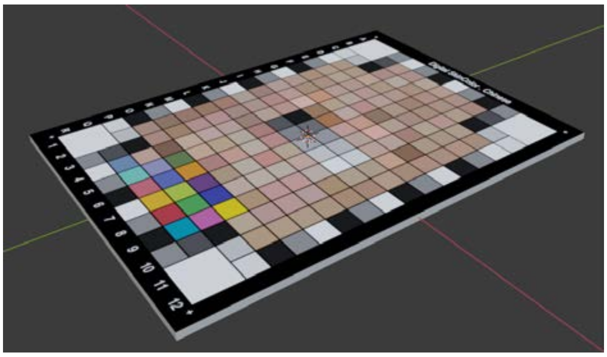

Figure 5.11 The digital 3D model of the skin colour chart.

5.2.2 Colour Characterisation Process

The spectral reflectance data of each patch in the 3D printed skin colour chart were measured using an X-Rite Ci64 spectrophotometer which has d/8° measurement geometry. The measurements were taken using a medium aperture size of 14 mm, and SCE measurement mode was selected because of the glossy surface finish. Then the colour characterisation was performed between the RGB values sent to the printer and the measured data of the 216 printed patches.

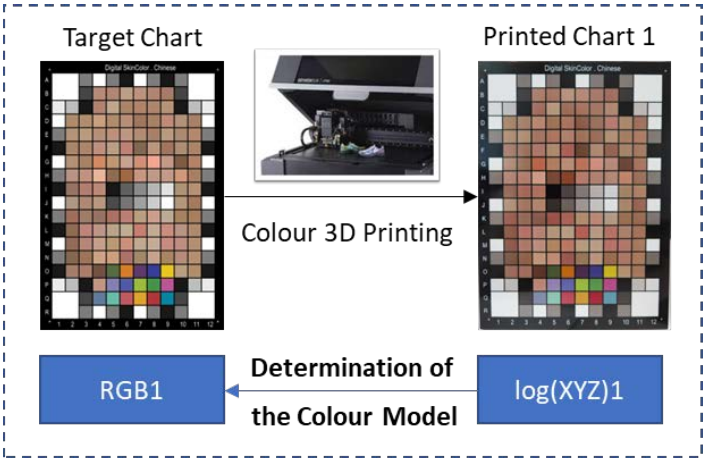

Figure 5.12 Diagram of the colour characterisation process of the 3D printer.

The logarithm of CIE XYZ, abbreviated as log(XYZ), was used for colour characterisation, given that it produced good performance on predicting those colours with moderate lightness like Chinese skin tones. In addition, considering that deep neural networks require a large number of training samples to achieve accurate performance, the third-order polynomial regression was employed to develop a colour characterisation model, specifically for Chinese skin colour reproduction, due to its reasonable results and ease of implementation based on a small dataset. Therefore, a mathematical colour characterisation model was determined by applying the 3rd polynomial regression with the least-squares method to transform the logarithm of CIE XYZ to RGB values of the 216 samples, as illustrated in Figure 5.12.

5.2.3 Colour Accuracy

To quantify the accuracy of the determined colour characterisation model, it was applied to the target skin colour chart with known CIELAB values to convert the logarithm of CIE XYZ tristimulus values of the 216 patches back to printer-based RGB values for faithfully reproducing the desired colours. The process is demonstrated in Figure 5.13. The characterised colour chart was as mapped to the 3D model and sent to the colour 3D printer.

The second skin colour chart (Figure 5.13) was printed using the same settings as the first print (Figure 5.12), and each colour patch was measured using the same spectrophotometer. The CIELAB and CIEDE2000 colour differences of the 216 patches between the first/second printed chart (before/after performing colour characterisation) and the target skin colour chart were calculated and given in Table 5.5.

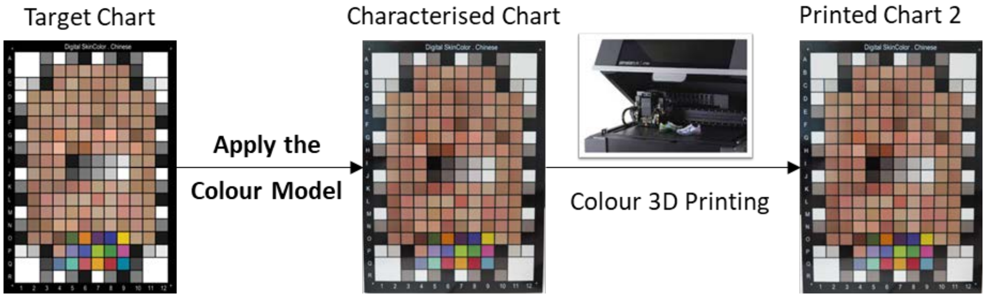

Figure 5.13 Validation process for the colour characterisation model.

Table 5.5 CIELAB and CIEDE2000 colour differences of the 216 patches.

	After characterisation			Before characterisation		
	mean	min	max	mean	min	max
CIELAB	2.81	0.11	17.49	7.77	2.85	18.43
CIEDE2000	1.95	0.12	6.92	6.09	2.50	7.91

Before performing colour characterisation based on the skin colour chart, the average colour difference of the 216 patches was 7.77 CIELAB units (6.09

CIEDE2000 units), and it was reduced to 2.81 CIELAB units (1.95 CIEDE2000 units) after applying the colour characterisation model. It is indicated a significant improvement in the predictive accuracy. Similarly, the minimum colour difference decreased from 2.85/2.5 to 0.11/0.12 CIELAB/CIEDE2000 units. Regarding the maximum colour difference, the value dropped very little, this is because of the white and black patches in the chart which had values of R=G=B=255.

For the purpose of focusing on the accuracy of skin colour, the 118 patches related to skin tones were separated from others in the chart, and Table 5.6 gives the mean, minimum and maximum CIELAB and CIEDE2000 colour differences of the 118 skin tone patches. Figure 5.14 shows the CIELAB colour-difference histograms before (left) and after (right) performing colour characterisation. It is evident that the majority of colour differences were significantly reduced to less than 3 CIELAB units, with most falling in the 0-1 range, thanks to the colour characterisation model. Only two samples showed colour differences greater than 6 units. In contrast, prior to applying the model, most colour differences were between 7-9 CIELAB units.

Table 5.6 CIELAB and CIEDE2000 colour differences of the 118 skin colour patches.

	After characterisation			Before characterisation		
	mean	min	max	mean	min	max
CIELAB	1.35	0.11	10.48	7.41	2.85	10.39
CIEDE2000	1.35	0.12	6.76	6.31	2.50	7.91

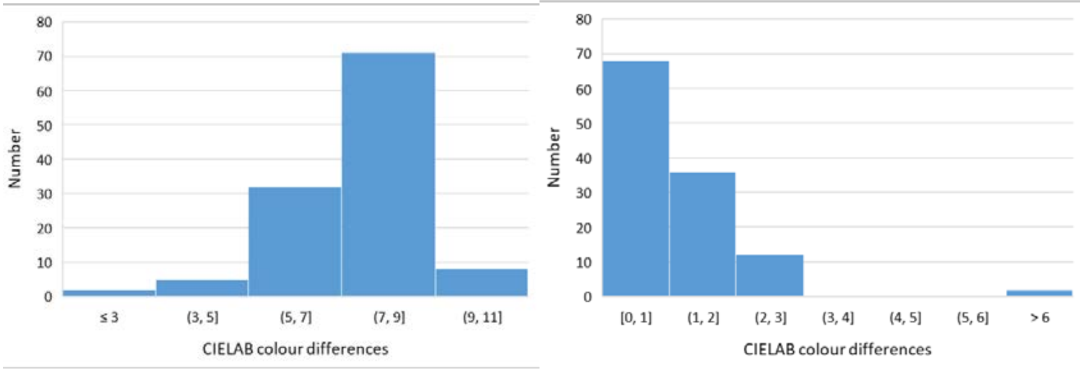

Figure 5.14 CIELAB colour-difference histogram of the 118 patches with skin tones before (left) and after (right) performing colour characterisation.

Regarding the reproduction of the 10 grey-scale patches in the centre of the skin colour chart, Table 5.7 gives the target CIELAB values and the measurements of the two 3D printed chart. The chart 1 was printed directly from the target chart, and the chart 2 was the result after applying colour characterisation. The CIELAB values of the chart 1 revealed that the 3D printer generated grey tones with lower lightness and higher yellowness than the intended target, except for black, due to the printer's individual performance. In comparison, the results in the chart 2 demonstrated a significant improvement in the printed grey tones, attaining CIELAB values that closely matched to the target, based on the developed colour characterisation model.

Table 5.7 CIELAB values of the ten grey-scale patches in the target chart and the two 3D printed charts and the average colour differences.

Target Chart			Print Chart 1			Print Chart 2		
L^*_{10}	a^*_{10}	b^*_{10}	L^*_{10}	a^*_{10}	b^*_{10}	L^*_{10}	a^*_{10}	b^*_{10}
0.00	0.00	0.00	13.62	-0.37	0.58	13.42	-0.15	0.45
31.89	0.00	0.00	31.80	0.18	4.65	31.13	-0.56	-0.10
40.73	0.00	0.00	38.51	0.78	3.79	40.68	-0.89	-1.17
49.64	0.00	0.00	45.61	0.78	5.34	49.34	-0.58	-0.93
57.86	0.00	0.00	52.15	1.49	5.62	57.88	0.39	-0.77
66.24	0.00	0.00	59.45	1.24	4.94	66.16	-0.07	-0.04
74.05	0.00	0.00	66.35	1.21	4.60	74.22	0.21	-0.46
82.05	0.00	0.00	74.09	0.52	2.66	81.53	-0.30	-0.75
89.53	0.00	0.00	81.13	-0.47	2.81	88.75	-0.50	0.69
100.00	0.00	0.00	91.04	-1.43	3.07	91.32	-2.72	2.61
CIELAB			7.48			2.13		
CIEDE2000			5.99			1.74		

5.2.4 Discussion

By implementing printer colour characterisation based on a specific Chinese skin colour chart, the average colour difference of skin tones was reduced from 7.41 to 1.35 CIELAB units (from 6.31 to 1.3 CIEDE2000 units), which indicates a significant improvement in the accuracy of skin colour reproduction. Compared to previous studies, Xiao et al. (2016a) used a ColorChecker DC chart and the third-order polynomial regression to determine a 3D printer colour profile transforming between printer RGB and CIE XYZ colour spaces, and the achieved accuracy of 14 printed skin colour samples was 4.50 CIELAB units. Sohaib et al (2018) characterised a colour 3D printer based on a ColorChecker Digital SG chart, giving an average CIELAB colour difference of 3.96 for 110 3D printed PANTONE skin tone samples. Therefore, to achieve higher accuracy of 3D colour reproduction of skin tones, it is recommended to use a specific skin colour chart instead of conventional colour charts. This finding demonstrated that the accuracy of printer colour characterisation is significantly influenced by the selection of training samples.

In the colour characterisation of 3D printer, the third order polynomial regression provided a good performance, giving an average colour difference of 2.81 CIELAB units and 1.95 CIEDE2000 units. Moreover, Xiao et al. (2013) compared the performance of linear, second and third order polynomial regression on 3D printer colour characterisation, and it was summarised that the third order polynomial regression model gave the smallest predicted colour difference whereas the linear transformation produced the worst performance. Liu et al. (2019) also reported that the third-order polynomial regression yielded smaller colour differences than the quadratic polynomial for developing a colour profile for a 3D printer.

In generally, prior to implementing the colour characterisation model developed using a skin colour chart, the colours printed by the 3D printer appeared less vibrant and had a yellowish tint in comparison to the target colours. With the introduction of the model, the printed colours were corrected, resulting in a significant improvement in accuracy of faithful and realistic skin colour reproduction.

5.3 Summary

In this chapter, two studies on colour characterisation of a 3D printer were carried out, one is the theoretical analysis on developing forward colour characterisation models using different methods, and the other one is the practical reverse colour characterisation transforming CIE colorimetric values to RGB values to achieve accurate skin colour reproduction using the 3D printer.

In the first study, the third order polynomial regression and deep neural networks were employed to perform colour characterisation from CMYK to CIELAB colour space, based on a dataset consisting of 2016 colour samples which was produced using a Stratasys J750 3D colour printer. Five output variables including CIE XYZ, the logarithm of CIE XYZ, CIELAB, spectra reflectance and the principal components of spectra were compared for the performance of printer colour characterisation. Moreover, the effect of different training data sizes on predictive accuracy was investigated. The 10-fold cross validation was applied to evaluate the accuracy of the models developed using different approaches, and CIELAB colour differences were calculated with CIE illuminant D65. The results showed that the DNN method produced much smaller colour differences than the PR method, but it is highly dependent on the amount of training data. In addition, the logarithm of CIE XYZ as the output provided higher accuracy than CIE XYZ.

In order to enhance the accuracy of reproducing skin colours in practical, a specialised colour chart designed for Chinese skin tones was utilised instead of relying on conventional colour charts like the ColorChecker SG chart to perform reverse colour characterisation for a Stratasys J750 3D printer. The third-order polynomial regression was adopted to develop a mathematical model converting the logarithm of CIE XYZ to RGB colour space. The accuracy of the model was quantified by calculating the average colour difference of the printed chart, which was 2.81 CIELAB units. The predicted error for the 118 printed skin colour patches was about 1.35 CIELAB units, indicating significant improved accuracy of skin colour reproduction using the 3D printer.

Chapter 6
Colour-Difference Evaluation of 3D Printed Objects

The current colour-difference formulae such as CIELAB and CIEDE2000 were developed based on flat coloured samples, currently there is no standard guidance for evaluating colour differences of 3D objects. CIE has listed the reproduction and measurement of 3D objects as one of the top priority topics in its current research strategy, and CIE Technical Committee 8-17 has been established to develop methods for evaluating the colour differences between 3D objects.

To understand the basic visual perception of coloured 3D objects in lightness, chroma and hue scale, a series of psychophysical experiments were conducted to collect visual colour-difference data of 3D objects. The performance of CIELAB and CIEDE2000 colour-difference formulae was tested and quantified, furthermore, the parametric factors in the colour-difference formulae were optimised to better fit the visual results collected from 3D objects.

6.1 3D Printed Spherical Samples

6.1.1 Colour Samples around 5 CIE Colour Centres

Based on the five CIE recommended colour centres: grey, red, green, yellow, and blue (Witt 1995), 45 spherical samples with a diameter of 50 mm were printed using the Stratasys J750 colour 3D printer as shown in Figure 3.6. A high mix printing mode and a matte surface finish were selected in 3D printing, and a waterjet machine was used to remove support materials. Figure 6.1 shows the 45 printed colour samples after postprocessing, where there are 5 grey samples with similar chroma and hue but different lightness and 10 colour samples with different variations in individual lightness, chroma and hue scales for red, green, yellow and blue colour centres, respectively. A Konica Minolta CM-700d spectrophotometer with a SAV 3 mm aperture and SCI mode, as shown in Figure 3.7 (right), was used to measure the colour of each printed sample. The measured spectral reflectance data were used to calculate corresponding CIELAB values with the CIE 1964 standard observer and the measured SPD of the D65 simulator of the viewing cabinet used for visual assessment (see Section 6.2.2).

Figure 6.1 The 3D printed spherical samples based on the 5 CIE recommended colour centres.

In order to quantify the colour homogeneity of the 3D printed objects, each spherical sample was measured at three different points, and the $MCDM$ value in CIELAB units was calculated using the results of the three measurements. The average $MCDM$ value of the 45 samples obtained is 1.77 CIELAB units, which indicates that the 3D printed spherical samples have reasonable colour uniformity.

The average CIELAB values of three measurements for each sample are illustrated in $L^*_{10}C^*_{ab,10}$ and $a^*_{10}b^*_{10}$ diagrams in Figure 6.2. The triangle symbols are approximately positioned at the 'centres of gravity' of the 3D printed samples around each CIE recommended colour centre. It can be seen that grey samples vary mainly in the lightness scale and have slight changes in chroma and hue dimensions. For the other four colour centres, the samples differ primarily in one of the three attributes.

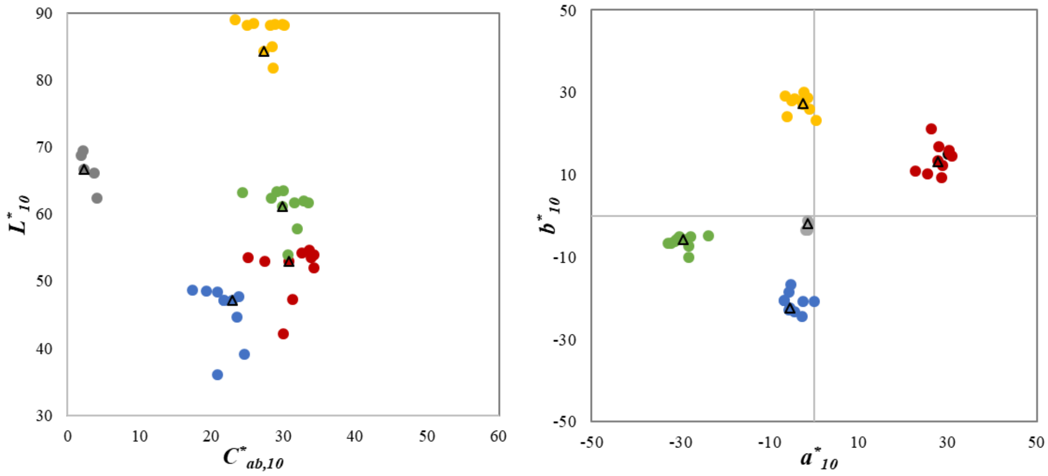

Figure 6.2 Colour distributions of the 45 spherical samples in $L^*_{10}C^*_{ab,10}$ and $a^*_{10}b^*_{10}$ plane.

Based on the 45 spherical colour samples printed using the J750 colour 3D printer, two sample sets were generated to collect visual colour-difference data, named Sample Set I and Sample Set II, respectively. Regarding the Sample Set I, 42 pairs of colour samples were prepared to have predominant lightness, chroma or hue differences, i.e., the colour difference of each pair of 3D samples is mainly (at least 85%) given by one colour attribute (e.g., lightness differences ΔL_{10}^{*}, chroma differences $\Delta C_{ab,10}^{*}$, or hue differences $\Delta H_{ab,10}^{*}$). Figure 6.3 shows the colour difference of each sample pair for the five colour centres.

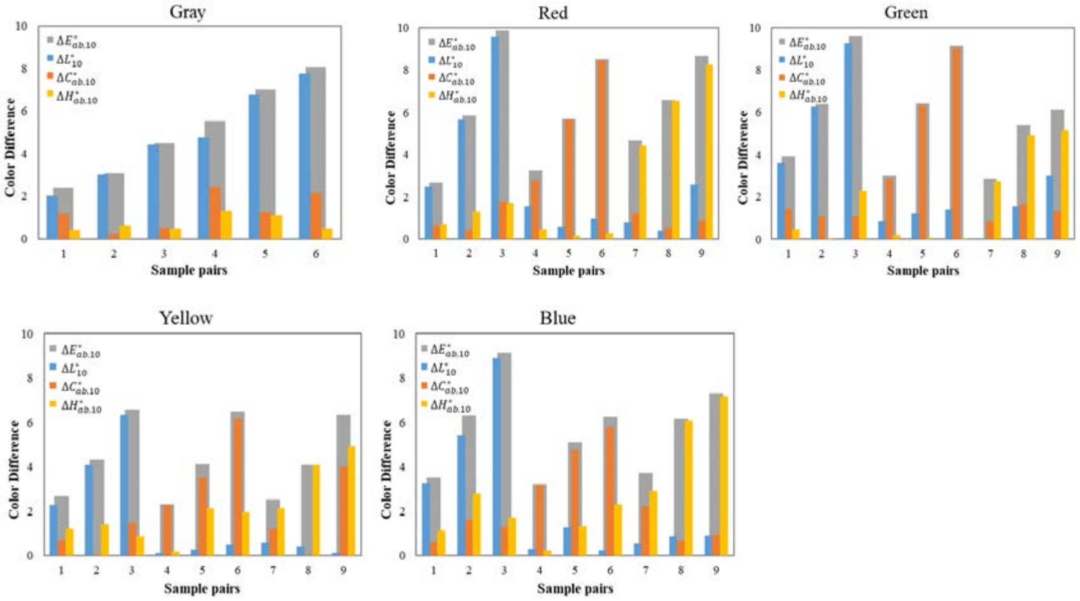

Figure 6.3 Values of $\Delta L_{10}^{*}, \Delta C_{ab,10}^{*}, \Delta H_{ab,10}^{*}, \Delta E_{ab,10}^{*}$ for the 42 pairs of 3D samples in Sample Set I.

For the grey centre, 6 pairs of 3D samples were produced to have colour difference mainly in lightness dimension, and for each of the four chromatic centres, 9 sample pairs were assembled to have predominant lightness, chroma and hue differences, respectively. The colour-difference magnitudes in the three attributes are designed to be consistent, always ranging from 2-10 $\Delta E_{ab,10}^{*}$, so that the visual perception can be compared for lightness, chroma and hue scales. Overall, there were 42 pairs of 3D samples in Sample Set I, including 18 lightness-difference pairs ($\Delta L_{10}^{*}/\Delta E_{ab,10}^{*} \geq 0.85$), 12 chroma-difference pairs ($\Delta C_{ab,10}^{*}/\Delta E_{ab,10}^{*} \geq 0.85$), and 12 hue-difference pairs ($\Delta H_{ab,10}^{*}/\Delta E_{ab,10}^{*} \geq 0.85$). The average colour difference of the 42 pairs of 3D samples was 5.46 CIELAB units.

In terms of the Sample Set II, it consists of 40 pairs of spherical samples with an anchored reference sample (the triangle symbols in Figure 6.2) for each of the five CIE colour centres. Specifically, there were 4 pairs for the CIE grey centre and 9 pairs for each CIE chromatic centre. The colour differences of the 40 sample pairs ranged from 1 to 12 CIELAB units, and the average colour difference was 4.58 CIELAB units.

Overall, a total of 82 pairs of 3D printed spherical samples (42 pairs in Sample Set I and 40 pairs in Sample Set II) were used in the psychophysical experiments to collect visual-colour difference data given by human observers. More specifically, the visual results collected from Sample Set I were used to investigate the human visual colour perception of these 3D objects in terms of the lightness, chroma and hue dimensions and optimise the parametric factors in CIELAB and CIEDE2000 colour-difference formulae. The visual results of Sample Set II were used to test the prediction performance of the optimised colour-difference formulae.

6.1.2 Colour Samples with Skin Tones

Based on the facial skin colour data collected from human participants using a spectrophotometer, the average CIELAB values are 60.41, 13.07, 16.35. This colour was regarded as a reference, and 9 colours with different lightness, chroma and hue differences from it were determined and printed using the Stratasys J750 colour 3D printer. The colour-difference magnitudes and the printing process of these samples were the same as Section 6.1.1. Figure 6.4 displays the 10 spherical samples printed with skin tones, changing in lightness, chroma and hue scale, respectively. Moreover, nine pairs of skin colour samples were produced for visual assessments.

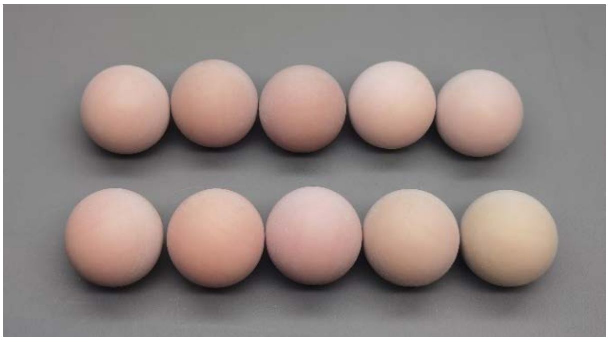

Figure 6.4 The 3D printed spherical samples based on the facial skin colour data collected.

6.2 Psychophysical Experiments

6.2.1 Grey-Scale Method

The grey-scale method has been widely used for visual assessment due to its ease of use and accurate results. In the present study, the *Grey scale for assessing change in colour* from the Society of Dyers and Colourists (SDC), following ISO 105-A02 (ISO 1993), was used in the visual experiments, as shown in Figure 6.5. It consists of 9 pairs of non-glossy neutral grey coloured chips, with grades of 1, 1.5, 2, 2.5, 3, 3.5, 4, 4.5 and 5. The larger the grey-scale number, the smaller the colour difference. The colour difference in the grey scale is predominantly caused by a lightness difference.

Figure 6.5 The SDC 9-step Grey Scale for assessing change in colour.

The spectral reflectance of each grey chip was measured using a CM700d spectrophotometer with SAV 3 mm and SCI, and the colour difference between each pair of grey chips was calculated for the CIE1964 standard observer under the illumination used in the visual experiments. Figure 6.6 plots the CIELAB and CIEDE2000 colour-difference values of the 9 grades in the grey scale. The grade 1 has the largest colour difference (13.36 $\Delta E^*_{ab,10}$ or 13.13 $\Delta E_{00,10}$), and the grade 5 has almost no colour difference (0.18 $\Delta E^*_{ab,10}$ or 0.16 $\Delta E_{00,10}$). In addition, it can be seen from Figure 6.6 that the colour-difference values of the 9 grey-scale grades calculated using CIEDE2000 formula were slightly smaller than those of CIELAB.

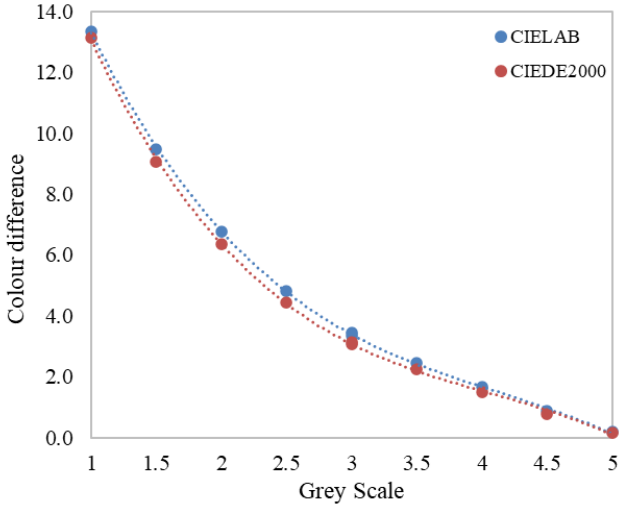

Figure 6.6 Relationship between the 9 grades in the SDC grey scale and their measured colour differences in CIELAB and CIEDE2000 units.

In order to convert the grey-scale grades given by human observers to colour differences, the third order polynomial regression was selected and used to quantify the relationship between the grey-scale grade numbers and the corresponding colour differences. The fitted curves are illustrated in Figure 6.6, and the determined equations for CIELAB and CIEDE2000 colour-difference units are expressed in Equations (6.1) and (6.2), respectively, with R^2 values of 0.9998 and 0.9960. Considering that this study aimed to test and optimise the CIELAB and CIEDE2000 formulae, both equations were used separately to obtain the visual colour-difference values.

$$\Delta V_{ab,10} = -0.25 \times GS^3 + 3.05 \times GS^2 - 13.95 \times GS + 24.46 \quad (6.1)$$

$$\Delta V_{00,10} = -0.28 \times GS^3 + 3.36 \times GS^2 - 14.83 \times GS + 24.81 \quad (6.2)$$

6.2.2 Visual Colour-Difference Assessment

6.2.2.1 VeriVide Viewing Cabinet

A VeriVide viewing cabinet with a D65 simulator was used in the visual colour-difference assessments. The spectral power distribution of the D65 illumination was measured using a Konica Minolta CS2000 spectroradiometer and a reference white tile, and the relative SPD is illustrated in Figure 6.7. The correlated colour temperature, CIE colour rendering index Ra and luminance of this illumination measured at the centre of the viewing cabinet were 6519 K, 97 and 412.35 cd/m^2, respectively.

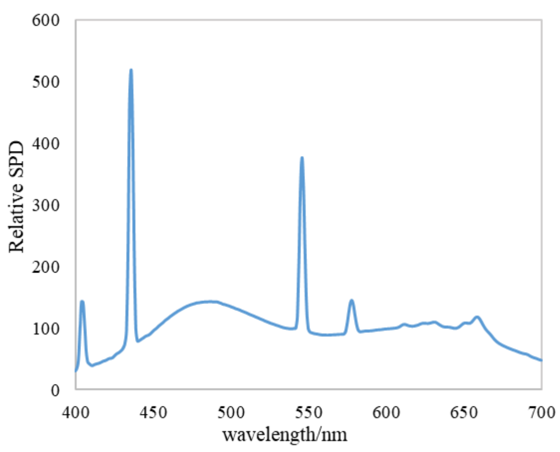

Figure 6.7 The relative SPD of the D65 illumination in the VeriVide viewing cabinet.

The visual experiments were conducted in a dark room, and human observers were asked to adapt to the dark surround for two minutes. Before starting psychophysical experiments, a pilot experiment was performed to train the observers to make the visual assessments using the grey scale method. Each pair of 3D samples was placed in the centre of the viewing cabinet, as shown in Figure 6.8. The observer’s task was to evaluate the magnitude of the colour difference in the pair in comparison with the perceived colour differences in the pairs of the grey scale. All the testing pairs were presented in a random order, and observers were encouraged to give intermediate assessment values with one decimal between two contiguous grey pairs (e.g., 3.6 for a colour difference between the pairs 3.5 and 4 but closer to 3.5 than to 4). During the visual experiments, observers had a fixed viewing position with an approximate distance of 50 cm from the samples and a 45° viewing angle. Each observer repeated the visual assessments of all testing pairs three times in different time periods.

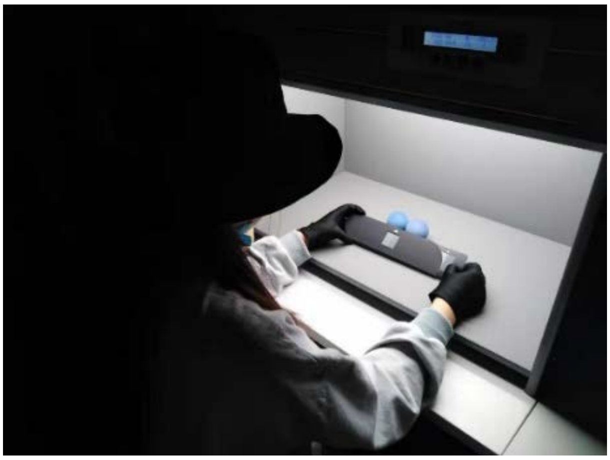

Figure 6.8 An example of visual colour-difference assessment in a VeriVide viewing cabinet.

A panel of 15 observers (10 females and 5 males) participated in the visual experiments, with ages ranging from 25 to 29. They were postgraduate students from the University of Leeds and had normal colour vision according to the Ishihara test. Most observers had little experience in colour-difference evaluation. A total of 3690 assessments (82 pairs × 3 repetitions × 15 observers) were achieved to collect visual colour-difference data of 3D printed spherical samples from the psychophysical experiments.

Regarding the 3D spherical samples with skin tones, 5 out of the 15 observers participated in the same psychophysical experiment and gave their visual assessments of the colour differences of 9 pairs of 3D skin colour samples.

6.2.2.2 X-Rite Virtual Light Booth

Considering that the 3D objects can be viewed from different directions and angles in the real world and there is no specific surface to be viewed like 2D objects, additional visual assessments were conducted in a X-Rite Virtual Light Booth with a rotate stage, as shown in Figure 6.9. The rotation speed and direction of the stage were controlled using buttons in the control panel.

The D65 illumination was provided in the light booth, and it was measured using a CS2000 spectroradiometer. The measured CCT, CIE rendering index and luminance were 6078 K, 97, 448.79 cd/m^2, respectively. Figure 6.10 plots the relative SPD of the D65 simulator in the X-Rite virtual light booth.

Each pair of 3D samples was placed in the centre of the rotate stage, and observers were asked to assess the colour difference of the test sample pair rotated with the stage. In such case, the 3D samples were viewed from 360 degrees during visual assessments. Five out of the 15 observers in the Section 6.2.2.1 were invited to evaluate the colour differences of the 82 rotated 3D sample pairs, subsequently. In addition, the same visual assessments were conducted on the 82 pairs of 3D samples in the light booth without any rotation so that the effect of rotation on colour-difference assessments can be compared.

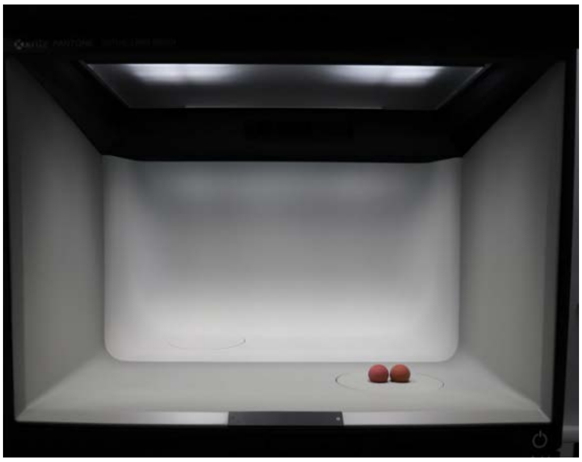

Figure 6.9 The X-Rite virtual light booth with a rotate stage.

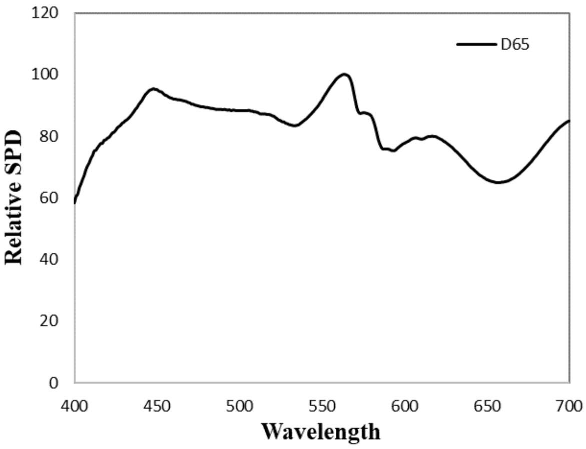

Figure 6.10 The relative SPD of the D65 illumination in the X-Rite virtual light booth.

6.3 Visual Results

6.3.1 Observer Variability

The observer variability was quantified by using the $STRESS$ index (see Section 2.6.2), based on the visual colour-difference data of the 82 pairs of 3D sample pairs collected from the psychophysical experiments. The average $STRESS$ values for intra- and inter-observer variability were 30.7 and 30.9 CIELAB units (31.4 and 31.7 CIEDE2000 units), respectively. Similar results were achieved by Huang et al. (2022b) where the intra- and inter-observer variability for matte spherical samples were 21.9 and 31.2 CIELAB units, respectively. In comparison, the intra-observer variability in the present study was relatively larger, which is possibly because three repetitions were performed in this study by each observer. Moreover, Jiang et al. (2021) reported that the observer variability in colour-difference evaluation of 3D objects is slightly larger (23.5 CIELAB units for inter and 14.9 for intra) than that of flat 2D objects (19.4 CIELAB units for inter and 12.6 for intra).

6.3.2 Visual Colour Difference

The visual colour-difference results (ΔV) of the 82 pairs of 3D samples in the VeriVide viewing cabinet were plotted in Figure 6.11 against the corresponding colour-difference values computed using the CIELAB (a) and CIEDE2000 (b) formulae. It shows that the visual data can be fitted as linear relationships (the dotted lines) to the computed colour differences, with R^2 values of 0.6244 and 0.6986 for CIELAB and CIEDE2000, respectively. It was to be expected that the scatter points should fall on the 45° dashed line if the colour-difference formula can exactly predict the visual results, and the larger the scatter, the worse the colour-difference formula performs. It can be seen from Figure 6.11 that the $\Delta E_{00,10}$ cluster data have less scatter than the $\Delta E^*_{ab,10}$ data, and the $\Delta E_{00,10}$ scatters tend to be closer to the 45° dashed line than $\Delta E_{ab,10}$, especially within approximately 6 units of colour-difference. This is in line with the statement that the CIEDE2000 formula was developed to fit visual assessment datasets of small-medium colour differences, typically under five CIELAB colour-difference units.

Additionally, the ΔV magnitudes in Figure 6.11 are almost half (0.48) those of the calculated colour-difference values. It was generally assumed that the ΔV values would tend to be close to the ΔE values if the colour-difference formula is a good predictor of the visual data, but it has been reported that in most cases the ratios, instead of the absolute values of ΔV and ΔE, are helpful for testing colour-difference formulae (Luo and Rigg 1987a). Poor correlation indicates that the colour-difference formula should be improved to provide a better performance of colour-difference assessment.

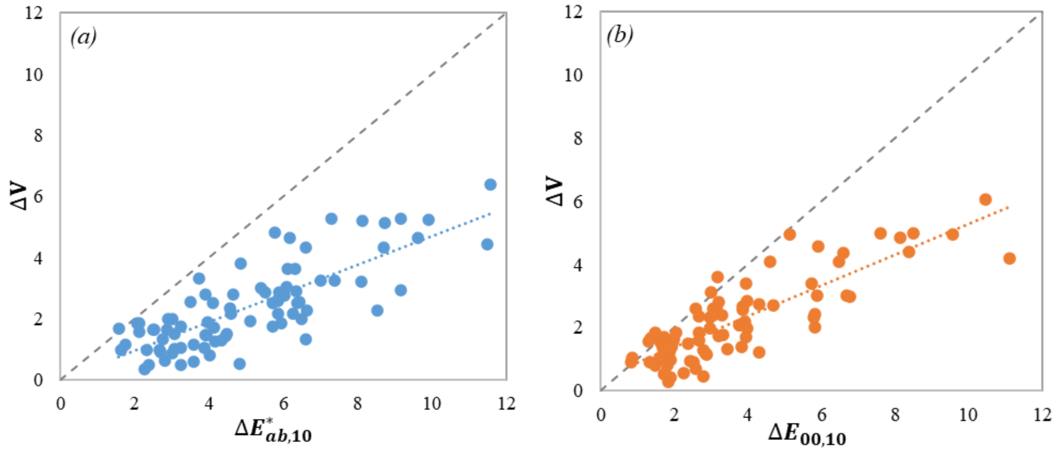

Figure 6.11. Plots of ΔV against $\Delta E^*_{ab,10}$ (a) and $\Delta E_{00,10}$ (b) for the 82 sample pairs in the VeriVide viewing cabinet.

Considering that the whole colour differences of the 42 sample pairs in Sample Set I were produced mainly from one of the three colour attributes, lightness, chroma and hue, the visual results were divided and analysed according to these three components. Figure 6.12 (left) shows the plots of the visual data of the 42 sample pairs in Sample Set I against ΔL^*_{10}, $\Delta C^*_{ab,10}$, $\Delta H^*_{ab,10}$ and three linear lines fitted for lightness, chroma and hue differences, respectively. Figure 6.12 (right) plots ΔV against the CIEDE2000 weighted ΔL_{00} , ΔC_{00} , ΔH_{00} which were calculated using the equations proposed by Nobbs (2006).

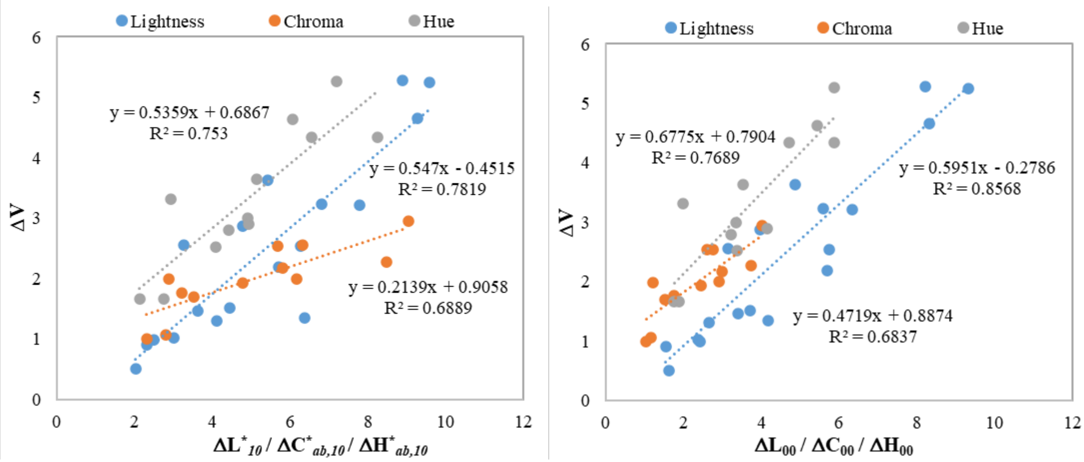

Figure 6.12 Plots and correlations of ΔV against $\Delta L^*_{10}, \Delta C^*_{ab,10}, \Delta H^*_{ab,10}$ (a) and $\Delta L_{00}, \Delta C_{00}, \Delta H_{00}$ (b) of the 42 sample pairs in Sample Set I.

As can be seen from Figure 6.12 (left), the relationships between the visual colour differences and the calculated in the three components of $\Delta E^*_{ab,10}$ were approximately linear, and the linear line fitted for hue differences is above the other two lines, indicating that the perceived hue differences are more distinct than the perceived lightness differences for a given $\Delta E^*_{ab,10}$. It is indicated that the human visual system is more sensitive to hue changes than to lightness changes in CIELAB. In comparison, the slope of the fitted chroma-difference line as well as its R^2 value are smaller than those of lightness and hue-difference fitted lines, indicating that the sensitivity to the perceived chroma changes for 3D objects is relatively lower.

In addition, the CIELAB lightness, chroma and hue differences of the 42 pairs are almost in the same range, from 2 to 10 units. The perceived visual colour differences, however, have different ranges for these three components, which are approximately 1.0-3.0 units for chroma differences, 0.5-5.5 units for lightness differences, and 1.5-5.5 units for hue differences. Therefore, the factors related to these three colour components in the colour-difference formula should be rescaled for 3D colour objects.

Regarding the results of CIEDE2000 as shown in Figure 6.12 (right), similar findings were achieved for lightness and hue-difference predictions, while a major difference was found for predicting chroma differences: the CIEDE2000 weighted ΔC_{00} is much closer to the visual data compared to the results of CIELAB. This confirmed that CIEDE2000 colour-difference formula performed chroma correction on CIELAB formula and a significant improvement was achieved.

6.3.3 Testing Colour-Difference Formulae

The performance of the CIELAB and CIEDE2000 colour-difference formulae was tested using the visual data of the 82 pairs of samples, and the average $STRESS$ values obtained were 30.5 CIELAB units and 29.2 CIEDE2000 units. This result indicates that CIEDE2000 has a slightly better performance than CIELAB for colour-difference prediction of 3D samples, which is in line with the results shown in in Figure 6.11.

In order to investigate the performance of CIELAB and CIEDE2000 formulae on predicting lightness, chroma and hue differences, the $STRESS$ values and the ratios of $\Delta E/\Delta V$ were calculated for the 42 pairs in Sample Set I, and the results are shown in Tables 6.1 and 6.2, respectively. It was assumed that the ratio should be equal to 1.0 for a perfect agreement between the predictions of a colour-difference formula and the visual results collected from psychophysical experimental.

Table 6.1 shows that the $STRESS$ values in CIEDE2000 units are smaller than those in CIELAB units for lightness-difference pairs and hue-difference pairs, but not for chroma-difference pairs, which is quite surprising. It can be seen that the $STRESS$ values achieved for hue differences are the smallest compared to lightness and chroma, it is indicated that the colour-difference formulae predict hue differences accurately. Regarding the results in Table 6.2, the average ratios of $\Delta E/\Delta V$ achieved using the two colour-difference formulae are larger than 1.0. The ratios calculated for hue differences are the closest to 1.0 and this is in agreement with the smallest $STRESS$ values shown in Table 6.1. It is therefore concluded that the tested colour-difference formulae have better performance for predicting hue differences than for lightness and chroma differences.

Table 6.1 The $STRESS$ values in CIELAB and CIEDE2000 units of the 42 pairs with predominant (≥85%) lightness, chroma and hue-differences.

	42 pairs	ΔL^*_{10} pairs	$\Delta C^*_{ab,10}$ pairs	$\Delta H^*_{ab,10}$ pairs
CIELAB	28.6	23.7	21.7	17.7
CIEDE2000	25.9	18.9	23.3	15.6

Table 6.2 Basic statistical results of $\Delta\mathrm{E}/\Delta\mathrm{V}$ ratios of the 42 pairs with predominant (≥85%) lightness, chroma and hue-differences.

	ΔL^*_{10} pairs		$\Delta C^*_{ab,10}$ pairs		$\Delta H^*_{ab,10}$ pairs	
	$\Delta E^*_{ab}/\Delta\mathrm{V}$	$\Delta E_{00}/\Delta\mathrm{V}$	$\Delta E^*_{ab}/\Delta\mathrm{V}$	$\Delta E_{00}/\Delta\mathrm{V}$	$\Delta E^*_{ab}/\Delta\mathrm{V}$	$\Delta E_{00}/\Delta\mathrm{V}$
Min	1.38	1.38	1.51	0.79	1.12	0.96
Max	4.91	4.37	3.76	1.99	2.19	1.59
Mean	2.66	2.41	2.63	1.44	1.63	1.26
STD	0.92	0.71	0.60	0.39	0.28	0.19

For the visual results of the same 82 pairs of 3D samples collected in the X-Rite light booth with a D65 simulator, the average $STRESS$ values achieved are given in Table 6.3, which are larger than the results obtained in the VeriVide standard viewing cabinet, even for the stationary 3D sample pairs. It is not surprising that the visual colour differences reported by observers for the rotated 3D sample pairs gave greater $STRESS$ values (39.5 CIELAB units and 42.6 CIEDE2000 units), because the experiment did not meet the reference viewing conditions (given in Table 2.1) for visual colour-difference evaluation recommended by CIE. The reason that the $STRESS$ values acquired for the 82 pairs of 3D samples in the X-Rite light booth were greater than in the VeriVide viewing cabinet may be due to the use of the two different simulated D65 illuminations.

Table 6.3 The $STRESS$ values in CIELAB and CIEDE2000 units of the 82 pairs of 3D samples in the X-Rite light booth.

	$STRESS$ in ΔE^*_{ab}	$STRESS$ in ΔE_{00}
Rotate	39.5	42.6
Still	36.7	36.8

6.4 Optimisation of CIELAB and CIEDE2000

6.4.1 Optimisation Methods

Most current advanced colour-difference formulae were derived by modifying the CIELAB formula which was defined as a Euclidean distance in terms of lightness, chroma and hue differences between the two stimuli (Luo et al 2001), and the generic equation is expressed:

$$\Delta E = \sqrt{\left(\frac{\Delta L^*_{10}}{k_L S_L}\right)^2 + \left(\frac{\Delta C^*_{ab,10}}{k_C S_C}\right)^2 + \left(\frac{\Delta H^*_{ab,10}}{k_H S_H}\right)^2 + \Delta R}, \tag{6.3}$$

where $\Delta L^*_{10}, \Delta C^*_{ab,10}, \Delta H^*_{ab,10}$ are the CIELAB metric lightness, chroma and hue difference, k_L, k_C, k_H and S_L, S_C, S_H are the three parametric factors and weighting functions for lightness, chroma and hue difference, respectively, ΔR is an interactive term between chroma and hue difference.

In CIELAB formula, $k_L, k_C, k_H, S_L, S_C, S_H$ were all set as 1 and $\Delta R = 0$. For CIEDE2000, S_L, S_C, S_H are three specified weighting functions, ΔR is related to the so-called rotation term affecting the blue saturated region of colour space, and $k_L = k_C = k_H = 1$ under so-called 'reference conditions' for most applications ($k_L = 2$, $k_C = k_H = 1$ for textiles). In order to better agree with visually perceived colour differences, Huang et al. (2015) reported that colour-difference formulae can be modified by applying power correction.

Since the colour appearance of 3D objects may be affected by more factors than for 2D objects, it is hypothesised that the factors in colour-difference formulae should be different for these two situations. To improve the predictions of CIELAB and CIEDE2000 colour-difference formulae for 3D printed spherical objects, the optimisation on parametric factors were performed and the power correction was applied. In a nutshell, the following three optimisation methods were adopted:

- Method 1: Optimise k_L with $k_C = k_H = 1$.
- Method 2: Optimise both k_L and k_C with $k_H = 1$.

- Method 3: Apply a power function and optimise the exponent n (i.e., $\Delta E' = \Delta E^n$).

The combination of parametric factor optimisation with application of power functions was also considered as an optimisation method, i.e., Method 1+3 and Method 2+3. The goal of the optimisations was to minimize the $STRESS$ value between the visual results and the values calculated using a colour-difference formula, by using the GRG nonlinear method in Excel Solver or the *fminsearch* function in MATLAB.

6.4.2 Optimisation Results

The visual colour-difference data of the 42 pairs of 3D samples in Sample Set I were used to optimise CIELAB and CIEDE2000 formulae, and the optimised factors for CIELAB and CIEDE2000 using different methods are given in Table 6.4. Table 6.5 presents the $STRESS$ values calculated using the original and the optimised CIELAB and CIEDE2000 formulae. In order to analyse the statistical significances between the original and the optimised colour-difference formulae, the F-test was performed using the Equation (2.41) described in Section 2.6.3. The degrees of freedom were 41 (N=42), and the critical value F_C is 0.54 ($1/F_C = 1.86$) for the two-tailed F-distribution with a 95% confidence level. Table 6.6 gives the F-test results for the optimised CIELAB and CIEDE2000 formulae, the bold numbers indicate cases with statistically significant improvements.

By using Method 1 which was to optimise the k_L factor with $k_C = k_H = 1$, the optimal k_L factor for CIELAB colour-difference formula is 1.1 and the corresponding $STRESS$ value is 28.5, which is similar to the $STRESS$ value of 28.6 calculated using the original formula ($k_L = k_C = k_H$ =1). Therefore, the improvement in performance of the optimised CIELAB colour-difference formula with $k_L = 1.1$ is negligible. In comparison, the optimal k_L factor for CIEDE2000 is 1.5 and the $STRESS$ value reduced from 25.9 to 18.8 units, indicating better performance was achieved. Furthermore, the corresponding F-test value is 0.53, as shown in Table 6.6, smaller than the critical value (F_C = 0.54). It is indicated that the optimised CIEDE2000 formula with k_L=1.5 is significantly better than the original formula.

Based on Method 2 for optimising both k_L and k_C simultaneously with k_H = 1, the optimal k_L and k_C factors for CIELAB are 1.4 and 1.9, respectively, and the calculated $STRESS$ value decreased from 28.6 to 20.5 CIELAB units. Furthermore, the corresponding F-test value is 0.51, smaller than the F_C value of 0.54, showing that the optimisation of the CIELAB formula with k_L =

1.4 and k_C = 1.9 has significantly better performance than the original CIELAB formula. For the results of the optimised CIEDE2000 with k_L = 1.6 and k_C = 1.1, significantly better performance was also achieved compared to the original CIEDE2000 formula, with the $STRESS$ value decreasing from 25.9 to 18.6 CIEDE2000 units and the F-test value of 0.52. In addition, the optimisation results of CIEDE2000 using Method 1 (k_L = 1.5, $k_C = k_H = 1$) and Method 2 (k_L = 1.6, k_C = 1.1, $k_H = 1$) are very similar, because the S_C function in CIEDE2000 has already corrected the CIELAB chroma difference values (Luo et al. 2001). In comparison, the optimisation for the k_C factor achieved better performance for CIELAB.

Table 6.4 The parametric factors optimised for CIELAB and CIEDE2000 formula using different methods.

Method	CIELAB	CIEDE2000
Original	$k_L = k_C = k_H = 1$	$k_L = k_C = k_H = 1$
Method 1	$k_L = 1.1, k_C = k_H = 1$	$k_L = 1.5, k_C = k_H = 1$
Method 2	$k_L = 1.4, k_C = 1.9, k_H = 1$	$k_L = 1.6, k_C = 1.1, k_H = 1$
Method 3	$n = 0.9$	$n = 0.8$
Method 1+3	$k_L = 1.1, k_C = k_H = 1$ $n = 1$	$k_L = 1.6, k_C = k_H = 1$ $n = 1$
Method 2+3	$k_L = 1.4, k_C = 1.9, k_H = 1$ $n = 1$	$k_L = 1.6, k_C = 1.2, k_H = 1$ $n = 0.9$

Table 6.5 The $STRESS$ values calculated using the original and the optimised CIELAB and CIEDE2000 formulae.

	Original	Method 1	Method 2	Method 3	Method 1+3	Method 2+3
CIELAB	28.6	28.5	20.5	28.5	28.4	20.5
CIEDE2000	25.9	18.8	18.6	24.8	18.7	18.4

Table 6.6 The F-test results for the optimised CIELAB and CIEDE2000 formulae.

	Method 1	Method 2	Method 3	Method 1+3	Method 2+3
CIELAB	0.99	**0.51**	1.00	0.99	**0.51**
CIEDE2000	**0.53**	**0.52**	0.92	**0.52**	**0.51**

With respect to the consequences of applying a power function to the original colour-difference formulae (Method 3), the obtained $STRESS$ values of the optimised CIELAB and CIEDE2000 formulae are 28.5 and 24.8 units, respectively, and the F-test values are close to 1, which suggested that there was no significant improvement achieved. When the power function was applied to the optimised colour-difference formulae, named as Method 1+3 and Method 2+3 in Tables 6.5 and 6.6, the results similar to those from Method 1 and Method 2 were obtained. This means that applying a power function gives almost no improvement on the optimisation of colour-difference formulae for 3D samples.

Given the 3D sample pairs in Sample Set I can be divided into three groups: those with predominant (≥85%) lightness differences, chroma differences and hue differences, the visual data of these three groups of 3D sample pairs were used to optimise the k_L, k_C, k_H parametric factors, respectively. The optimisation results and corresponding $STRESS$ values for CIELAB and CIEDE2000 are listed in Table 6.7. The k_L factors (1.8 and 1.6) optimised for the two formulae are larger than the default value of 1.0, indicating that lightness differences in the original formulae were over-valued for 3D samples (see Equation (6.3)). The optimal values for the k_C factor were totally different for CIELAB and CIEDE2000 formulae, i.e., k_C=1.4 was determined for CIELAB while k_C=0.5 for CIEDE2000, and an opposite circumstance happened for the optimisation of k_H factor, the optimal k_H is 0.5 for CIELAB while 1.1 for CIEDE2000.

Compared to the results calculated using the original formulae, as shown in Table 6.1, the $STRESS$ values become smaller after individual factor optimisation, but the disparity is not great. This implies that the approach to separately optimise the parametric factors did not yield significantly improvement.

Table 6.7 The individual optimised k_L, k_C, k_H factors and corresponding $STRESS$ values (in parentheses) for CIELAB and CIEDE2000.

	ΔL^*_{10} pairs	$\Delta C^*_{ab,10}$ pairs	$\Delta H^*_{ab,10}$ pairs
CIELAB	k_L=1.8 (23.3)	k_C=1.4 (21.6)	k_H=0.5 (16.7)
CIEDE2000	k_L=1.6 (18.3)	k_C=0.5 (21.3)	k_H=1.1 (15.5)

6.4.3 Validation

In addition to reporting the results of the optimised colour-difference formulae using the same 42 pairs of 3D samples in Sample Set I, the collected visual colour-difference data of the 40 pairs of 3D samples in Sample Set II were used to validate the performance of the optimised colour-difference formulae. The calculated $STRESS$ values are shown in Table 6.8, and Table 6.9 gives the F-test results of the optimised formulae with respect to the original ones. The degrees of freedom are 39 (N =40), and the critical value F_C is 0.53 ($1/F_C = 1.89$) for the two-tailed F-distribution with a 95% confidence level.

Table 6.8 The $STRESS$ values of the original and the optimised colour-difference formulae, validated using the 40 sample pairs.

	Original	Method 1	Method 2	Method 3	Method 1+3	Method 2+3
CIELAB	32.8	32.6	25.3	33.1	33.0	25.3
CIEDE2000	32.9	26.0	25.4	31.2	26.0	25.1

Table 6.9 The F-*test* values of the optimised colour-difference formulae, validated using the 40 sample pairs.

	Method 1	Method 2	Method 3	Method 1+3	Method 2+ 3
CIELAB	0.99	0.59	1.02	1.01	0.59
CIEDE2000	0.62	0.60	0.90	0.62	0.58

It is noticeable in Table 6.8 that the $STRESS$ value decreased from 32.8 to 25.3 units, which was achieved using Method 2 and Method 2+3 to optimise CIELAB formula. In the light of the improvement, the recommended factors for CIELAB are $k_L = 1.4, k_C = 1.9$. For the optimisation of CIEDE2000, the Method 1 (1+3) and Method 2 (2+3) gave similar $STRESS$ values between 25.1 and 26.0 units, and the k_L factor is 1.5 for Method 1 and $k_L = 1.6$ for Method 2. The effect produced by optimising k_C factor in CIELAB is not significant in CIEDE2000, because the weighting function for chroma (S_C) was applied to CIEDE2000. The results showed that the k_L optimised factors are useful for CIELAB and in CIEDE2000 formulae. Furthermore, the corresponding F-test values in Table 6.9 indicate that the performance of the optimised colour-difference formulae was greatly improved. Additionally, the application of power correction (Method 3) did not provide better performance for the optimisation of colour-difference formulae.

The visual colour-difference data collected from the 82 pairs of 3D sample in the X-Rite light booth were used to validate the predictive performance of the optimised colour-difference formulae, CIELAB with $k_L = 1.4, k_C = 1.9$ and

CIEDE2000 with $k_L = 1.5$. The $STRESS$ values achieved using the optimised formulae are given in Table 6.10. Compared to the results calculated using the original CIELAB and CIEDE2000 formulae, as listed in Table 6.3, the $STRESS$ values in Table 6.10 are all smaller because of the optimisation on the colour-difference formulae, even for the rotated 3D samples. Consequently, it was confirmed that the optimised parametric factors in CIELAB and CIEDE2000 formulae are valid and useful for predicting colour differences of 3D printed samples.

Table 6.10 The $STRESS$ values in the optimised CIELAB and CIEDE2000 units of the 82 pairs of 3D samples in the X-Rite light booth.

	Optimised CIELAB	Optimised CIEDE2000
Rotate	31.7	33.9
Still	32.2	30.8

Additionally, the collected visual data of the 3D samples with skin tones were also used to validate the performance of the optimised colour-difference formulae. The $STRESS$ value calculated using the original CIELAB formula was 18.4, and it decreased to 12.5 by using the optimised CIELAB with $k_L = 1.4, k_C = 1.9$. Similarly, the $STRESS$ value calculated using the optimised CIEDE2000 with $k_L = 1.5$ was 11.6 units, compared to the value of 16.0 calculated using the original CIEDE2000 formula. To sum up, after tested using different 3D samples sets including skin tones, the optimisation of colour-difference formulae for 3D objects achieved significant improvements.

6.5 Discussion

This study was conducted to investigate the human visual colour system of 3D printed samples in perceiving lightness, chroma and hue differences, and to optimise the CIELAB and CIEDE2000 colour-difference formulae based on the visual results collected from psychophysical experiments. It was found that it is generally easier to assess hue differences of 3D spherical objects but not chroma differences, and the results indicated that the parametric factors related to lightness differences, chroma differences and hue-differences in colour-difference formulae should be optimised for 3D objects.

Among the three methods used for optimisation, the best performance achieved for CIELAB was to optimise both the k_L and k_C parametric factors. The optimal k_C factor (1.9) is larger than the optimal k_L factor (1.4), indicating that the original CIELAB formula predicted a larger difference for the chroma dimension than for the lightness dimension. Moreover, both optimised factors are larger than the original values of 1.0, suggesting that the difference scale should be compressed for 3D objects in the CIELAB colour-difference formula. In addition, the method to optimise only the k_L factor gives little improvement to CIELAB, which is quite different from the CIEDE2000 formula.

The optimal k_L parametric factor for the optimised CIEDE2000 is 1.5, larger than the default value of 1.0, indicating that the visual lightness difference of 3D objects is over-estimated by the original formula($k_L = 1$) which was developed based on 2D samples with homogeneous surfaces under reference conditions. It is suggested that human colour perception of 3D objects is different from 2D objects, concerning that 3D objects have non-flat surfaces. The parametric factors in colour-difference formulae have been modified to improve the prediction performance in different applications. In the textile industry, it is common practice to set the lightness parametric factor to 2 (CIE 2001), allowing for the associated texture effect. Huertas et al. (2006) investigated the three parametric factors based on simulated random-dot textures, suggesting values which were always larger than 1.0; Liu et al. (2013) proposed k_L= 2.3 for assessing colour differences in digital images; Mirjalili et al. (2019) concluded that optimising the lightness parametric factor, k_L, resulted in an improvement in the performance of the CIEDE2000 formula. Therefore, it is crucial to develop a colour-difference formula for 3D objects.

In comparison to the optimisation of parametric factors, the power function had no evident improvement over the original formulae in this study. A possible reason for this is that the 3D sample pairs used in the current visual experiments had small to medium colour differences ranging from 2 to 9 CIELAB units. In the study of Jiang et al. (2021), a remarkable improvement was achieved by adding a power correction in predictions of colour differences between 3D objects in a range of 25 CIELAB units, and it was reported that colour-difference magnitude had more effect on the perceived colour differences of 3D objects than sample shape or illumination. Therefore, a power function is possibly more suitable for sample pairs with magnitudes in a very large range of colour differences.

6.6 Summary

In this chapter, psychophysical experiments with the grey scale method were conducted to assess colour differences of 3D printed spherical samples. The visual colour-difference results indicate that the human visual colour system of 3D objects is different in perceiving lightness, chroma and hue differences, and the factors related to these three components in colour-difference formulae need to be optimised for 3D objects.

By applying different optimisation methods to CIELAB and CIEDE2000 formulae, the $STRESS$ value of the 42 sample pairs decreased from 28.6 to 20.5 units by simultaneously optimising both the k_L and k_C factors in CIELAB. Regarding the validation results based on the 40 sample pairs, considerable improvement was achieved for the optimised CIELAB with k_L=1.4 and k_C=1.9, and the $STRESS$ value achieved was 25.3 units, smaller than the value of 32.8 calculating using the original CIELAB formula. For the optimisation of the CIEDE2000 colour-difference formula, k_L =1.5 is recommended for 3D spherical objects, and the $STRESS$ value of the validation decreased by 7 units compared with the results from the original formula (k_L=1).

In addition, it was found that power functions do not improve predictions of visual results, because the colour differences of 3D samples used in the present study were in small and medium magnitudes (less than 10 CIELAB units).

Chapter 7
Implementation of 3D Colour Reproduction of a Human Face

Based on the 3D colour image reproduction workflow for human faces introduced in Chapter 3 and the colour characterisation methods developed for the 3D imaging system (Section 4.6) and the colour 3D printer (Section 5.2), a practice of reproducing the colour appearance of a human face was described in this chapter, from 3D image acquisition to 3D printing with colour characterisation models applied. In addition, the colour quality of the reproduced 3D face model was evaluated using the optimised colour-difference formulae presented in Section 6.4.

7.1 3D Image Acquisition

The 3dMDface system introduced in Section 3.2.1 was utilised to capture the 3D images of a human face. Prior to capturing facial images using this system, a successful calibration procedure was conducted. A Chinese human subject was asked to sit on a chair placed in a specific position that was the same as the calibration plate. The height of the chair was adjusted so that the human face can be shown simultaneously in the three live view windows. The implementation of 3D image acquisition was in a dark room and the built-in flash in the 3dMDface system was the only illumination for 3D image capture. The 3dMDface acquisition software was used to control the 3D imaging system and capture the 3D images of the human face. During the 3D image acquisition, the subject was asked to keep still until the capture is finished.

It is crucial to ensure absence of acquisition errors in 3D models, such as imaging artifacts, blurring, and missing surface data. Any images with these bad characteristics were discarded, and a new image capture was carried out to obtain high-quality 3D images. The speckle projection images and the bitmap images captured from three directions using the 3D imaging system are shown in Figures 7.1 and 7.2, respectively. Figure 7.3 (left) presents the 3D mesh of the human face captured, which requires edge repairs and the removal of unwanted parts, and Figure 7.3 (right) presents the 3D face model with colour appearance, achieved by projecting the bitmap images onto the 3D mesh model.

Figure 7.1 The speckle projection images captured from different directions using the 3dMDface system.

Figure 7.2 The bitmap images captured from different directions using the 3dMDface system.

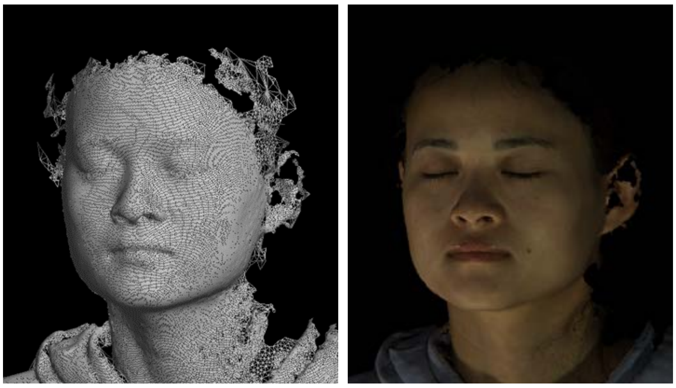

Figure 7.3 The captured 3D face model without (left) and with (right) the bitmap image mapped.

7.2 3D Mesh Manipulation

From Figure 7.3 (left), it can be seen that the original 3D mesh exhibits rough edges and a large number of sparse and discontinuous vertices and faces. As a result, it is necessary to modify the 3D mesh by adding and deleting vertices, edges and faces to smooth and refine the surface. Additionally, while the 3D model captured using the 3dMDface system provides a comprehensive coverage of the human face, ranging from left ear to right ear, it lacks certain details of the back of the head, resulting in gaps of holes that prevent it from being closed and watertight.

The Blender software (Blender 2.90.1, Blender, Amsterdam, Netherlands) was used to manipulate the 3D mesh. Firstly, the object file created using the 3dMDface system was imported to Blender, and the selection tool was employed to choose the areas other than the face, such as the neck and hair, and the unwanted mesh was deleted. The next step was to add a plane to close the back of the 3D mesh, using the Solidity and Boolean Modifier tool provided by the software. Afterwards, the superfluous components were eliminated to create a smoother edge and achieve a solid and clean 3D model. The final step was to check if the 3D model is watertight and feasible for 3D printing, using the Clean Up tool in Blender. Figure 7.4 shows the 3D mesh model of the face after manipulation, which is workable for 3D printing.

Figure 7.4 The manipulated 3D mesh model of the human face workable for 3D printing.

7.3 Colour Management

Based on the colour characterisation model developed for the 3D imaging system in Section 4.6, the bitmap image of the human face was converted from the 3D camera RGB colour space to a device-independent CIE XYZ colour space. Figure 7.5 (left) shows the corrected bitmap image after performing colour characterisation, and Figure 7.5 (right) presents the original bitmap captured using the 3dMDface system.

Figure 7.5 The corrected bitmap image (left) using the colour characterisation model of the 3D cameras, in comparison to the original bitmap (right).

A CM700d spectrophotometer with a SAV 3 mm aperture and SCI mode was used to measure the colours at four facial areas (FH, CBR, CBL, CH), which was carried out immediately after 3D image acquisition. The colour accuracy of the 3dMDface system was quantified by calculating the colour differences between the skin colour data predicted from the bitmap image using the colour characterisation model and the instrumental measurements of the actual human face. The average colour difference achieved for this subject was 2.45 CIELAB units (1.88 CIEDE2000 units), indicating good accuracy of colour reproduction of the 3D cameras, particularly compared to the original value of 32.26 CIELAB units (31.94 CIEDE2000 units) without performing camera colour characterisation. Table 7.1 gives the CIELAB and CIEDE2000 colour differences calculated for each facial location. The colour difference in the chin area appeared to be slightly greater than in the other three facial regions, this is possibly because the chin area is not as flat as the forehead and cheek areas.

Table 7.1 The measurement accuracy of the 3D imaging system for each facial location.

	FH	CBR	CBL	CH	Mean
CIELAB	1.72	2.58	2.42	3.07	2.45
CIEDE2000	1.72	1.53	1.72	2.56	1.88

In order to faithfully print the desired skin colours, a reverse colour characterisation model was developed for the colour 3D printer in Section 5.2, calculating the input colour values from the output colours. The corrected bitmap image in CIE XYZ colour space was then converted to the printer RGB colour space for achieving accurate and consistent colour reproduction by using the colour characterisation model established for the Stratasys J750 colour 3D printer.

7.4 3D Printing

The processed bitmap image in the printer RGB colour space instead of the original bitmap was projected onto the manipulated 3D mesh model by applying the Image Texture tool in Blender. Apart from texture mapping, no other modifications were made to the colour appearance of the 3D face model. Figure 7.6 (left) shows the desired 3D colour face model in Blender. The GrabCAD Print software was employed to send the ready 3D face model to the Stratasys J750 3D colour printer without changing the colour appearance. A high mix printing mode were selected for reproducing the face model. Figure 7.6 (right) presents the process of 3D printing the face model, which has a support material covering the outer surface of the 3D model to achieve a matte finish.

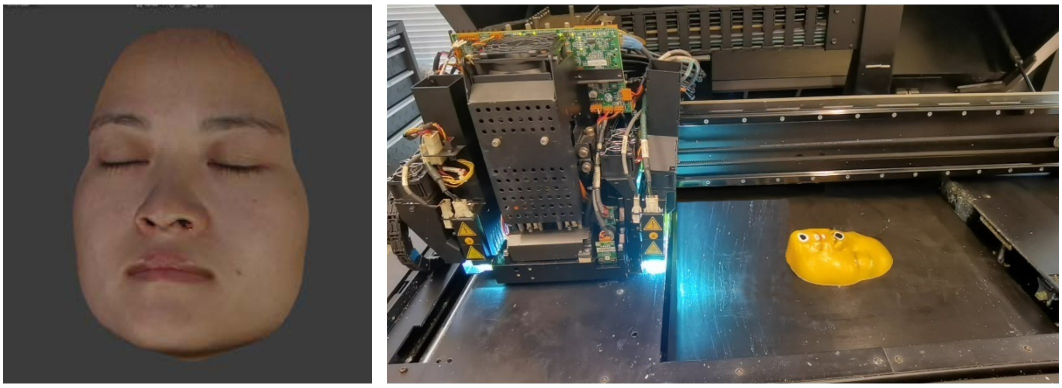

Figure 7.6 The digital 3D face model (left) and the process of 3D printing (right).

7.5 Postprocessing

When the 3D printing process is finished, the 3D face model was carefully removed from the build tray of the 3D printer and put into a waterjet system, as shown in Figure 7.7 (left). The support material was rinsed off under the high-pressure stream of the waterjet. Alternatively, it can be stripped manually and cleaned under water. Figure 7.7 (right) displays the printed 3D face model after postprocessing.

Figure 7.7 The printed 3D model in a waterjet system (left) and the face model after removing the support material.

7.6 Colour Reproduction Evaluation

A CM700d spectrophotometer with a small aperture and SCI condition was used to measure the colour of each of the four facial locations, and the colour differences between the measurement data of the actual human face and the results measured on the 3D printed face model were calculated and used quantify the accuracy of the 3D colour reproduction workflow. Table 7.2 gives CIELAB and CIEDE2000 colour-difference values of each facial location under CIE illuminant D65. The average colour difference achieved for the 3D printed face is 5.73 CIELAB units and 3.88 CIEDE2000 units, which indicates a large improvement in colour accuracy, compared to the value of 17.98 CIELAB units (16.81 CIEDE2000 units) without applying colour characterisation for the 3D printer. In addition, the two cheek areas presented slightly smaller colour differences, then followed by the results achieved in the forehead area. The largest colour difference occurred in the chin area, the same to the accuracy results of the 3D imaging system. This is likely concerning to the curvature of the chin area, resulting in darker tones in the captured image.

Table 7.2 The colour reproduction accuracy of the 3D printed face model for each facial location.

	FH	CBR	CKL	CH	Mean
CIELAB	6.87	3.95	2.87	9.21	5.73
CIEDE2000	4.53	2.66	1.86	6.46	3.88

In Section 6.4, the parametric factors in colour-difference formulae were optimised for evaluating the colour differences of 3D spherical objects, and the optimal factors k_L=1.4 and k_C=1.9 are recommended for CIELAB, and k_L=1.5 for CIEDE2000 (the default factors $k_L = k_C = k_H = 1$). These two optimised colour-difference formulae are named CIELAB-3D and CIEDE2000-3D, respectively, and expressed as:

$$\text{CIELAB -3D} = \sqrt{(\frac{\Delta L^*}{1.4})^2 + (\frac{\Delta C^*_{ab}}{1.9})^2 + (\Delta H^*_{ab})^2} \tag{7.1}$$

$$\text{CIEDE2000-3D} = \sqrt{\left(\frac{\Delta L'}{1.5S_L}\right)^2 + \left(\frac{\Delta C'}{S_C}\right)^2 + \left(\frac{\Delta H'}{S_H}\right)^2 + R_T\left(\frac{\Delta C'}{S_C}\right)^2\left(\frac{\Delta H'}{S_H}\right)^2} \tag{7.2}$$

The colour accuracy of the 3D printed face was evaluated using the CIELAB-3D and CIEDE2000-3D colour-difference formulae, and the results obtained are illustrated in Figure 7.8 with the colour differences calculated using the original formulae. It can be clearly seen that the optimised formulae gave smaller colour-difference values than the original CIELAB and CIEDE2000 formulae. This is concerning to that the optimisation was performed using the visual colour-difference data of 3D objects, even though only spherical samples were involved, while current CIELAB and CIEDE2000 formulae were developed based on 2D samples.

The average colour difference calculated using CIELAB-3D was 3.75, with 2 units reduced in comparison to the value of 5.73 produced using CIELAB. For the performance of CIEDE2000-3D, the colour-difference value decreased from the original value of 3.88 to 3.42 units. According to the colour difference thresholds reported by Paravina et al. (2009), these colour-difference values of the 3D printed face model are acceptable for skin colour reproduction.

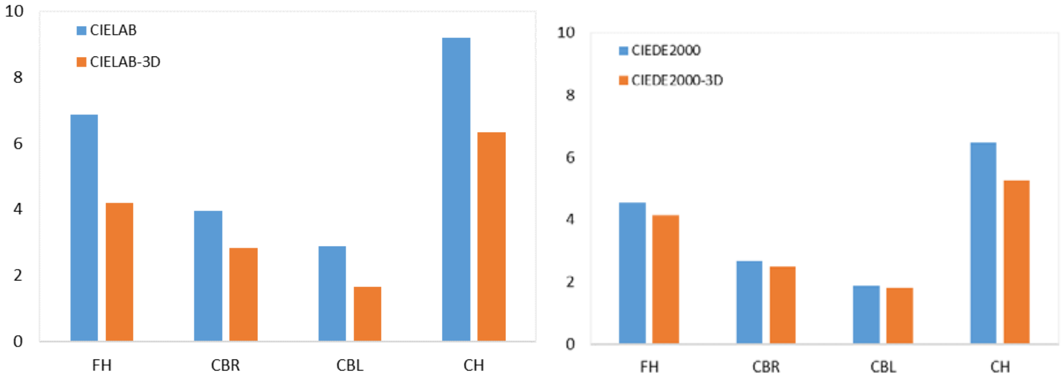

Figure 7.8 Colour differences between the 3D printed face model and the actual human face.

7.7 Discussion

The colour reproduction of a Chinese woman face was implemented in practice, from 3D colour image acquisition, colour management, colour 3D printing to colour quality evaluation. The average colour differences achieved for the 3D printed face model were 5.73 CIELAB units and 3.88 CIEDE2000 units, and the colour-difference values produced for the forehead and cheek areas were 4.53 and 2.26 (the average for both cheeks) CIEDE2000 units, respectively. In the study conducted by Sohail et al. (2018) to evaluate colour quality of 3D printed facial prostheses, the average colour difference of the forehead areas of two Chinese subjects was 7.15 CIEDE2000 units (8.2 and 6.1 units, respectively), and the CIEDE2000 values were 8.9 (8.4 and 9.4 units, respectively) for the cheek area. In comparison, the results attained in this study has demonstrated a significant improvement in colour accuracy of skin colour reproduction using 3D printing technology.

In this study, a specific skin colour chart instead of a conventional colour chart was applied to the colour characterisation processes for the 3D imaging system and the colour 3D printer to improve the accuracy of skin colour reproduction. Cheung et al. (2004) stated that better results would be achieved when using the colour samples which exhibit similar statistical properties to the target to characterise a camera. Considering that the colour of skin varies between different ethnicities (4.3 to 6.2 in CIELAB units reported by Xiao et al. 2017), a skin colour chart specifically developed for the Chinese group was selected in the 3D colour reproduction of a Chinese women face, and the results indicate that better colour accuracy was achieved for reproducing Chinese facial skin colour.

Regarding the colour difference thresholds for the reproduced skin colour samples, Paravina et al. (2009) conducted visual colour assessments for the skin-coloured maxillofacial elastomers in light and dark tones, and it was found that the perceptibility and acceptability thresholds for dark specimens were significantly higher than light specimens in both CIELAB and CIEDE2000. The perceptibility and acceptability thresholds for light specimens were 1.1 and 3.0 CIELAB units (0.7 and 2.1 CIEDE2000 units), respectively, while the results for dark specimens were 1.6 and 4.4 CIELAB units (1.2 and 3.1 CIEDE2000 units), respectively.

Despite that there is no systematic method to assess the colour fidelity and quality of the facial prostheses, achievement of colour consistency and good colour match is a practical requirement for reproducing skin colour samples using 3D printing. In previous studies, the accuracy of a 3D colour image reproduction system was typically evaluated by printing some specific colours. For example, Xiao et al. (2013) used 14 testing skin colours to assess the performance of the colour reproduction, and the colour differences calculated under CIE illuminant D65 were 2.5 to 11.1 CIELAB units with an average value of 4.5. Liu et al. (2019) evaluated the developed 3D colour reproduction system using tooth and gum shades, and the achieved CIELAB colour difference values ranged from 2.19 to 11.22 units, and the mean value was 6.54. Fewer studies have focused on colour reproduction evaluation for practical applications in 3D printing.

In order to evaluate colour quality of facial prostheses in additive manufacturing, Sohail et al. (2018) reported large differences between the 3D and 2D printed facial prostheses which were fabricated using the same colour management procedure. It is possible that good colour accuracy is achieved for 3D printing 2D colour images, but it is not feasible for faithfully reproducing colours in 3D models. Therefore, it is suggested to use 3D samples instead of relying on 2D colour patches, which are commonly used in traditional colour management processes, to evaluate the accuracy of the 3D colour reproduction workflow.

7.8 Summary

In this chapter, the developed 3D colour image reproduction workflow was employed to reproduce the colour appearance of a human face in practice, including the 3D image acquisition, 3D mesh manipulation, colour management, 3D printing, postprocessing and colour evaluation. Based on the specific colour characterisation models, the colour accuracy of the 3dMDface system was reduced from 32.26 to 2.54 CIELAB units (from 31.94 to 2.04 CIEDE2000 units) for capturing the skin colour of a human face, and the precision of the 3D printed face model achieved was 5.73 CIELAB units (3.88 CIEDE2000 units), compared to the skin colour measurements on the actual human face.

Additionally, the CIELAB-3D and CIEDE2000-3D colour-difference formulae, which have been optimised for 3D printed objects, were used to evaluate the colour accuracy of a 3D printed face model. The average colour differences produced by these formulae were 3.75 CIELAB-3D units and 3.42 CIEDE2000-3D units, respectively. These results confirmed the validation and enhancement of the optimised colour-difference formulae for 3D objects, particularly CIELAB. Overall, the accuracy of reproducing human facial skin colour in 3D printing was significantly improved by implementing the proposed colour management and colour evaluation methods within the 3D colour reproduction workflow.

Chapter 8
Conclusions

8.1 Overview of Findings

The aim of the research presented in this thesis was to improve the accuracy of skin colour reproduction of human faces in 3D printing. To achieve this goal, a 3D colour image reproduction workflow was introduced, which involves 3D image acquisition, colour management, colour 3D printing and colour quality assessment. The skin colour data and facial images of human subjects were collected using a spectrophotometer and a specialised digital imaging system. The factors affecting the accuracy of camera colour characterisation were comprehensively investigated, enabling the 3D imaging system to accurately capture facial skin colour images. Moreover, the colour characterisation of a 3D printer was implemented and different approaches were compared to achieve faithful skin colour reproduction. In order to evaluate colour quality of 3D objects, psychophysical experiments were conducted to collect visual colour-difference data of 3D printed samples and the parametric factors in colour-difference formulae were optimised for 3D objects. Based on the developed 3D colour image reproduction workflow, a 3D human face model was printed with realistic skin tones. The major findings and contributions of the research are summarised in the following sections.

8.1.1 Image Measurement

The accurate colour reproduction of a 3D printed object is not only affected by the 3D printer but also the image quality captured using the 3D imaging system. For image-based measurement, the colour characterisation of digital cameras is the basis and key to convert the device-dependent RGB colour space to device-independent CIELAB colour space. In order to investigate the factors such as image formats, training samples and mapping methods that affect the accuracy of camera colour characterisation, a specific 2D digital imaging system was developed to capture colour images of human faces, and a facial skin colour database was collected. The findings are summarised as follows:

- RAW images provided more stable and consistent predictive accuracy than RGB images which resulted in larger variations for different training datasets and mapping methods,

- The actual facial skin colour data used as the training samples gave significant higher accuracy than the conventional ColorChecker SG colour chart for skin colour reproduction,
- Different methods produced the smallest colour difference for different training datasets.

Based on the results of the digital imaging system, a specific skin colour chart and the second-order polynomial regression were utilised to determine the colour characterisation model for the 3dMDface system, and the average colour difference of capturing facial images decreased from 32.71 to 2.90 CIELAB units.

8.1.2 Colour Characterisation for the 3D Printer

To achieve accurate colour reproduction of 3D printed object, different colour characterisation methods for determining a mathematical model that describes the colour behaviour of the 3D printer were investigated and compared, based on a large dataset generated using a Stratasys J750 3D printer. The obtained results showed that the method of deep neural networks gave overall better results (less than 3 CIELAB units and 2 CIEDE2000 units) than the third order polynomial regression, but it is highly dependent on the size of training data, e.g., the optimal and consistent results were produced when the number of training samples was equal to or greater than 1310. In comparison, the training data size had little effect for the third order polynomial regression on the colour characterisation accuracy. Moreover, the logarithms of CIE XYZ rather than CIE XYZ tristimulus values were preferred as the output variables for printer colour characterisation.

In the practical colour characterisation process of the 3D printer, the third order polynomial regression was applied to develop the printer colour characterisation model based on a specific skin colour chart. The average colour difference of 118 skin colour patches was 1.35 CIELAB units, indicating significant improved accuracy of skin colour reproduction, compared to the original value of 7.41 CIELAB units.

8.1.3 Colour-Difference Evaluation

The visual colour-difference data collected from psychophysical experiments showed that the human visual colour system is more sensitive to hue differences of 3D spherical objects, then followed by lightness and chroma differences. Based on the visual results, the parametric factors in CIELAB and CIEDE2000 colour-difference formulae were optimised for 3D objects:

- The factors k_L=1.4 and k_C=1.9 are recommended for CIELAB-3D,
- The factor k_L=1.5 is recommended for CIEDE2000-3D.

Regarding the validation results based on the 40 sample pairs, the $STRESS$ value decreased from 32.8 to 25.3 CIELAB units, and 7 units were reduced for the optimised CIEDE2000 formula.

For the 3D printed face model, the accuracy of skin colour reproduction achieved using the developed methods was 5.73 CIELAB units (3.88 CIEDE2000 units). By using the optimised colour difference formulae, CIELAB-3D and CIEDE2000-3D, the colour differences calculated were 3.75 and 3.42 units, respectively. In generally, the developed 3D colour image reproduction workflow with specific colour characterisation models for the 3D imaging system and the colour 3D printer is capable of achieving higher accuracy of skin tone reproduction of human faces.

8.2 Future Work

Even though the methods of colour management and colour evaluation have been successfully applied to the 3D colour image reproduction workflow with improved accuracy, there are limitations in this work and some areas that need to be further studied:

- The colour characterisation of the 3D printer was based on a skin colour chart particularly developed for Chinese skin tones, other ethnic groups such as Caucasian, Mexican, Indonesian and African can be involved to accurately reproducing different skin tones. In addition, the skin colour chart was printed on the surface of a cuboid as a 2D image, it will be interesting to investigate the difference between the 2D image printing and 3D image printing using the same colour 3D printer.

- The optimisation of CIELAB and CIEDE2000 colour-difference formulae was mainly based on 3D printed spherical samples, other shapes such as cube, cylinder, and cone can be taken into consideration, and more visual colour-difference data of 3D objects need to be collected and used to test the optimised formulae.

- Regarding skin colour reproduction in 3D printing, it is recommended to compare the glossy and matte surface finishes of 3D printed samples and investigate which print mode better matches the actual skin colours.

- In addition to using colour-difference formulae, visual assessments are useful to evaluate the similarity of the 3D printed model compared to the actual human face. A combination of objective measurements and subjective assessments can provide a more comprehensive evaluation on the accuracy of skin colour reproduction.
- In the 3D colour image reproduction workflow, it is important to assess the repeatability and reproducibility of 3D printed objects to ensure the consistency and reliability of the accuracy.

List of References

Alman, D.H., Berns, R.S., Snyder, G.D. and Larsen, W.A. 1989. Performance testing of color-difference metrics using a color tolerance dataset. Color Research & Application, 14(3), pp.139-151.

Amano, K., Xiao, K., Wuerger, S. and Meyer, G. 2020. A colorimetric comparison of sunless with natural skin tan. Plos one, 15(12), p.e0233816.

Angelopoulou, E. 2001. Understanding the color of human skin. Proc. SPIE: Human vision and electronic imaging. 4299, pp.243-251.

ASTM, E1164. 2009. Standard practice for obtaining spectrophotometric data for object-color evaluation, ASTM International, West Conshohocken, PA, USA.

ASTM, E308-17. 2017. Standard practice for computing the colors of objects by using the CIE system, ASTM International, West Conshohocken, PA, USA.

ASTM, F2792-12a. 2012. Standard terminology for additive manufacturing technologies. ASTM International. West Conshohocken, PA, USA.

ASTM, E1808-96R21. 2021. Standard Guide for Designing and Conducting Visual Experiments. Updated July 2021, Published July 1996.

Berns, R.S., Alman, D.H., Reniff, L., Snyder, G.D. and Balonon-Rosen, M.R. 1991. Visual determination of suprathreshold color-difference tolerances using probit analysis. Color Research & Application, 16(5), pp.297-316.

Billmeyer Jr, F.W. and Alessi, P.J. 1981. Assessment of color-measuring instruments. Color Research & Application, 6(4), pp.195-202.

Bloj, M.G., Kersten, D. and Hurlbert, A.C. 1999. Perception of three-dimensional shape influences colour perception through mutual illumination. Nature, 402(6764), pp.877-879.

Brancati, N., De Pietro, G., Frucci, M. and Gallo, L. 2017. Human skin detection through correlation rules between the YCb and YCr subspaces based on dynamic color clustering. Computer Vision and Image Understanding, 155, pp.33-42.

Brill, M.H. and Süsstrunk, S. 2008. Repairing gamut problems in CIECAM02: A progress report. Color Research & Application, 33(5), pp.424-426.

Caisey, L., Grangeat, F., Lemasson, A., Talabot, J. and Voirin, A. 2006. Skin color and makeup strategies of women from different ethnic groups. International journal of cosmetic science, 28(6), pp.427-437.

Chauhan, T., Xiao, K. and Wuerger, S. 2019. Chromatic and luminance sensitivity for skin and skinlike textures. Journal of vision, 19(1), pp.13-13.

Chen, J.R., Morris, J., Wentworth, A., Sears, V., Duit, A., Erie, E., McGee, K. and Leng, S. 2022. Quality assurance and printing accuracy analysis of 3D printing in medical applications. In Medical Imaging 2022: Imaging Informatics for Healthcare, Research, and Applications, SPIE, Vol. 12037, pp. 150-154.

Cheung, M. and Rigg, B. 1986. Colour-difference ellipsoids for five CIE colour centres. Color Research & Application, 11(3), pp.185-195.

Cheung, T.L.V. and Westland, S. 2004. January. Color selections for characterization charts. In Conference on Colour in Graphics, Imaging, and Vision (Vol. 2004, No. 1, pp. 116-119). Society for Imaging Science and Technology.

Cheung, T.L.V., Westland, S., Connah, D.R. and Ripamonti, C. 2004. A comparative study of the characterisation of colour cameras by means of neural networks and polynomial transforms. Journal of Coloration Technology. 120(1), pp.19-25.

Choi, K.M., Kim, S.J., Baek, J.H., Kang, S.J., Boo, Y.C. and Koh, J.S. 2012. Cosmetic efficacy evaluation of an anti-acne cream using the 3 D image analysis system. Skin Research and Technology, 18(2), pp.192-198.

CIE. 1998. The CIE 1997 Interim colour appearance model (simple version), CIECAM97s. CIE Pub. No. 131-1998, CIE Central Bureau, Vienna, Austria.

CIE. 2016. Recommended Method for Evaluating the Performance of Colour-Difference Formulas. CIE Pub. No. 217-2016, CIE Central Bureau, Vienna, Austria.

CIE. 1975. Progress report of CIE TC-1.3 Colorimetry. Compte Rendu 18e Session, Londres. CIE Pub. No. 36-1975, 161-172.

CIE. 1995. Industrial Colour-Difference Evaluation. CIE Pub. No. 116-1995, CIE Central Bureau, Vienna, Austria.

CIE. 1995. Technical report: Industrial colour-difference evaluation. CIE Pub. No. 116-1995, CIE Central Bureau, Vienna, Austria.

CIE. 2001. Improvement to industrial colour-difference evaluation. CIE Pub. No. 142-2001, CIE Central Bureau, Vienna, Austria.

CIE. 2004. A colour appearance model for colour management system: CIECAM02. CIE Pub. No. 159-2004, CIE Central Bureau, Vienna, Austria.

CIE. 2006a. Colorimetry - Part 1: CIE standard colorimetric observer. CIE Central Bureau, Vienna, Austria.

CIE. 2006b. Colorimetry - Part 2: CIE standard illuminants. CIE Central Bureau, Vienna, Austria.

CIE. 2022. The CIE 2016 Colour Appearance Model For Colour Management Systems: CIECAM16. CIE Pub. No. 248-2022, CIE Central Bureau, Vienna, Austria.

Clarke, F. J., MacDonald, R. and Rigg, B. 1984. Modification of the JPC79 Colour-Difference Formula. Journal of the Society of Dyers and Colourists. pp.100-107.

Clarke, F.J., McDonald, R. and Rigg, B. 1984. Modification to the JPC79 colour–difference formula. Journal of the Society of Dyers and Colourists, 100(4), pp.128-132.

Clarys, P., Alewaeters, K., Lambrecht, R. and Barel, A.O. 2000. Skin color measurements: comparison between three instruments: the Chromameter®, the DermaSpectrometer® and the Mexameter®. Skin research and technology, 6(4), pp.230-238.

Coffin, D. 2018. Decoding raw digital photos in Linux. https://www.dechifro.org/dcraw. (valid in March 2023)

Colomb, L., Flament, F., Wagle, A. and Agrawal, D. 2018. In vivo evaluation of some biophysical parameters of the facial skin of Indian women. Part I: variability with age and geographical locations. International Journal of Cosmetic Science, 40(1), pp.50-57.

Cui, G. 2000. Colour-difference evaluation using CRT displays (Doctoral dissertation, PhD Thesis, Derby University).

Cui, G., Luo, M.R., Rigg, B. and Li, W. 2001. Colour-difference evaluation using CRT colours. Part I: Data gathering and testing colour difference formulae. Color Research & Application, 26(5), pp.394-402.

De Rigal, J., Des Mazis, I., Diridollou, S., Querleux, B., Yang, G., Leroy, F. and Barbosa, V.H. 2010. The effect of age on skin color and color heterogeneity in four ethnic groups. Skin Research and Technology. 16(2), pp.168-178.

Del Bino, S. and Bernerd, F. 2013. Variations in skin colour and the biological consequences of ultraviolet radiation exposure. British Journal of Dermatology, 169(s3), pp.33-40.

Espera, A.H., Dizon, J.R.C., Chen, Q. and Advincula, R.C. 2019. 3D-printing and advanced manufacturing for electronics. Progress in Additive Manufacturing, 4, pp.245-267.

Fairchild, M.D., Wyble, D.R. and Johnson, G.M. 2008, January. Matching image color from different cameras. In Image Quality and System Performance V (Vol. 6808, pp. 122-131). SPIE.

Fink, B., Grammer, K. and Matts, P.J. 2006. Visible skin color distribution plays a role in the perception of age, attractiveness, and health in female faces. Evolution and Human Behavior, 27(6), pp.433-442.

Fink, B., Matts, P.J., D'Emiliano, D., Bunse, L., Weege, B. and Röder, S. 2012. Colour homogeneity and visual perception of age, health and attractiveness of male facial skin. Journal of the European Academy of Dermatology and Venereology, 26(12), pp.1486-1492.

Finlayson, G.D., Mackiewicz, M. and Hurlbert, A. 2015. Color correction using root-polynomial regression. IEEE Transactions on Image Processing, 24(5), pp.1460-1470.

Garcia, P.A., Huertas, R., Melgosa, M. and Cui, G. 2007. Measurement of the relationship between perceived and computed color differences. JOSA A, 24(7), pp.1823-1829.

Guan, S., Luo, M.R. 1999. Investigation of parametric effects using small color-differences. Color Res. Appl. 24, 331–343.

Guild, J. 1931. The colorimetric properties of the spectrum. Philosophical Transactions of the Royal Society of London. Series A, Containing Papers of a Mathematical or Physical Character, 230(681-693), pp.149-187.

Hardeberg, J.Y. 2001. Acquisition and reproduction of color images: colorimetric and multispectral approaches. Universal-Publishers.

He, R. 2021. Training and Testing Datasets for skin colour characterisation [Data set]. In Color Research and Application. Zenodo. https://doi.org/10.5281/zenodo.5532176

Hong, G., Luo, M.R. and Rhodes, P.A. 2001. A study of digital camera colorimetric characterisation based on polynomial modelling. Color Research & Application. 26(1), pp.76-84.

Huang, M., Cui, G., Melgosa, M., Sánchez-Marañón, M., Li, C., Luo, M.R. and Liu, H. 2015. Power functions improving the performance of color-difference formulas. Optics Express, 23(1), pp.597-610.

Huang, M., Gao, X., Pan, J., Li, X., Hemingray, C., Xiao, K. and Melgosa, M. 2022a. Optimizing Color-Difference Formulas for 3D-Printed Objects. Sensors, 22(22), p.8869.

Huang, M., Pan, J., Wang, Y., Li, Y., Hu, X., Li, X., Xiang, D., Hemingray, C. and Xiao, K. 2022b. Influences of shape, size, and gloss on the perceived color difference of 3D printed objects. JOSA A, 39(5), pp.916-926.

Huertas, R., Melgosa, M. and Hita, E. 2006. Influence of random-dot textures on perception of suprathreshold color differences. JOSA A, 23(9), pp.2067-2076.

Hung, P.C. 1993. Colorimetric calibration in electronic imaging devices using a look-up table model and interpolations. J Electronic Image. 2, pp.53–61.

Hung, W., Sun, P., Lai, Y., Chen, Y. 2018. A Visual Evaluation of Color Differences between 3D Objects. In Proceedings of CIE 2018, Taipei, Chinese Taipei, 26-27 April 2018.

Igarashi T., Nishino K. and Nayar S.K. 2005. The Appearance of Human Skin. Technical Report: CUCS-024-05, Columbia University.

ISO. 1993. Textiles-Tests for colour fastness-Part A02: Grey scale for assessing change in colour. 105-A02:1993(E).

ISO. 2010. Textiles-Tests for colour fastness-Part A01: General principles of testing. 105-A01:2010(E).

ISO. 2019. Textiles-Tests for colour fastness-Part A03: Grey scale for assessing staining. 105-A03:2019(E).

ISO/CIE. 2014. Colorimetry - Part 6: CIEDE2000 color-difference formula. 11664-6:2014, CIE Central Bureau, Vienna, Austria, 2014.

ISO/CIE. 2022. Colorimetry - Part 2: CIE Standard Illuminants. 11664-2:2022(E).

ISO/IEC. 1994. Digital compression and coding of continuous-tone still images. 10918-1:1994, Joint Picture Expert Group, Geneve, Switzerland.

ISO/TR. 2003. Graphic technology - Standard object colour spectra database for colour reproduction evaluation (SOCS). 16066:2003, ISO, Switzerland.

Jiang, J., Liu, D., Gu, J. and Süsstrunk, S. 2013, January. What is the space of spectral sensitivity functions for digital color cameras?. In 2013 IEEE Workshop on Applications of Computer Vision (WACV) (pp. 168-179). IEEE.

Jiang, L., Cui, G., Melgosa, M., Xiao, K. and Sueeprasan, S. 2021. Color-difference evaluation for 3D objects. Optics Express, 29(15), pp.24237-24254.

Jiang, L., Wang, H., Gao, C., Zhang, X., Xiao, K., Melgosa, M. and Li, C. 2022. Skin color measurements before and after two weeks of sun exposure. Vision Research, 192, p.107976.

Jones M.J. and Rehg J.M. 2002. Statistical color models with application to skin detection. Int J Comput Vis. 46(1):81-96.

Jones, A.L., Porcheron, A., Sweda, J.R., Morizot, F. and Russell, R. 2016. Coloration in different areas of facial skin is a cue to health: The role of cheek redness and periorbital luminance in health perception. Body Image, 17, pp.57-66.

Kikuchi, K., Masuda, Y., Yamashita, T., Kawai, E. and Hirao, T. 2015. Image analysis of skin color heterogeneity focusing on skin chromophores and the age-related changes in facial skin. Skin Research and Technology, 21(2), pp.175-183.

Kim, D.H. and Nobbs, J.H. 1997. New weighting functions for the weighted CIELAB color difference formula, in: Proceedings of the AIC Color 97, Kyoto, 1, pp. 446–449.

Lee, M., Han, J. and Kim, E. 2019. An evaluation of the effects of makeup on perceived age based on skin color in Korean women. J Cosmet Dermatol, 18(4):1044-1051.

Li, C., Cui, G. and Luo, M.R. 2003. The accuracy of polynomial models for characterizing digital cameras. Proceedings of AIC2003 Bangkok: Color Communication and Management. pp.166–170.

Li, C., Li, Z., Wang, Z., Xu, Y., Luo, M.R., Cui, G., Melgosa, M., Brill, M.H. and Pointer, M. 2017. Comprehensive color solutions: CAM16, CAT16, and CAM16-UCS. Color Res. Appl. 42(6), pp.703–718.

Li, C., Perales, E., Luo, M.R. and Martínez-verdú, F. 2007. The Problem with CAT02 and Its Correction.

Littlewood, D. and Subbarayan, G. 2006. Updating a CMYK printer model using a sparse data set. Journal of Imaging Science and Technology, 50(6), pp.556-566.

Liu, H., Huang, M., Cui, G., Luo, M.R. and Melgosa, M. 2013. Color-difference evaluation for digital images using a categorical judgment method. JOSA A, 30(4), pp.616-626.

Liu, Y., Zhang, R., Ye, H., Wang, S., Wang, K.P., Liu, Y. and Zhou, Y. 2019. The development of a 3D colour reproduction system of digital impressions with an intraoral scanner and a 3D printer: a preliminary study. Scientific reports, 9(1), pp.20052.

Luo M. R., Cui G. and Rigg B. 2001. The Development of the CIE 2000 Colour Difference Formula. Color Res. Appl. 26(5), pp.340-350.

Luo M.R. and Hunt R.W.G. 1998. The structure of the CIE 1997 colour appearance model (CIECAM97s). Color Res. Appl., 23(3), pp.138–146.

Luo, M.R. and Rigg, B. 1987. BFD (l: c) colour-difference formula Part 1ndashDevelopment of the formula. Journal of the Society of Dyers and Colourists, 103(2), pp.86-94.

Luo, M.R. and Rigg, B. 1987. BFD (l: c) colour-difference formula Part 2-Performance of the formula. Journal of the Society of Dyers and Colourists, 103(3), pp.126-132.

Luo, M.R., Cui, G. and Li, C. 2006. Uniform colour spaces based on CIECAM02 colour appearance model. Color Research & Application. 31(4), pp.320-330.

Luo, M.R., Cui, G. and Rigg, B. 2001. The development of the CIE 2000 colour-difference formula: CIEDE2000. Color Research & Application, 26(5), pp.340–350.

Ly, B.C.K., Dyer, E.B., Feig, J.L., Chien, A.L. and Del Bino, S. 2020. Research techniques made simple: cutaneous colorimetry: a reliable technique for objective skin color measurement. Journal of Investigative Dermatology, 140(1), pp.3-12.

MacAdam, D.L. 1942. Visual sensitivities to color differences in daylight. J. Opt. Soc. Am., 32, pp.247–274.

Malacara, D. 2003. Color vision and colorimetry: theory and applications. Wiley Online Library. Color Research & Application. 28(1), pp.77-78.

Marimont, D.H. and Wandell, B.A. 1992. Linear models of surface and illuminant spectra. JOSA A, 9(11), pp.1905-1913.

Matias, A.R., Ferreira, M., Costa, P. and Neto, P. 2015. Skin colour, skin redness and melanin biometric measurements: comparison study between Antera® 3D, Mexameter® and Colorimeter®. Skin Research and Technology, 21(3), pp.346-362.

Melgosa, M., Cui, G., Oleari, C., Pardo, P.J., Huang, M., Li, C. and Luo, M.R. 2017. Revisiting the weighting function for lightness in the CIEDE 2000 colour-difference formula. Coloration Technology, 133(4), pp.273-282.

Melgosa, M., García, P.A., Gómez-Robledo, L., Shamey, R., Hinks, D., Cui, G. and Luo, M.R. 2011. Notes on the application of the standardized residual sum of squares index for the assessment of intra-and inter-observer variability in color-difference experiments. JOSA A, 28(5), pp.949-953.

Melgosa, M., Huertas, R. and Berns, R.S. 2008. Performance of recent advanced color-difference formulas using the standardized residual sum of squares index. JOSA A, 25(7), pp.1828-1834.

Melgosa, M., Richard, N., Fernández-Maloigne, C., Xiao, K., de Clermont-Gallerande, H., Jost-Boissard, S. and Okajima, K. 2018. Colour differences in Caucasian and Oriental women's faces illuminated by white light-emitting diode sources. International Journal of Cosmetic Science, 40(3), pp.244-255.

Mirjalili, F., Luo, M.R., Cui, G. and Morovic, J. 2019. Color-difference formula for evaluating color pairs with no separation: ΔE NS. JOSA A, 36(5), pp.789-799.

Moroney, N. 2002. The CIECAM02 color appearance model, in: Proceeding of the Tenth Color Imaging Conference: Color Science, Systems, and Applications, pp.23–27.

Naik, P.P. and Farrukh, S.N. 2022. Influence of ethnicities and skin color variations in different populations: a review. Skin Pharmacology and Physiology, 35(2), pp.65-76.

Nobbs, J.H. 2002. A lightness, chroma and hue splitting approach to CIEDE2000 colour differences. Advances in Colour Science and Technology, 5(2), pp.46-53.

Ogura, Y., Kuwahara, T., Akiyama, M., Tajima, S., Hattori, K., Okamoto, K., Okawa, S., Yamada, Y., Tagami, H., Takahashi, M. and Hirao, T. 2011. Dermal carbonyl modification is related to the yellowish color change of photo-aged Japanese facial skin. Journal of dermatological science. 64(1), pp.45-52.

Pantone, L.L.C. 2012. PANTONE SkinTone™Guide. Carlstadt, NJ, USA.

Paravina, R.D., Majkic, G., del Mar Perez, M. and Kiat-amnuay, S. 2009. Color difference thresholds of maxillofacial skin replications. Journal of Prosthodontics: Implant, Esthetic and Reconstructive Dentistry, 18(7), pp.618-625.

Parraman, C., Walters, P., Reid, B. and Huson, D. 2008. Specifying colour and maintaining colour accuracy for 3D printing. In Three-Dimensional Image Capture and Applications 2008 (Vol. 6805, pp. 175-182). SPIE.

Pedersen, M., Bonnier, N., Hardeberg, J.Y. and Albregtsen, F. 2010. Attributes of image quality for color prints. Journal of Electronic Imaging, 19(1), pp.011016-011016.

Perz, M. 2010. Flicker perception in the periphery. Master dissertation, Eindhoven University of Technology.

Pointer, M.R., Attridge, G.G. and Jacobson, R.E. 2001. Practical camera characterization for colour measurement. The Imaging Science Journal, 49(2), pp.63-80.

Richards, G.M., Oresajo, C.O. and Halder, R.M. 2003. Structure and function of ethnic skin and hair. Dermatol. Clin. 21(4), pp.595–600.

Rigal, J . Abella, M. Giron, F. Caisey, L. and Lefebvre, M. 2007. Development and validation of a new Skin Color Chart, Skin Research and Technology, 13, pp.101–109.

Rigal, J. Diridollou, S. Querleux, B. Yang, G. Leroy, F. and Barbosa, V. 2010. The effect of age on skin color and color heterogeneity in four ethnic groups, Skin Research and Technology, 16, pp.168-178 .

Samanta, A.K. and Das, D. 1992. Studies on Quantitative colour measurement of direct dyed Jute Fabric in relation to computerized colour matching. Journal of Institution of Engineers-Textile Engineering, 73, pp.53.

Sarkar, A., Blondé, L., Le Callet, P., Autrusseau, F., Morvan, P. and Stauder, J. 2010. A color matching experiment using two displays: design considerations and pilot test results. In Fifth European Conference on Color in Graphics, Imaging and Vision, CGIV, Jun 2010, Joensuu, Finland.

Shaw, M., Sharma, G., Bala, R. and Dalal, E.N. 2003. Color printer characterization adjustment for different substrates.Color Research & Application, 28(6), pp.454-467.

Shen, H.L., Zheng, Z.H., Jin, C.C., Du, X., Shao, S.J. and Xin, J.H. 2013. Adaptive characterization method for desktop color printers. Journal of Electronic Imaging, 22(2), pp.023012-023012.

Sohaib, A., Amano, K., Xiao, K., Yates, J.M., Whitford, C. and Wuerger, S. 2018. Colour quality of facial prostheses in additive manufacturing. The International Journal of Advanced Manufacturing Technology, 96, pp.881-894.

Speranskaya, N.I. 1959. Determination of spectral color co-ordinates for twenty-seven normal observers. Optics Spectrosc., 7, pp.424–428.

Stephen, I.D., Law Smith, M.J., Stirrat, M.R. and Perrett, D.I. 2009. Facial skin coloration affects perceived health of human faces. International journal of primatology, 30, pp.845-857.

Stiles, W.S. and Burch, J.M. 1959. N.P.L. color-matching investigation: Final report. Optica Acta, 6, pp.1–26.

Stopp, S., Wolff, T., Irlinger, F. and Lueth, T. 2008. A new method for printer calibration and contour accuracy manufacturing with 3D-print technology. Rapid Prototyping Journal. 14(3), pp.167-172.

Su, Z., Yang, J., Li, P., Zhang, H. and Jing, J. 2021. Colour space conversion model from CMYK to CIELab based on CS-WNN. Coloration Technology, 137(3), pp.272-279.

Sun, J., Peng, Z., Zhou, W., Fuh, J.Y., Hong, G.S. and Chiu, A. 2015. A review on 3D printing for customized food fabrication. Procedia Manufacturing, 1, pp.308-319.

Sun, P.L. and Sie, Y.P. 2016. Color uniformity improvement for an inkjet color 3D printing system. Electronic Imaging, 28, pp.1-6.

Süsstrunk, S. and Bill, M.H. 2006. The Nesting Instinct: Repairing Non Nested Gamuts in CIECAM02. CIC14.

Thorstenson, C.A., Pazda, A.D., Elliot, A.J. and Perrett, D.I. 2017. Facial redness increases men's perceived healthiness and attractiveness. Perception, 46(6), pp.650-664.

Thurstone, L. L. 1927. A Law of Comparative Judgment. Psychological Review, 34, pp.273–286

Torgerson, W. S. 1954. A Law of Categorical Judgment. Consumer Behaviour, Clark L. H. (ed.), New York University Press, New York, pp.92–93

Van Noort, R. 2011. The future of dental devices is digital. Dental Materials, 28, pp.3–12.

Vanderploeg, A., Lee, S.E. and Mamp, M. 2017. The application of 3D printing technology in the fashion industry. International Journal of Fashion Design, Technology and Education, 10(2), pp.170-179.

Velastegui, R. and Pedersen, M. 2021, September. CMYK-CIELAB Color Space Transformation Using Machine Learning Techniques. In London Imaging Meeting (Vol. 2021, No. 1, pp. 73-77). Society for Imaging Science and Technology.

Walters, P., Huson, D., Parraman, C. and Stanić, M. 2009. 3D printing in colour: Technical evaluation and creative applications. In Proceedings of the Impact, Bristol, UK, 16-19 September 2009.

Wang, M., Xiao, K., Luo, M.R., Pointer, M., Cheung, V. and Wuerger, S. 2018. An investigation into the variability of skin colour measurements. Color Research & Application, 43(4), pp.458-470.

Wang, Y., Luo, M.R., Wang, M., Xiao, K. and Pointer, M. 2017. Spectrophotometric measurement of human skin colour. Color Research & Application, 42(6), pp.764-774.

Wei, X., Zou, N., Zeng, L. and Pei, Z. 2022. PolyJet 3D printing: predicting color by multilayer perceptron neural network. Annals of 3D Printed Medicine, 5, pp.100049.

Witt, K. 1995. CIE guidelines for coordinated future work on industrial colour-difference evaluation. Color Research & Application, 20(6), pp.399-403.

Witt, K. 1999. Geometric relations between scales of small color differences. Color Res. Appl., 24, pp.78–92.

Witt, K. and Döring, G. 1983. Parametric variations in a threshold colordifference ellipsoid for green painted samples. Colour Research & Application. 8, pp.153–163.

Wright, W.D. 1930. A re-determination of the mixture curves of the spectrum. Transactions of the Optical Society, 31(4), pp.201-218.

Wright, W.D. 1941. The sensitivity of the eye to small colour differences. Proceedings of the Physical Society, 53(2), pp.93-112.

Wright, W.D. 1929. A re-determination of the trichromatic coefficients of the spectral colours. Transactions of the Optical Society, 30(4), pp.141-164.

Xiao, B. and Brainard, D.H. 2008. Surface gloss and color perception of 3D objects. Visual neuroscience, 25(3), pp.371-385.

Xiao, K. 2006. Colour appearance assessment for dissimilar sizes. Doctoral thesis, University of Derby.

Xiao, K., Liao, N., Zardawi, F., Liu, H., Van Noort, R., Yang, Z., Huang, M. and Yates, J.M. 2012. Investigation of Chinese skin colour and appearance for skin colour reproduction. Chinese Optics Letters, 10(8), pp.083301.

Xiao, K., Sohiab, A., Sun, P.L., Yates, J.M., Li, C. and Wuerger, S. 2016a. A colour image reproduction framework for 3D colour printing. Advanced Laser Manufacturing Technology. 10153, pp.1015318.

Xiao, K., Yates, J.M., Zardawi, F., Sueeprasan, S., Liao, N., Gill, L., Li, C. and Wuerger, S. 2017. Characterising the variations in ethnic skin colours: a new calibrated data base for human skin. Skin Research and Technology. 23(1), pp.21-29.

Xiao, K., Zardawi, F., van Noort, R. and Yates, J.M. 2014. Developing a 3D colour image reproduction system for additive manufacturing of facial prostheses. The international journal of advanced manufacturing technology, 70, pp.2043-2049.

Xiao, K., Zardawi, F., van Noort, R. and Yates, J.M. 2013. Color reproduction for advanced manufacture of soft tissue prostheses. Journal of Dentistry, 41, pp.e15-e23.

Xiao, K., Zhu, Y., Li, C., Connah, D., Yates, J.M. and Wuerger, S. 2016b. Improved method for skin reflectance reconstruction from camera images. Optics express. 24(13), pp.14934-14950.

Yao, D., Yuan, J., Tian, J., Wang, L. and Chen, G., 2022. Pigment penetration characterization of colored boundaries in powder-based color 3D printing. Materials, 15(9), pp.3245.

Yoshikawa, H., Kikuchi, K., Takata, S. and Yaguchi, H. 2009. Development of a visual and quantitaive evaluation method for facial skin color. In Proceedings of 11th Congress of the AIC, September, 2019, Sydney.

Zardawi, F.M. 2013. Characterisation of implant supported soft tissue prostheses produced with 3D colour printing technology. Doctoral dissertation, University of Sheffield.

Zeng, H. and Luo, R. 2013. Colour and tolerance of preferred skin colours on digital photographic images. Color Research & Application, 38(1), pp.30-45.

Zhang, X., Wang, Q., Li, J., Zhou, X., Yang, Y. and Xu, H. 2017. Estimating spectral reflectance from camera responses based on CIE XYZ tristimulus values under multi-illuminants. Color Research & Application, 42(1), pp.68-77.

Bibliography

Berns, R.S. 2019. Billmeyer and Saltzman's principles of color technology. John Wiley & Sons.

CIE. 2018. Colorimetry. 4th Edition. CIE Central Bureau, Vienna, Austria.

Fairchild, M.D. 2005. Color Appearance Models, 2nd ed., J. Wiley, Chichester.

Green, P. and MacDonald, L. eds. 2011. Colour engineering: achieving device independent colour. John Wiley & Sons.

Hunt, R.W.G. and Pointer, M.R. 2011. Measuring Colour, 4th ed., John Wiley & Sons.

Hunt, R.W.G. 2004. The reproduction of colour, 6th Edition. John Wiley & Sons.

Ohta, N. and Robertson, A.R. 2006. Colorimetry: Fundamentals and Applications. John Wiley & Sons.

Schanda, J. ed., 2007. Colorimetry: understanding the CIE system. John Wiley & Sons.

List of Abbreviations

2D	Two-Dimensional
3D	Three-Dimensional
ASTM	American Society For Testing And Materials
CAD	Computer-Aided Design
CAM	Colour Appearance Model
CAT	Chromatic Adaptation Transform
CBL	Left Cheekbone
CBR	Right Cheekbone
CCD	Charged Coupled Device
CCSG	Colorchecker Sg Chart
CCT	Corelated Colour Temperature
CH	Chin
CIE	Commission Internationale De L’éclairage
CM	Centimetre
CMFs	Colour Matching Functions
CMOS	Complementary Metal–Oxide–Semiconductor
CMYK	Cyan, Magenta, Yellow, Key
DNN	Deep Neural Network
DSLR	Digital Single-Lens Reflex
FC	Fully Connected Layers
FH	Forehead
FSCD	Facial Skin Colour Data
ICC	International Color Consortium
ISO	International Organization For Standardization
JND	Just-Noticeable Difference
JPD	Just-Perceptible Difference
JPEG	Joint Photographic Experts Group

K	Kelvin
LED	Light-Emitting Diode
LLSC	Leeds-Liverpool Skin Colour
MAV	Medium Area View
MCDM	Mean Colour Difference From The Mean
MM	Millimetre
MTL	Material Template Library
NM	Nanometre
NT	Nose Tip
OBJ	Object
PCA	Principal Component Analysis
PCC	Pearson Correlation Coefficient
PR	Polynomial Regression
RGB	Red, Green, Blue
RMSE	Root-Mean-Square Error
RPR	Root Polynomial Regression
SAV	Small Area View
SCE	Specular Component Excluded
SCI	Specular Component Included
SDC	Society Of Dyers And Colourists
SLR	Single-Lens Reflex
SOCS	Standard Object Colour Spectra
SPD	Spectral Power Distribution
SSCC	Silicon Skin Colour Chart
STRESS	Standardized Residual Sum Of Squares
TIFF	Tagged Image File Format

Appendix

This appendix shows the inspection report and calibration certification for Konica Minolta CM700d spectrophotometer.

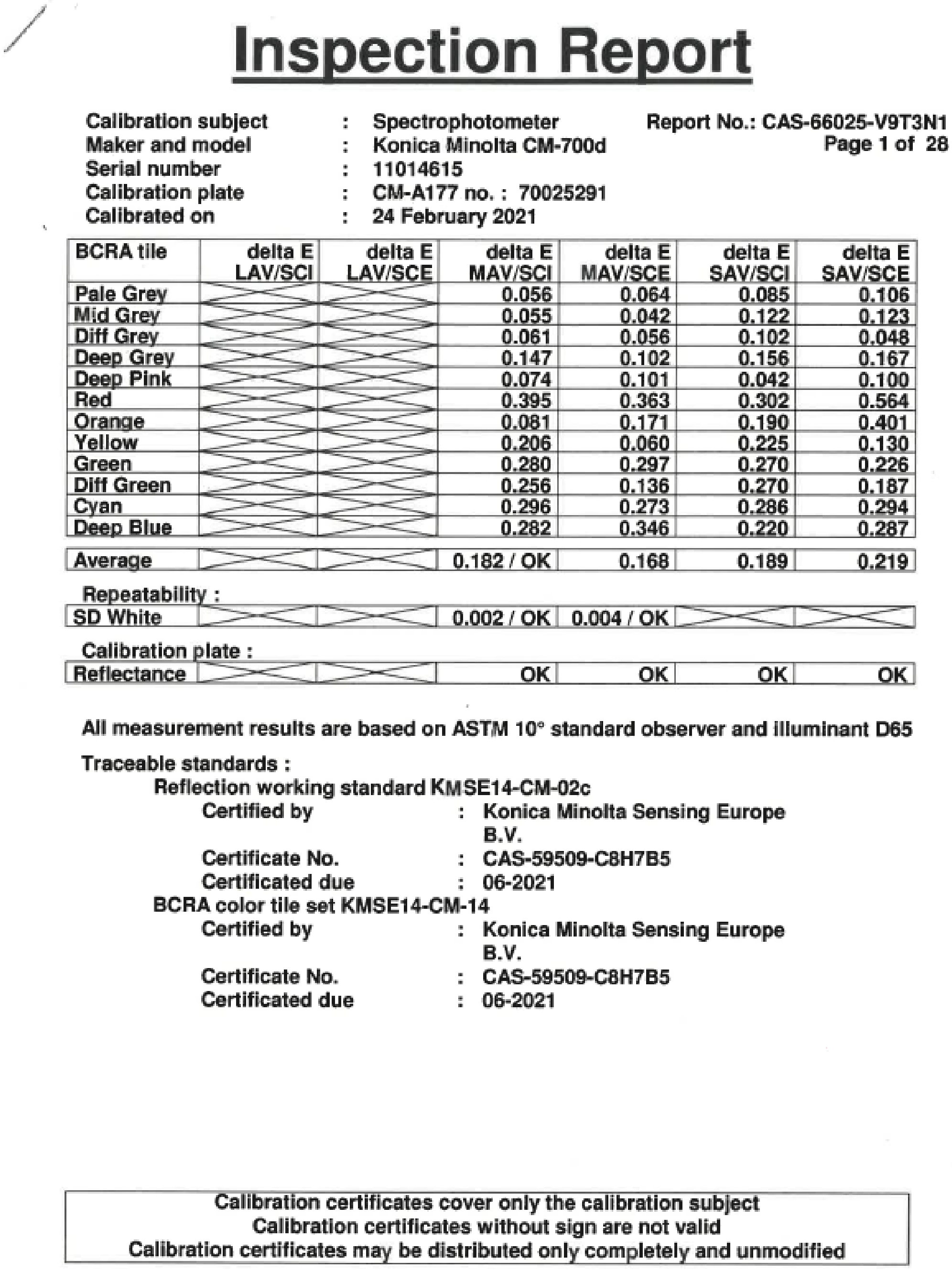

Inspection Report

Calibration subject	:	Spectrophotometer	Report No.: CAS-66025-V9T3N1
Maker and model	:	Konica Minolta CM-700d	Page 1 of 28
Serial number	:	11014615	
Calibration plate	:	CM-A177 no. : 70025291	
Calibrated on	:	24 February 2021	

BCRA tile	delta E LAV/SCI	delta E LAV/SCE	delta E MAV/SCI	delta E MAV/SCE	delta E SAV/SCI	delta E SAV/SCE
Pale Grey			0.056	0.064	0.085	0.106
Mid Grey			0.055	0.042	0.122	0.123
Diff Grey			0.061	0.056	0.102	0.048
Deep Grey			0.147	0.102	0.156	0.167
Deep Pink			0.074	0.101	0.042	0.100
Red			0.395	0.363	0.302	0.564
Orange			0.081	0.171	0.190	0.401
Yellow			0.206	0.060	0.225	0.130
Green			0.280	0.297	0.270	0.226
Diff Green			0.256	0.136	0.270	0.187
Cyan			0.296	0.273	0.286	0.294
Deep Blue			0.282	0.346	0.220	0.287
Average			0.182 / OK	0.168	0.189	0.219

Repeatability :

SD White			0.002 / OK	0.004 / OK		

Calibration plate :

Reflectance			OK	OK	OK	OK

All measurement results are based on ASTM 10° standard observer and illuminant D65

Traceable standards :

Reflection working standard KMSE14-CM-02c

Certified by	:	Konica Minolta Sensing Europe B.V.
Certificate No.	:	CAS-59509-C8H7B5
Certificated due	:	06-2021

BCRA color tile set KMSE14-CM-14

Certified by	:	Konica Minolta Sensing Europe B.V.
Certificate No.	:	CAS-59509-C8H7B5
Certificated due	:	06-2021

Calibration certificates cover only the calibration subject
Calibration certificates without sign are not valid
Calibration certificates may be distributed only completely and unmodified

KONICA MINOLTA

Calibration certificate

Page 1 / 2

Certificate number : CAS-66025-V9T3N1

Maker : Konica Minolta
Model : Spectrophotometer CM-700d
Serial number : 11014615
Calibration Plate : 70025291

Commissioner :
University of Leeds
School of Design
Woodhouse Lane
Leeds
LS2 9JT
United Kingdom

Calibrated on : 24/02/2021
Recommended next calibration : 24/02/2022

This is to certify that above calibration subject is inspected and calibrated, using apparatus traceable to Japanese or other international standards. The results of inspection and calibration have been found to satisfy the inspection standards of Konica Minolta Sensing. For detailed information about traceability please refer to:
https://www.konicaminolta.eu/en/measuring-instruments/technical-service/maintenance-calibration/traceability.html

Warrington, 24/02/2021

Service Manager

Ulrich Strahlendorf

Service Technician

B. Burrow

Brian Burrow

Giving Shape to Ideas

Konica Minolta Sensing Europe B.V.
UK Branch Office
Unit 9 Webster Court, Westbrook Crescent, Gemini Business Park, WA5 8WD Tel: +44 (0) 1925 467 300 Fax: +44 (0) 1925 711 143
www.konicaminolta.eu Email: info.uk@seu.konicaminolta.eu

Bank Account ING Bank **IBAN** GB70INGB23885920342529 **Swift/BIC** INGBGB22
Register FC26708 **VAT** GB883345500

KONICA MINOLTA

Page 2/2 of calibration certificate with number: CAS-66025-V9T3N1

Inspection protocol

Maker	:	Konica Minolta
Model	:	Spectrophotometer CM-700d
Serial number	:	11014615
Calibration Plate	:	70025291
Calibrated on	:	24/02/2021

Check point	Result	Remark
Condition of instrument	✓	
Switches	✓	
Program	✓	
Display	✓	
Accuracy	✓	
Interface	✓	
Accessory	✓	

Environment conditions: Temperature: 23° C +/- 1° C
Humidity: < 85%

Calibration certificates cover only the calibration subject.
Calibration certificates without sign are not valid.
Calibration certificates may be distributed only completely and unmodified.